La borsa di dottorato è stata cofinanziata con risorse del
Programma Operativo Nazionale Ricerca e Innovazione 2014-2020 (CCI 2014IT16M2OP005)
Fondo Sociale Europeo, Azione I.1 "Dottorati Innovativi con caratterizzazione Industriale"

UNIVERSITA' DELLA CALABRIA

Dipartimento di Fisica

Dottorato di Ricerca in

Scienze e Ingegneria dell'Ambiente, delle Costruzioni e dell'Energia

Con il contributo di (Ente finanziatore)

MIUR – PON R&I 2014 - 2020

CICLO XXXIII

DEVELOPMENT OF ADVANCED SYSTEMS FOR ENERGY CONVERSION BASED ON INNOVATIVE TWO-DIMENSIONAL MATERIALS

Settore Scientifico Disciplinare: Fis 01

Coordinatore: Ch.mo Prof. Salvatore Critelli

Firma _____

Critelli
Salvatore
27.09.2021
05:53:51
GMT+00:00

Tutor: Ch.mo Prof. Gennaro Chiarello

Firma Gennaro Chiarello

Co-Tutor: Dr.ssa Anna Cupolillo

Firma Anna Cupolillo

Dottorando: Dott.ssa Marilena Isabella Zappia

Firma Marilena Isabella Zappia

UNIONE EUROPEA
Fondo Sociale Europeo

Ministero dell'Istruzione, dell'Università e della Ricerca

PON
RICERCA E INNOVAZIONE
2014 - 2020

UNIVERSITÀ DELLA CALABRIA

UNIONE EUROPEA
Fondo Sociale Europeo
Ministero dell'Istruzione, dell'Università e della Ricerca
PON RICERCA E INNOVAZIONE 2014 - 2020
UNIVERSITÀ DELLA CALABRIA

Preface

Before going into the thesis entitled: "Development of Advanced Systems for Energy Conversion based on innovative Two-Dimensional", this preface gives a clear idea of the main topics that will be discussed in the following sections. The first fourth chapters will deal with the liquid-phase exfoliation of layered metal monochalcogenides in their few-layer flake form, and the application of these novel two-dimensional materials within electrochemical devices. The last chapter reports an extensive surface characterization, as well as the electronic characterization, of $PtTe_2$, a material of the family of the transition metal dichalcogenides whose properties are still almost unexplored for practical applications.

This project has been carried out in three different institutions. The first part of the PhD has taken place at the University of Calabria, under the supervision of Prof. Gennaro Chiarello and Dr. Anna Cupolillo, in which I spent 12 months. The second part of the PhD was carried out at BeDimensional S.p.A., under the supervision of Dr. Francesco Bonaccorso, in which I spent 18 months. The third part of the PhD was carried out at the Unìversita Autonòma de Madrid, under the supervision of Prof. Daniel Farias, in which I spent 6 months.

During these three years of PhD, I have grown both professionally and, above all, personally, thanks to the people who have been close to me. For this reason, I would like to thank my supervisors for their excellent guidance and support throughout this journey. I would also like to thank all my colleagues, friends, and family for having been with me throughout this time.

I hope you enjoy this reading.

Marilena Isabella Zappia

UNIONE EUROPEA
Fondo Sociale Europeo

Ministero dell'Istruzione, dell'Università e della Ricerca

PON
RICERCA E INNOVAZIONE
2014 - 2020

UNIVERSITÀ DELLA CALABRIA

UNIONE EUROPEA
Fondo Sociale Europeo
Ministero dell'Istruzione, dell'Università e della Ricerca
PON RICERCA E INNOVAZIONE 2014 - 2020
UNIVERSITÀ DELLA CALABRIA

ABSTRACT

The even growing energy demand due to the demographic growth and the consequent economic expansion has led to the search for innovative technologies available for energy production and conversion from green and renewable sources such as solar energy. In this context, two-dimensional (2D) materials, including either single- and few-layer flake forms, are constantly attracting more and more interest as potential advanced photo(electro)catalysts for redox reactions leading to green fuel production. Recently, layered semiconductors of group-III and group-IV, which can be exfoliated in their 2D form due to low cleavage energy (typically < 0.5 J m^{-2}), have been theoretically predicted as water splitting photocatalysts for hydrogen production. For example, their large surface-to-volume ratio intrinsically guarantees that the charge carriers are directly photogenerated at the interface with the electrolyte, where redox reactions take place before they recombine. Moreover, their electronic structure can be tuned by controlling the number of layers, fulfilling the fundamental requirements for water splitting photocatalysts, *i.e.*: 1) conduction band minimum (CBM) energy (E_{CBM}) > reduction potential of H^+/H_2 ($E(H^+/H_2)$); 2) valence band maximum (VBM) energy (E_{VBM}) < reduction potential of O_2/H_2O ($E(O_2/H_2O)$). A requirement for large-scale applications is the development of low-cost, reliable industrial production processes. In this scenario, liquid-phase exfoliation (LPE) methods provide scalable production of 2D materials in form of liquid dispersions, enabling their processing in thin-film through low-cost and industrially relevant deposition techniques. This thesis investigates, for the first time, the photoelectrochemical (PEC) activity of single-/few-layer flakes of GaS, GaSe, and GeSe produced through ultrasound-assisted LPE in environmentally friendly solvents (*e.g.*, 2-propanol) in aqueous media. Our results are

consequently used to design proof-of-concept PEC water splitting photoelectrodes, as well as PEC-type photodetectors. Moreover, structural and electronic properties of $PtTe_2$ have been investigated, being this material a potential catalyst for the hydrogen evolution reaction (HER) and other fuel-producing electrochemical reactions.

SINTESI

La crescente domanda energetica dovuta all'incremento demografico e alla conseguente espansione economica ha portato alla ricerca di tecnologie innovative per la produzione e la conversione dell'energia da fonti pulite e rinnovabili come l'energia solare. In questo contesto, i materiali bidimensionali (2D), comprese le forme allotropiche a uno o pochi strati, attirano costantemente un interesse sempre maggiore come foto(elettro)catalizzatori avanzati utilizzati nelle reazioni redox che portano alla produzione di carburante ecosostenibile. Recentemente è stato previsto teoricamente che i semiconduttori del gruppo III e del gruppo IV stratificati, che possono essere esfoliati nella loro forma 2D grazie alla loro bassa energia di scissione (tipicamente < 0,5 J m-2), sono adatti per la scissione elettrochimica dell'acqua per la produzione di idrogeno. Ad esempio, il loro ampio rapporto superficie-volume garantisce che i portatori di carica siano intrinsecamente fotogenerati direttamente all'interfaccia con l'elettrolita, dove avvengono le reazioni redox prima che si ricombinano. Inoltre, la loro struttura elettronica può essere regolata controllando il numero di strati, soddisfacendo i requisiti fondamentali per i fotocatalizzatori per la scissione dell'acqua, ovvero: 1) l'energia minima della banda di conduzione (CBM) (E_{CBM}) > del potenziale di riduzione di H^+/H_2 ($E(H^+/ H_2)$); 2) l'energia massima della banda di valenza (VBM) (E_{VBM}) < del potenziale di riduzione di O_2/H_2O ($E(O_2/H_2O)$). Un requisito per le applicazioni su larga scala è lo sviluppo di processi di produzione industriale a basso costo e affidabili. In questo scenario, i metodi di esfoliazione in fase liquida (LPE) possono fornire una produzione scalabile di materiali 2D sottoforma di dispersione liquida, consentendo il processo di lavorazione nella forma di film sottili attraverso

tecniche di deposizione a basso costo e di rilievo industriale. Questa tesi indaga, per la prima volta, l'attività fotoelettrochimica (PEC) di cristalli monostrato di GaS, GaSe e GeSe prodotte con l'approccio della LPE in solventi non tossici (2-propanolo) per la scissione dell'acqua attraverso la PEC e fotorivelatori di tipo PEC. Sono state inoltre studiate le proprietà strutturali ed elettroniche del $PtTe_2$, le cui potenzialità applicative sono ancora inesplorate. Questa tesi indaga, per la prima volta, l'attività fotoelettrochimica (PEC) di cristalli a singolo o pochi strati di GaS, GaSe e GeSe prodotte mediante LPE tramite ultrasuoni in solventi ecocompatibili (es. 2-propanolo) o acquosi. I nostri risultati sono stati quindi utilizzati per progettare prototipi di elettrodi fotoelettrochimici per la scissione dell'acqua, nonché fotorivelatori di tipo PEC. Inoltre, sono state studiate le proprietà strutturali ed elettroniche di $PtTe_2$, essendo un potenziale catalizzatore per la reazione di evoluzione dell'idrogeno (HER) e altre reazioni elettrochimiche per la produzione di combustibile.

List of publications and contributions

Original publications on ISI Journals:

1. Ghosh, B., Alessandro, F., Zappia, M., Brescia, R., Kuo, C. N., Lue, C. S., Chiarello, G., Politano, A., Caputi, L. S., Amit, A., Cupolillo, A.
Broadband excitation spectrum of bulk crystals and thin layers of $PtTe_2$
Physical Review B 99.4 2019, 045414.

2. Anemone, G., Garnica, M., Zappia, M., Aguilar, P. C., Al Taleb, A., Kuo, C. N., Lue, C. S., Politano, A., Benedek, G., Vázquez de Parga, A. L, Miranda, R., Farías, D.
Experimental determination of surface thermal expansion and electron–phonon coupling constant of 1T-$PtTe_2$
2D Materials 7.2 2020, 025007.

3. Zappia, M. I., Bianca G., Bellani, S., Serri, M., Najafi, L., Oropesa-Nuñez, R., Martín-García, B., Bouša, D., Sedmidubský, D., Pellegrini, V., Sofer Z., Bonaccorso, F.
Solution-Processed GaSe Nanoflake-Based Films for Photoelectrochemical Water Splitting and Photoelectrochemical-Type Photodetectors
Advanced Functional Materials 2020, 30, 1909572.

4. Bianca, G., Zappia, M. I., Bellani, S., Sofer, Z., Serri, M., Najafi, L., Oropesa-Nuñez, R., Martín-García, B., Hartman, T., Leoncino, L., Sedmidubský, D., Pellegrini, V., Chiarello, G., Bonaccorso, F.
Liquid-Phase Exfoliated GeSe Nanoflakes for Photoelectrochemical-Type Photodetectors and Photoelectrochemical Water Splitting
ACS Applied Materials & Interfaces 2020, 12, 48598-48613.

5. Curreli, N., Serri, M., Zappia, M. I., Spirito, D., Bianca, G., Buha, J., Najafi, L., Sofer, Z., Krahne, R., Pellegrini, V., Bonaccorso, F.
Liquid-Phase Exfoliated Gallium Selenide for Light-Driven Thin-Film Transistors
Advanced electronic Materials 2021, 7, 2001080.

6. Zappia, M. I., Bianca, G., Bellani, S., Curreli, N., Sofer, Z., Serri, M., Najafi,L., Piccinni, M., Oropesa-Nuñez, R., Marvan, P., Pellegrini, V., Kriegel, I., Prato, M., Cupolillo, A., Bonaccorso, F.
Two-dimensional (2D) gallium sulfide (GaS) nanoflakes for UV-selective photoelectrochemical-type photodetectors

The Journal Physical of Chemistry C 2021, 125, 22, 11857–11866.

7. Mariani P., Najafi L., Bianca G., Zappia M. I., Gabatel L., Agresti A., Pescetelli S., Bellani S., Bonaccorso F., Di Carlo A.
Low-Temperature Graphene-Based Paste for Large-Area Carbon Perovskite Solar Cells
ACS Applied Materials & Interfaces 2021 13 (19), 22368-22380.

8. Bellani S., Najafi L., Prato M., Oropesa-Nuñez R., Martín-García B., Gagliani L., Mantero E., Marasco L., Bianca G., Zappia M. I., Demirci C., Olivotto S., Mariucci G., Pellegrini V., Schiavetti M., Bonaccorso F.
Graphene-Based Electrodes in a Vanadium Redox Flow Battery Produced by Rapid Low-Pressure Combined Gas Plasma Treatments
Chemistry of Materials 2021, 33, 11, 4106–4121.

Communications at Conferences

Oral communications:

1. **Graphene Canada2020** (November 16 – 17)
   Zappia M. I., Bianca, G., Bellani, S., Curreli, N., Sofer, Z., Serri, M., Najafi, L., Oropesa-Nuñez, R., Martín-García, B., Bouša, D., Sedmidubský, D., Pellegrini, V., Cupolillo, A., Bonaccorso F.
   Group-III layered semiconductors (GaSe and GaS) for photoelectrochemical (PEC)-type photodetectors

2. **Graphene 2020** (October 19 – 22)**:**
   Grenoble, France
   Zappia M. I., Bianca, G., Bellani, S., Serri, M., Najafi, L., Oropesa-Nuñez, R., Martín-García, B., Bouša, D., Sedmidubský, D., Pellegrini, V., Sofer, Z., Cupolillo, A., Bonaccorso F.
   Solution-processed GaSe nanoflake-based films for photoelectrochemical water splitting and photoelectrochemical-type photodetectors

3. **Material Research Society MRS Fall Meeting & Exhibit 2020** (November 27-December 4)
   Boston, United States
   Bianca G., Zappia M. I., Bellani S., Sofer Z., Serri M., Najafi L., Oropesa-Nuñez R., Martín-García B., Hartman T., Sedmidubský D., Pellegrini V., Chiarello G., Bonaccorso F.
   Solution-processed photoelectrochemical (PEC)-type photodetectors based on layered metal monochalcogenides (GaS, GaSe, GeSe)

4. **Graphene Canada2020** (November 16 – 17)
   Bianca G., Zappia M. I., Bellani S., Sofer Z., Serri M., Najafi L., Oropesa-Nuñez R., Martín-García B., Hartman T., Sedmidubský D., Pellegrini V., Chiarello G., Bonaccorso F.
   2D Layered metal monochalcogenides for photoelectrochemical (PEC)-type photodetectors and water splitting applications

5. **Graphene 2019** (June 25 – 28)**:**
   Rome, Italy

Alessandro, F., Ghosh, B., Zappia, M., Brescia, R., Kuo, C. N., Lue, C. S., Chiarello, G., Politano, A., Caputi, L. S., Amit, A., Cupolillo, A.
High-energy excitations in the type-II Dirac semimetal $PtTe_2$

Poster Communications:

1. **Graphene 2020 (19-23 October 2020)**
   Grenoble, France
   Bianca G., Zappia M. I., Bellani S., Sofer Z., Serri M., Najafi L., Oropesa-Nuñez R., Martín-García B., Hartman T., Sedmidubský D., Pellegrini V., Cupolillo A., Bonaccorso F.
   Liquid-phase exfoliated GeSe nanoflakes for photoelectrochemical-type photodetectors and photoelectrochemical water splitting

2. **Graphene and 2DM Industrial Forum 2020 (May 27)**
   Zappia M. I., Bianca G., Bellani S., Serri M., Najafi L., Oropesa-Nuñez R., Martín-García B., Bouša D., Sedmidubský D., Pellegrini V., Sofer Z., Cupolillo A., Bonaccorso F.
   Solution-processed GaSe nanoflake-based films for photoelectrochemical water splitting

3. **Graphene and 2DM Industrial Forum 2020 (May 27)**
   Bianca G., Zappia M. I., Bellani S., Serri M., Najafi L., Martín-García B., Oropesa-Nuñez R., Tomáš Hartman, Sedmidubský D., Pellegrini V., Sofer Z., Chiarello G., Bonaccorso F.
   Liquid-phase exfoliated GeSe nanoflakes for photoelectrochemical-type photodetectors

4. **Graphene and 2DM Industrial Forum 2020 (May 27)**
   Piccinni M., Bellani S., Bianca G., Zappia M. I., Najafi L., Bonaccorso F.
   Solution-processed Layered Double Hydroxides for Energy Applications

5. **Graphene and 2DM Industrial Forum 2020 (May 27)**
   Mariani P., Najafi L., Bellani S., Zappia M. I., Bianca G., Yaghoobi Nia N., Pescetelli S., Agresti A., Bonaccorso F., Di Carlo A**.**
   Graphene-based counter-electrode for large area gold-free perovskite solar devices

Contents

List of Abbreviations 1

INTRODUCTION 5

Chapter 1: *2D Materials Family: structure and proprieties* 9

1.1 Graphene 9

1.1.1 Graphene properties 10

1.2 Transition Metal Dichalcogenides (TMDs) 11

1.2.1 Platinum Ditelluride ($PtTe_2$) 14

1.3 Metal Monochalcogenides (MMCs) 14

1.3.1 Group-III Monochalcogenides: Gallium Selenide (GaSe) and Gallium Sulfide (GaS) 15

1.3.2 Group-IV Monochalcogenide: Germanium Selenide (GeSe) 16

Chapter 2: *Production Methods* 17

2.1 Micromechanical exfoliation 18

2.2 Liquid phase exfoliation 18

2.2.1 Dispersion 19

2.2.2 Exfoliation 20

2.2.3 Purification 24

2.3 Chemical vapour deposition 24

2.4 Molecular beam epitaxy 25

Chapter 3: *Characterization of 2D Metal Monochalcogenides (MMCs)* 27

3.1 Morphological characterization 28

3.2 Optical and structural characterization 30

Chapter 4: *Metal Monochalcogenides for PEC Water Splitting* 37

4.1 Fundamentals of Photoelectrochemical (PEC) Water Splitting 37

4.2 Photoelectrochemical cell 43

4.2.1 Efficiency and figures of merit (FoM) 44

4.3 Photoelectrodes fabrication 47

4.4 Photoelectrochemical measurements of MMCs and results 48

4.4.1 Gallium Selenide 50
4.4.2 Germanium Selenide 52
Chapter 5: *MMCs for PEC-type Photodetectors* 55
5.1 Self-Powered Photodetectors 55
5.2 Results 56
5.2.1 Gallium Selenide 57
5.2.2 Gallium Sulfide 59
5.2.3 Germanium Selenide 62
Chapter 6: *$PtTe_2$: an insight into structural and electronic properties* 67
6.1 Structural corrugation and surface thermal expansion of $PtTe_2$ 68
6.2 Electron-phonon coupling constant of $PtTe_2$ 72
6.3 The broadband excitation spectrum of $PtTe_2$ 74
CONCLUSIONS 81
Appendix A: *Characterization techniques of 2D material* 85
A.1 Electron energy loss spectroscopy (EELS) 85
A.2 Helium atom scattering (HAS) 86
A.3 Optical absorption spectroscopy 87
A.4 Raman spectroscopy 88
A.5 Atomic force microscopy (AFM) 89
A.6 Electronic microscopy 91
A.6.1 Transmission electron microscopy (TEM) 91
A.6.2 Scanning electron microscopy (SEM) 92
REFERENCES 94

List of Abbreviations

0D	Zero-dimensional
1D	One-dimensional
2D	Two-dimensional
3D	Three-dimensional
Ag/AgCl	Silver/SilverChloride
AM 1.5	Air mass 1.5 (1000 W m^{-2})
Au	Gold
C	Concentration
CB	Conduction band
CBE	Chemical beam epitaxy
CBM	Conduction band maximum
CE	Counter electrode
CNT	Carbon nanotube
CVD	Chemical vapor deposition
DMF	N,N-dimethylformamide
DRS	Diffusive reflectance spectroscopy
E_a	Activation energy
EDX	Energy-dispersive X-ray spectroscopy
EELS	Electron energy-loss spectroscopy
E_g	Bang gap energy
E_{sur}	Surface energy
Ext(λ)	Extinction

FoM	Figures of merit
H_2	Hydrogen
H_2O	Water
H_2SO_4	Sulfuric acid
H_3O^+	Hydronium ion
H_{ads}	Hydrogen adsorbed
HAS	Helium atom scattering
HER	Hydrogen evolution reaction
IPA	2-Propanol
$J_{+1.23\ V\ vs\ RHE}$	Photocurrent density at +1.23 V *vs.* RHE
$J_{0V\ vs\ RHE}$	Photocurrent density at 0 V *vs.* RHE
J_{SC}	Short circuit photocurrent
LED	Light-emitting diode
LVS	Linear sweep voltammetry
MBE	Molecular beam epitaxy
MC	Micromechanical cleavage
MMC	Metal monochalcogenide
MWCNT	Multi-walled carbon nanotube
NMP	N-methyl-2-pyrrolidone
O_2	Oxygen
OER	Oxygen evolution reaction
OH^-	Hydroxyl group
PEC	Photoelectrochemical
PL	Photoluminescence
Pt	Platinum

RE	Reference electrode
RHE	Reversible hydrogen electrode
RT	Room temperature
s	sedimentation coefficient
SBS	Sedimentation-based separation
SEM	Scanning electron microscopy
Si	Silicon
SWCNT	Single-walled carbon nanotube
T	Temperature
TEM	Transmission electron microscopy
TMD	Transition metal dichalcogenides
T_s	Surface temperature
UHV	Ultra-high vacuum
UV	Ultraviolet
VB	Valence band
VBM	Valence band maximum
V_{oc}	Open circuit voltage
WC	Working electrode
WJM	Wet-jet milling
XRD	X-Ray diffraction spectroscopy
α	Absorption coefficient
γ	Surface energy
δ_D	Energy from dispersion forces between molecules
ΔG^0	Gibbs free energy
ΔG_{H^+}	Hydrogen adsorption free energy

δ_H	Energy from hydrogen bonds between molecules or electron exchange parameter
δ_P	Energy from dipolar intermolecular force between molecules
η	Viscosity
η_{STH}	Solar-to-hydrogen conversion efficiency
λ	Wavelength
$\lambda_{e\text{-}ph}$	Electron-phonon coupling constant
π	Bonding molecular orbital
π^*	Antibonding molecular orbital
ϕ_{saved}	Ratiometric power-saved efficiency

Introduction

Nowadays, demographic growth and significant economic expansion have led to an annual energy consumption of ~17.91 TWy, and this consumption is expected to double up to ~27 TWy by 2050.

Most of the energy is currently produced from non-renewable energy sources, such as fossil fuels or uranium. This has caused a significant increase in carbon dioxide (CO_2) in the air and other greenhouse gases (GHGs) such as CH_4 or N_2O, with a disastrous impact on the climate, global pollution, and human health. These factors, combined with the rising prices of traditional energy sources, have led to an increasingly urgent demand for green and renewable resources, namely solar, wind, geothermal, and hydroelectric power.

Among these energy sources, solar energy represents the most abundant, clean, and renewable energy resource on the planet, supplying the earth with approximately 173000 TW power.

However, to date, the challenge lies in developing cost-effective, stable, and efficient large-scale solar energy conversion systems.

In this context, the production of molecular hydrogen (H_2) from photoelectrochemical (PEC) water splitting, has been proposed for the storage and distribution of solar energy in the so-called "Hydrogen economy", representing one of the most pursued solutions for clean energy. In fact, H_2 can be extracted from water using a photoelectrochemical (PEC) system, in which the electromagnetic radiation is converted into chemical fuels and electricity. Molecular H_2 possesses high energy density (120-140 MJ kg^{-1} for H_2 *versus* 44 MJ kg^{-1} for gasoline) being a promising energy carrier for replacing traditional fossil fuels. Nevertheless, PEC systems are still facing crucial challenges, which are mainly related to their insufficient solar-to-hydrogen power conversion efficiency (η_{STH}) and long-term instability. Indeed, the theoretical efficiencies for solar-

driven water splitting cells of various configurations reported in literature (for example, a η_{STH} ~ 31% in the case of PEC water splitting with two light absorbers or ~ 28.7% for photovoltaic-electrochemical system with bipolar alkaline electrolyzer) cannot be reached experimentally yet. Therefore, the research of earth-abundant materials with PEC properties is an unstoppable field of research, aiming to solve the present open issues and to propose advanced H_2 production systems.

In this scenario, layered materials emerged as photocatalysts candidates. More in detail, these materials show strong in-plane and weak out-of-plane chemical bonds and can be therefore exfoliated to increase their electrochemically accessible surface area, in which the water splitting reaction takes place.

The morphology of the layered nanomaterials strongly affects their final optoelectronic properties, which can therefore be tuned by controlling the number of layers as well as the lateral size due to quantum confinement effects. In particular, their two-dimensional (2D) forms, including monolayers have sparked great interest due to their astonishing properties, which are often different from those of their bulk counterparts.

Among 2D materials, metal monochalcogenides (MMCs) have been studied due to their potential applications as photocatalysts for water splitting reactions. In fact, their optoelectronic structure fulfils the fundamental requirements for water splitting photocatalysts:

1. conduction band minimum energy (E_{CBM}) greater than the reduction potential of H^+/H_2 ($E_{CBM} > E(H^+/H_2)$);
2. valence band maximum energy (E_{VBM}) less than the reduction potential of O_2/H_2O ($E_{VBM} < E(O_2/H_2O)$).

Moreover, the high electrical mobility of their photogenerated charges and their large surface-to-volume ratio synergistically guarantee that the charges reach the interface with the electrolyte, where redox reactions take place, cancelling out recombination losses.

To address large-scale PEC applications, it is also pivotal to develop low-cost, reliable industrial production processes for material production. In this context, liquid-phase exfoliation (LPE) methods can provide scalable production of 2D materials in form of liquid dispersion, enabling their processing in thin film through low-cost and industrially relevant deposition techniques.

For all these reasons, the aim of my research work is the production and characterization of 2D materials and their use in energy devices. In particular, I studied the PEC behaviour of group-III and group-IV MMCs flakes, produced by LPE in an eco-friendly solvent (2-propanol). The LPE-produced MMCs flakes dispersions were processed by spray coating to fabricate the photoelectrodes.

Firstly, the as-produced MMCs flakes photoelectrodes were characterized for the first time under simulated sunlight for water splitting reactions: hydrogen evolution reactions (HER) and oxygen evolution reactions (OER).

The PEC properties of the MMCs flakes were also exploited to conceive PEC-type photodetectors, investigating the photoresponse under different illumination wavelengths and in different pH solutions, *e.g.*, ranging from acidic to alkaline conditions.

In parallel, during my PhD, I have also studied $PtTe_2$ crystals, a TMD whose application potential in optoelectronics is still unexplored. The surface structure of $PtTe_2$, the surface lattice constant as well as the dependence on surface temperature were investigated. I also investigated the electron-

phonon coupling constant ($\lambda_{e\text{-}ph}$) of $PtTe_2$ and the broadband excitation spectrum of bulk crystals and thin layers of $PtTe_2$.

In detail, the organization of this Thesis is reported below.

Chapter 1 gives an overview of 2D materials (*i.e.*, graphene, TMDs, MMCs, and their applications).

Chapter 2 provides the production methods of 2D materials.

Chapter 3 reports the morphological, optical, and structural characterization of 2D MMCs.

Chapter 4 presents a brief introduction of PEC water splitting and the main figures of merit, as well as the corresponding characterization techniques. In particular, I investigated the PEC properties of as-produced gallium selenide (GaSe) and germanium selenide (GeSe) flakes.

Chapter 5 describes the use of solution-processed materials (GaSe, GeSe, and GaS) for the realization of PEC-type photodetectors.

Chapter 6 shows the surface and electronic characterization of $PtTe_2$ layered material.

Finally, **Conclusions** and **Appendix A** report the main results of this thesis and a description of the experimental techniques used for the characterization of 2D materials, respectively.

Chapter 1

2D Materials Family: structure and proprieties

In this chapter, a brief overview of the main classes of two-dimensional (2D) materials is reported. In particular, their morphological, optical, electrical, and electrochemical properties are discussed, and the resultant applications due to their properties.

1.1 *Graphene*

Graphene is a 2D crystal formed by carbon atoms arranged in a hexagonal honeycomb structure and it represents the basic building block of other important allotropes, see **Figure 1** [1], [2]. In fact, graphene can be arranged spherically, rolled, or stacked forming (0D) fullerenes, (1D)

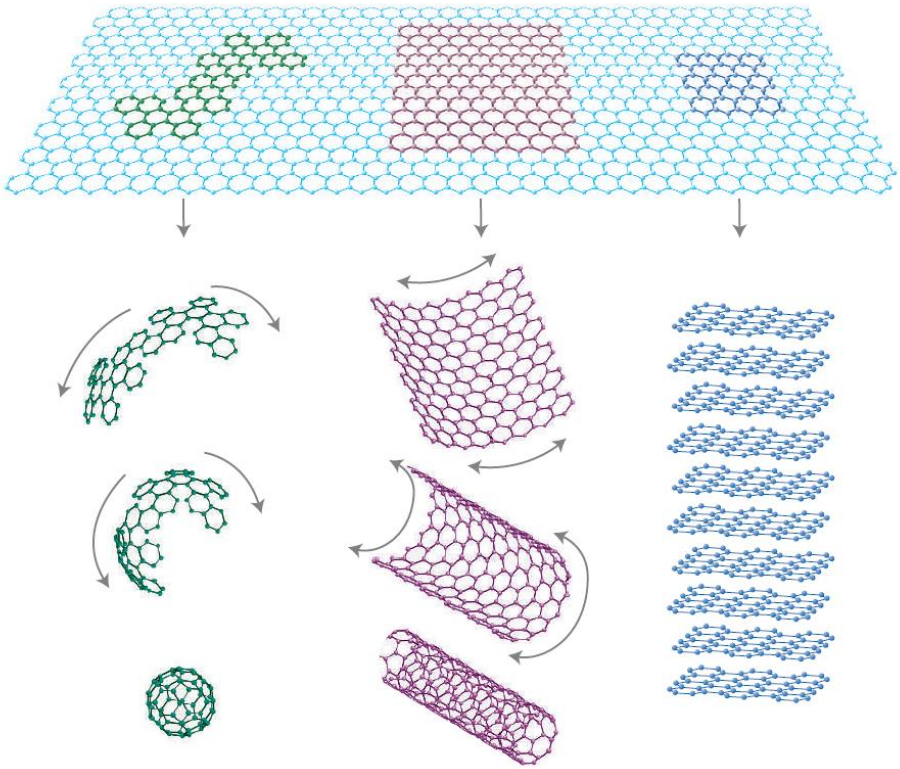

Figure 1: Representative allotropes of carbon. The image is taken from [1].

nanotubes, or (3D) graphite, respectively. A fullerene is a spherical structure with hexagonal and

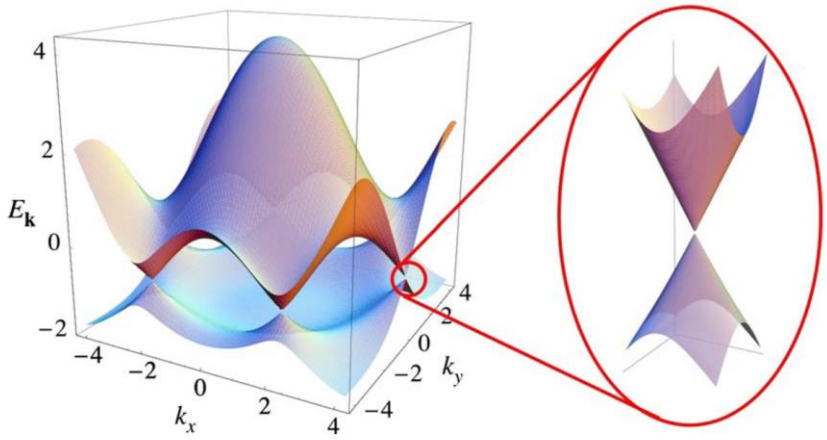

Figure 2: Plot of electronic band structure of graphene. In inset there is the zoom of one of the Dirac points, where the valence band and the conduction band meet. Picture by [10].

pentagonal rings made up of carbon named C_{60}, where the suffix represents the number of sp^2 hybridized carbon atoms in the structure [3]. Carbon nanotubes (CNTs) are obtained by rolled-up of one or more layers of graphene (indicated with single-wall, SWCNT, or multi-wall, MWCNT), and their names are derived from their cylindrical structure [4]. The CNTs show a metallic or semiconducting behaviour, depending on the orientation of the graphene lattice with respect to the CNT axis. Due to their electrical, mechanical, and thermal properties [4]–[6], CNTs have been studied as electrode for batteries, supercapacitors, fuel cells, biomedical applications, etc [7], [8]. Finally, graphite, which is natural 3D counterpart of graphene, consists of carbon layers, separated by a distance of 0.335 nm [9]. Graphite is a semimetal and is the most stable allotropic form of carbon.

1.1.1 Graphene properties

Graphene is a two-dimensional sheet of carbon atoms. Thanks to the hybridization sp^2, the 2s, $2p_{x,}$ and $2p_y$ orbitals generate the strong covalent bond σ in the plane. The remaining $2p_z$ orbital,

perpendicular to the graphene plane, forms the weaker π bonds, responsible for the semi-metallic band structure [2]. In fact, the empty conduction band π* and the occupied valence band π meet in the K points of the Brillouin zone (called Dirac points), see **Figure 2** [10]. This makes graphene a zero-gap semiconductor and the electrons, in the vicinity of the Fermi level, obey a linear dispersion relation, behaving like massless fermions Dirac [11], [12]. These features are responsible for most of the peculiar electronic properties of graphene [10], [11]. In fact, the graphene shows an electron mobility of ~ 25000 $cm^2\ V^{-1}\ s^{-1}$ at room temperature (RT) [13]. In addition, because of the strong and anisotropic bonding of the carbon atoms, graphene possesses an extraordinary high RT thermal conductivity in the range of 4800 – 6000 $W\ m^{-1}\ K^{-1}$ [14]. Graphene exhibits unique mechanical properties. The first study reported that Young's modulus of graphene is of 1.1 TPa and breaking strength of 42 $N\ m^{-1}$ [15]. Additionally, thanks to its low thickness, graphene absorbs only 2.3% of visible light [16]–[18]. Therefore, graphene represents a viable candidate for optoelectronic applications as a transparent conductor [12].

1.2 Transition Metal Dichalcogenides (TMDs)

Transition Metal Dichalcogenides (TMDs) constitute a large family of layered materials with the formula MX_2, where M is a transition metal of the group 4 to 10 and X is a chalcogen atom such as sulphur (S), selenium (Se) or tellurium (Te). A sandwich of three atoms composes each TMD's single-layer, where the metal atoms are in the centre of the structure, while the chalcogenides atoms are located at the edges of the structure (X – M – X). In layered TMDs, there is a strong

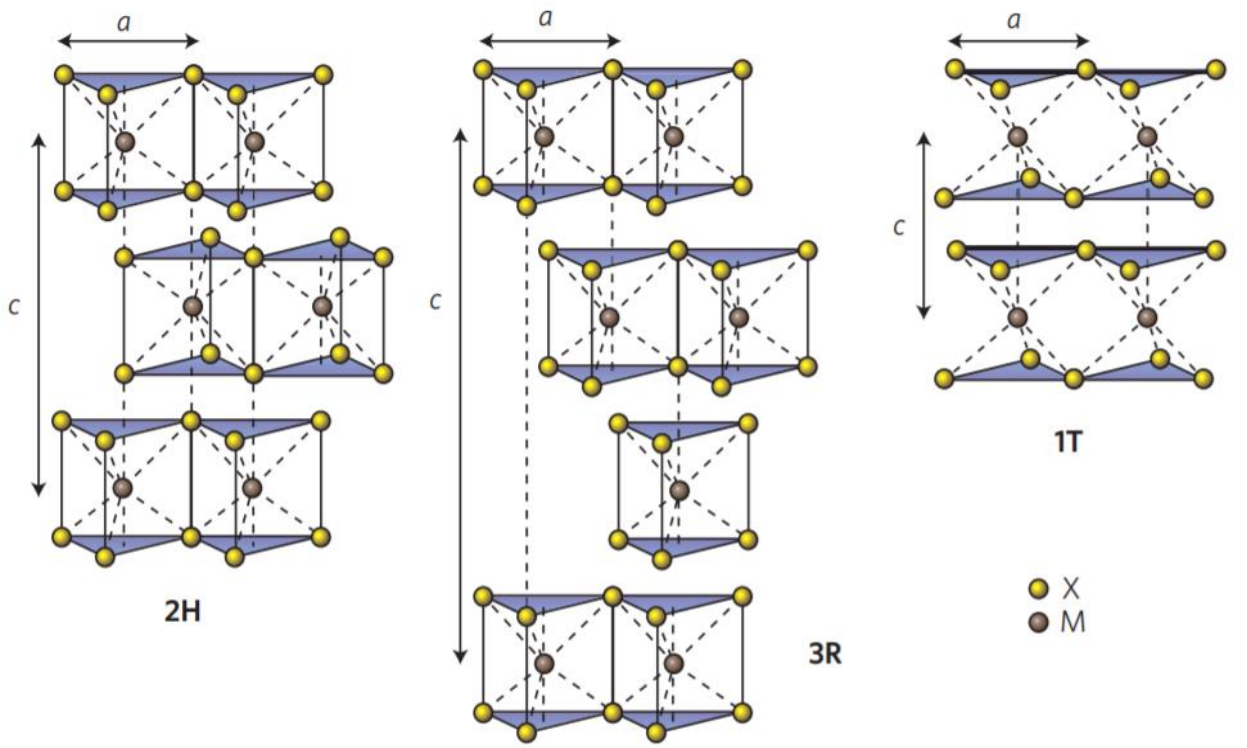

Figure 3: Schematics of the structural polytypes of TMDs from left to right 2H (hexagonal symmetry), 3R (rhombohedral symmetry) and 1T (tetragonal symmetry). Adapted from [19].

intralayer covalent bonding and weak interlayer van der Waals forces. The overall symmetry of TMDs is hexagonal or rhombohedral, and the metal atoms have octahedral or trigonal prismatic coordination [19]. The symmetry adopted by a TMD depends on *d*-electrons count of the M [20]. The compounds of group 4 form an octahedral structure while both structures octahedral and trigonal prismatic can be found in the group 5 of the TMDs. On the other hand, the species of groups 6 and 7 are typically in a trigonal prismatic and a distorted octahedral geometry, respectively. Finally, TMDs of the group 10 display octahedral coordination [20]. Bulk TMDs may exist in several polymorphs but the most common are 2H, 3R or 1T, where the *c* axis defines the unit cell (**Figure 3**). For example, TaS_2 shows several phases, such as 2H-TaS_2 or 3R-TaS_2 [21].

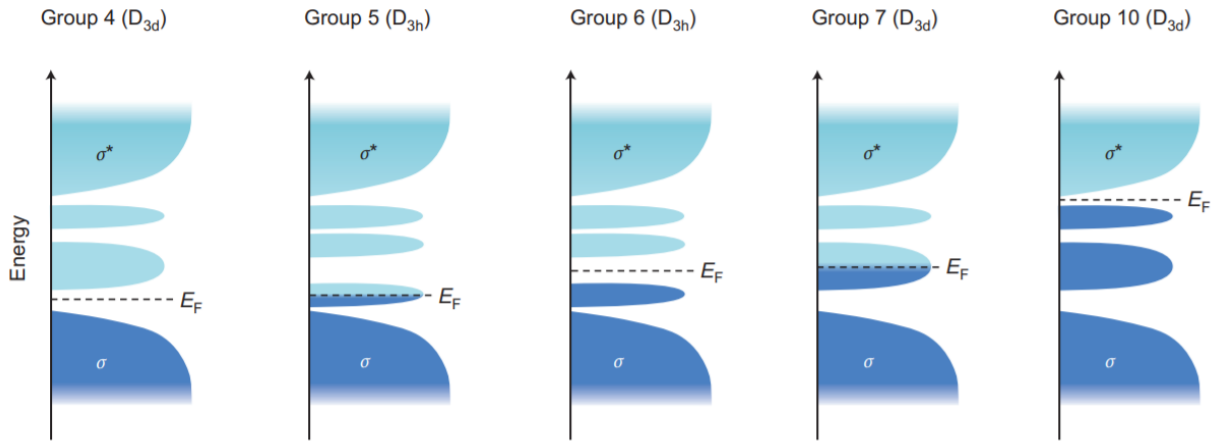

Figure 4: Schematic illustration of the density of states of different TMD groups. Adapted from [20].

The electronic structure of TMDs strongly depends on the coordination of the transition metal and its *d*-electron count[20]. As displayed in **figure 4**, the non-bonding *d*-bands of the TMDs are positioned between the bonding (σ) and anti-bonding (σ^*) bands for the 2H and 1T phases, respectively. When the M is coordinated octahedrally, there are two degenerate *d*-orbitals (d_{z^2,x^2-y^2} and $d_{yz,xz,xy}$), while for the trigonal prismatic coordination, there are three degenerate *d*-orbitals (d_{z^2}, $d_{x^2-y^2,xy}$ and $d_{xz,yz}$) [22]. Depending on the progressive filling of the σ^* from group 4 to group 10 species, TMDs can be metallic (such as NbS_2), semimetallic (such as $TiSe_2$), semiconducting (such as WS_2) or insulators (such as HfS_2) [20]. Additionally, superconductivity and charge-density wave effects have been observed in some TMDs, such as $NbSe_2$ and TaS_2 [20], [23].

Due to their structures, TMDs can be exfoliated from bulk to single- or few- layers. In their 2D form, TMDs exhibit properties that are different from those of their 3D counterpart. For example in the case of 2D MoS_2 or WS_2, the quantum confinement effects regulate the optical and electronic, leading to a transition from indirect to direct bandgap when the thickness is reduced from bulk to monolayer [23], [24]. This indirect-to-direct bandgap evolution is demonstrated by the presence of strong photoluminescence (PL) and large exciton binding energy shown by TMD

monolayers [20], [23]. For example, in the MoS_2 the indirect band gap (E_g) of the bulk is 1.3 eV, while in the monolayer there is a direct E_g of 1.9 eV, which induces a giant PL, good mobility (~ 700 $cm^2\ V^{-1}\ s^{-1}$), high current on/off ratio of ~ 10^7 - 10^8 and large optical absorption (~ $10^7\ m^{-1}$ in the visible range) [23]. These properties, combined with their large surface area, make 2D TMDs promising candidates for a large variety of applications, such as photo-detectors, solar cells, light-emitting diodes [23].

1.2.1 Platinum Ditelluride ($PtTe_2$)

Bulk 1T-$PtTe_2$ is a type-II Dirac semimetal with strongly tilted Dirac points along the Γ-A direction [25], [26]. The $PtTe_2$ crystal presents a trigonal CdI_2-type crystal structure, ($P\bar{3}m1$ space group), where six Te atoms surround the central Pt atom building the $PtTe_6$ octahedra along the basal plane [27]. From theoretical studies [28], [29], the $PtTe_2$ electronic properties are thickness-dependent. When it is exfoliated, passing from the bulk to the monolayer form [25], it undergoes a transition from semimetal to semiconductor, showing a small indirect bandgap between 0.38 – 0.67 eV [25], [30], [31]. At the same time, the electrical conductivity strongly depends on the thickness. In fact, the 2D $PtTe_2$ shows a high electrical conductivity of $10^7\ S\ m^{-1}$ at room temperature, which is 1000 times higher with respect to MoS_2 [32]. Moreover, $PtTe_2$ exhibits a promising catalytic behaviour for hydrogen evolution reaction [31], [33], and the pristine surface of $PtTe_2$ crystal is chemically inert toward common ambient gases [26]. As a result of its properties, this material can find application in (opto)electronic, photonic and (photo)catalytic devices [26], [27], [32], [34], [35].

1.3 Metal Monochalcogenides (MMCs)

The family of the group-III and -IV metal monochalcogenides layered semiconductors (MMC) have attracted huge attention thanks to their unique physical and chemical intrinsic properties [36],

[37]. Like TMDs, MMCs structure exhibits strong in-plane bonds and weak bonds between layers [38]. Most of MMCs are semiconductors with a larger band gap as the number of layers decreases. In recent years, 2D MMCs received attention due to their potential use in energy conversion applications, high-sensitivity photodetectors, field-effect transistors, flexible all-solid-state supercapacitors, and electrochemical sensing [37]–[41].

1.3.1 Group-III Monochalcogenides: Gallium Selenide (GaSe) and Gallium Sulfide (GaS)

Gallium selenide and gallium sulfide are two compounds of the group-IIIA monochalcogenides. Their crystal structures consist of four atomic layers vertically stacked X-Ga-Ga-X, where X is Se or S, kept together by van der Waals forces [42]. Depending on layer stacking order, four different polytypes (β, γ, δ and ε) can be obtained [43]. The most common polytype for GaSe is ε-phase (space group symmetry $P\bar{6}m\text{-}D'_{3h}$), while GaS crystallize in the is β-phase (space group symmetry…$P6_3/mmc$ (D_{6h})) [44]. The GaSe shows a pseudo-direct optical band gap, ranging from ~ 1.8 eV for the bulk to ~ 2.6 eV for the monolayer[43], which is only 25 meV higher than its indirect E_g [45]. Meanwhile, some studies reported for GaS a large indirect band gap of ~ 2.4 eV (direct E_g ~ 3.2 eV) for the bulk [43], [46], that exceeds 3 eV in the single-layer form [47]. Due to their anisotropic structural and distinctive optoelectronic properties, these materials have been successfully exploited in nonlinear optical applications and photodetectors [48]–[51]. In particular, GaS is a promising material for the implementation in photodetectors suitable to detect light in the ultraviolet (UV) range, thanks to its wide bandgap [52], [53]. In addition, theoretical calculations have demonstrated mechanical stability of 2D GaS [54] with excellent oxidation resistance, showing high activation energy (E_a = 3.11 eV) for dissociation and chemisorption of O_2 molecules [55] and a satisfactory thermal stability [56]. Moreover, group-IIIA monochalcogenides are

promising (photo)catalytic materials for energy conversion applications, such as water splitting [43], [47], [57], [58].

1.3.2 Group-IV Monochalcogenide: Germanium Selenide (GeSe)

Germanium selenide is an orthorhombic crystal with a phosphorene-derived distorted NaCl-type structure ("black-phase structure") formed by strong covalent bonding within the layers and weak van der Waals interaction between the adjacent layers [59]–[61]. The GeSe crystal shows different polymorphs (α, β, γ, δ and ε) [62]–[64]. Among them, the most common allotropic form is β-GeSe that crystallizes in the orthorhombic space group *Pnma* [64], [65]. The GeSe polymorphs have been studied in several applications, such as photovoltaics [66], [67], photodetectors [68], field-effect transistors [69], ferroelectric devices [70], and energy storage systems [71]. Moreover, GeSe, which can be easily exfoliated in the 2D form, has attracted significant attention due to its many advantages, such as high stability, oxidation resistance, and earth-abundance, which makes it a suitable material in applications of semiconductors [41], [72]. Theoretical studies demonstrated a band gap-dependence with the number of the layers, showing a direct bandgap in the monolayer crystals > 1.9 eV [61], [73]. Due to its high absorption coefficient in the visible spectral range (~ 10^5 cm^{-1}) and its high charge carriers mobility (10^2 - 10^4 cm^2 V^{-1} s^{-1} for electrons [73]–[75] and between 1 and 10^3 cm^2 V^{-1} s^{-1} for holes [73]–[75]), 2D GeSe can find application in photo(electro)chemical devices [73], [76].

Chapter 2

Production Methods

Two-dimensional materials can be obtained by a large number of methods, which can be divided into two classes, *i.e.*, bottom-up and top-down production approaches [77]. In bottom-up processes, atoms are bonded together to directly grow 2D materials on top of the substrate. In top-down processes, the bulk material is exfoliated layer by layer in order to obtain 2D material counterpart. The bottom-up techniques, including chemical vapour deposition (CVD) or molecular beam epitaxy (MBE) ones, allow high-quality nanosheets to be produced with a small number of defects [78]. Nevertheless, these approaches suffer from a very low yield and high production cost, and cannot satisfy the request on the large-scale. On the other hand, a large-scale production and

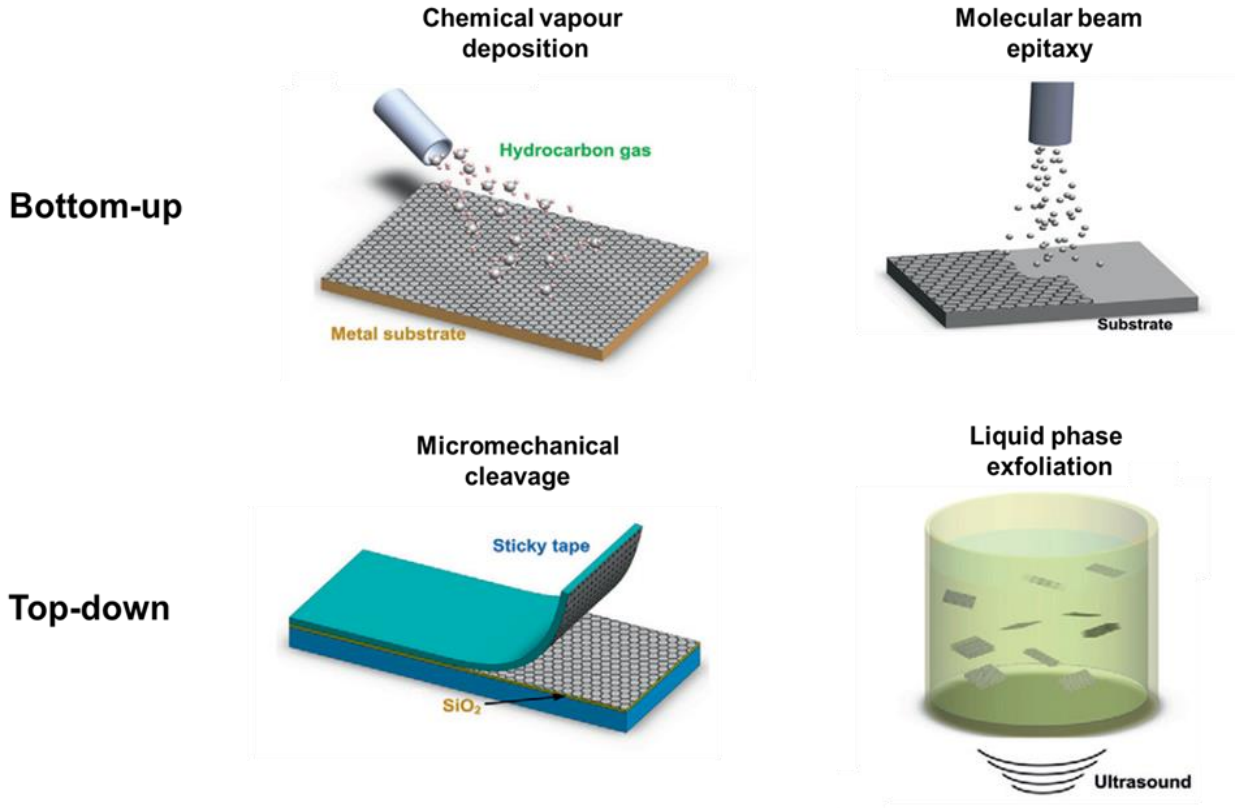

***Figure 5*:** Schematic illustration of some of the main top-down (micromechanical cleavage and liquid phase exfoliation) and bottom-up (chemical vapour deposition and molecular beam epitaxy) 2D crystal production approaches. Adapted from [77].

low cost are obtained with top-down techniques [79], such as mechanical exfoliation or liquid phase exfoliation (LPE). In this section, some of these methods will be explained (**Figure 5**).

2.1 Micromechanical exfoliation

The micromechanical exfoliation, known also as micromechanical cleavage (MC), was used to isolate of graphene from graphite in 2004 by A. K. Geim and K.S. Novoselov [80]. After the successful exfoliation of graphite, many other defectless monolayer materials have been obtained in a reliable way. The most common method for the mechanical exfoliation includes the *scotch-tape* technique, as shown in **Figure 6**, in which an adhesive tape is applied to the surface of the bulk crystal, exerting a normal force [78]. By repeatedly peeling the crystal, flakes with different thicknesses are produced[81]. Recently, it has been reported a novel technique that makes use of the so-called "gold tape", to disassemble layered bulk crystals into monolayers with lateral size

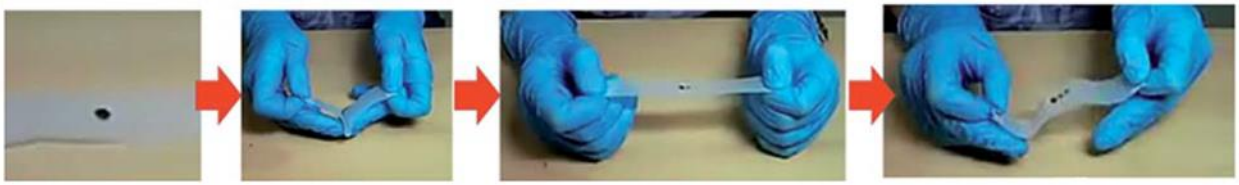

Figure 6: Photograph of mechanical exfoliation. Adapted from [78].

limited by bulk crystal dimension (~ few mm) [82]. The obtained monolayers present similar quality, in terms of defects, to the flakes from conventional scotch tape exfoliation. However, despite all the progresses and improvements, the mechanical exfoliation technique still suffers from disadvantages in terms of yield, being impractical for large-scale applications.

2.2 Liquid phase exfoliation

To overcome the problems of low yield and a production rate introduced with the mechanical exfoliation [83], liquid media can be used to exfoliate layered compounds in large amounts [83]–

[85]. These techniques, classified as liquid-phase exfoliation methods, allow 2D materials to be formulated in form of inks, that can be processed by means of consolidated industrial techniques[83]. In literature, several liquid-phase exfoliation approaches have been reported for layered materials, including ultrasonication-assisted exfoliation [77] and the wet-jet milling exfoliation [86], [87], which are discussed in the following section.

All liquid-phase methods have three different steps in common (**Figure 7**):

1. Dispersion of the bulk material in a liquid medium;
2. Exfoliation process by a driving force (*i.e.*, ultrasounds, shear forces);
3. Purification.

2.2.1 Dispersion

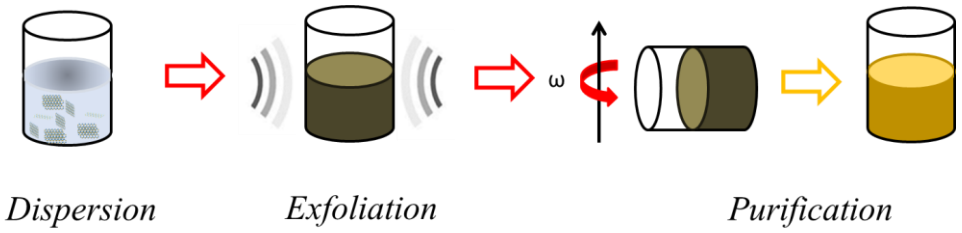

Figure 7: Schematic illustration of the three steps involved in the LPE process. Adapted from [57].

The choice of the solvent plays a crucial role in the exfoliation [77]. Solvents suitable for dispersion are those whose surface energy (E_{sur}) matches the surface tension of the liquid (γ) [88]. For the case of graphene, stable dispersions can be achieved for solvents surface tension near to $\gamma \sim 46.7$ mN m^{-1} [88] In this case, the flakes tend to adhere to each other and the work of cohesion between them is high (*i.e.*, the energy per unit area required to separate two flat surfaces from contact), hindering their dispersion in liquid [89]. Besides, the Hansen (or Hildebrand) parameters (namely, the energy from dispersion forces between molecules (δ_D), the energy from dipolar

intermolecular force between molecules (δ_P) and the energy from hydrogen bonds between molecules or electron exchange parameter (δ_H)) and the viscosity (η) are also important factors in the choice of the solvent [88]. Extensive experiments have demonstrated that in the case of graphene[88], and also in many other layered materials [83], N-Methyl-2-pyrrolidone (NMP) and Dimethylformamide (DMF) showed the most suitable values for γ (40 - 50 mN m^{-1}), Hansen parameters ($\delta_D \sim 18$ $MPa^{1/2}$, $\delta_P \sim 10$ $MPa^{1/2}$, $\delta_H \sim 7$ $MPa^{1/2}$ for graphene) and η (0.93 - 1.59 mPa s), being the best candidates for stable dispersions [84], [88], [90], [91]. Unfortunately, toxicity [92] and high boiling point (~177 °C) [93] are critical issues when the dispersions are deposited onto a substrate. For this reason, the use of green solvents with lower boiling points (such as acetone [94] and isopropanol [95] can be a solution, by tuning their rheological parameters by adding stabilizing agents like polymers and surfactants [84]. However, the use of polymers/surfactants strictly depends on the target application because their residues can increase the inter-flake contact resistance [96].

2.2.2 Exfoliation

The exfoliation of the bulk material in a liquid medium can be carried out by different approaches. In my thesis work, I used the ultrasonication-assisted exfoliation [95] and the wet-jet milling (WJM) exfoliation techniques [86]. The ultrasonication technique consists of dispersing the bulk material into the solvent while ultrasound vibrations, which are transmitted to the sample, provide the driving force needed for the material exfoliation. The physical principle of the ultrasonication

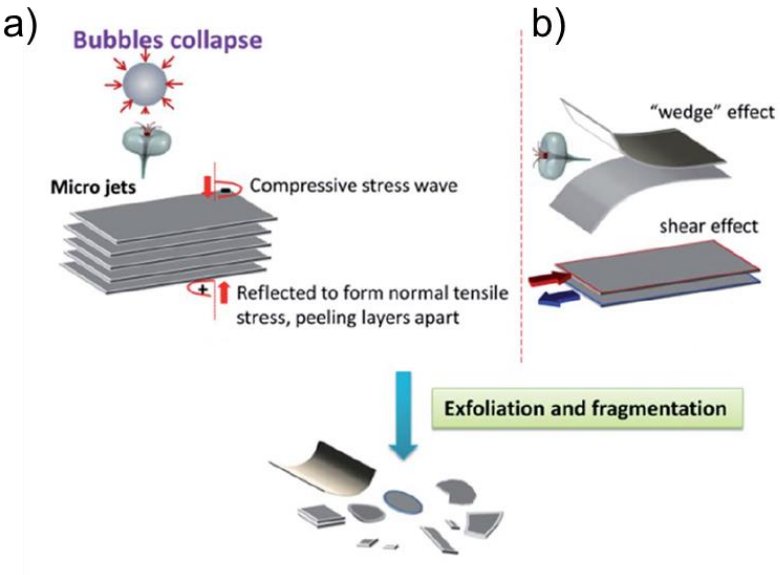

Figure 8: Illustration of the mechanism for exfoliation via sonication, showing a) collapsing cavitation bubbles acting as compressive stress waves and b) the effect of shear forces. Adapted from [78].

of layered materials is based on cavitation. In particular, as shown in **Figure 8a**, collapsing cavitation bubbles that surround the bulk crystal act as compressive stress waves, which propagate into the sample inducing exfoliation. Another effect on the exfoliation is due by the shear forces, which effectively separate the layers (**Figure 8b**). The ultrasonication of layered crystals can take place with ultrasonic baths or probes [97].

In the first case, the ultrasonic waves propagate through the water bath, setting up a standing wave [77], [83]. The intensity of the waves is affected by the presence of the acoustic absorption. For this reason, the energy acting on the sample is partially transformed into heat, resulting in an intensity nominally lower than expected [84]. In the second case, ultrasonic probes are directly immersed in the solution, generating locally higher powers compared to the ultrasonic bath [77], [88], [98]. In this context, sonication power, frequency, exfoliation time, temperature are important parameters to consider in order to obtain flakes with desired thickness and lateral size

[97]. For example, Khan et al. [99] have shown that the lateral size of graphene flakes decreases with sonication time (t), scaling as $t^{-1/2}$. However, the more sonication times are, the greater the defects. Indeed, for more sonication time (above 2 hours) the defects, besides being on the edges of the flakes, also occur on the basal plane [100]. On the other hand, fragmentation of the material, as well as poor scalability and reproducibility, are the main limitations of the ultrasonication-assisted technique [101].

For this reason, A. E. Del Rio Castillo et al. [86], introduced a novel approach called wet-jet milling technique, which overcomes the drawbacks presented by the ultrasonication approach. The WJM technique copes with the possibility to exfoliate several bulk layered crystals (such as, graphite, hexagonal-boron nitride, and TMDs among the others) in form of single-/few-layer flakes dispersed in solvents, resulting in a cost-effective production of 2D crystals without compromising the integrity of the starting materials [86]. Basically, the WJM exfoliation process comprises a first step of preparing a dispersion of bulk layered crystals in a suitable solvent, and a subsequent exfoliating step in which hydrodynamic forces cause the shear stress exfoliating the layered crystals. As shown in **Figure 9a, b**, an hydraulic piston supplies the pressure (180 – 250 MPa) to push the bulk crystal/solvent mixture into the processor (a set of 5 different perforated and interconnected disks) where two jet streams are generated. Nozzles with different sizes (between 0.1 – 0.3 mm⌀) generate the compression of the dispersant fluid phase [86], [87]. Thus, the jet streams collide in the nozzle, generating the shear forces that cause the layered crystal exfoliation [86]. By decreasing the size of the nozzle, it is possible to tune the thickness and the lateral size of the flakes.

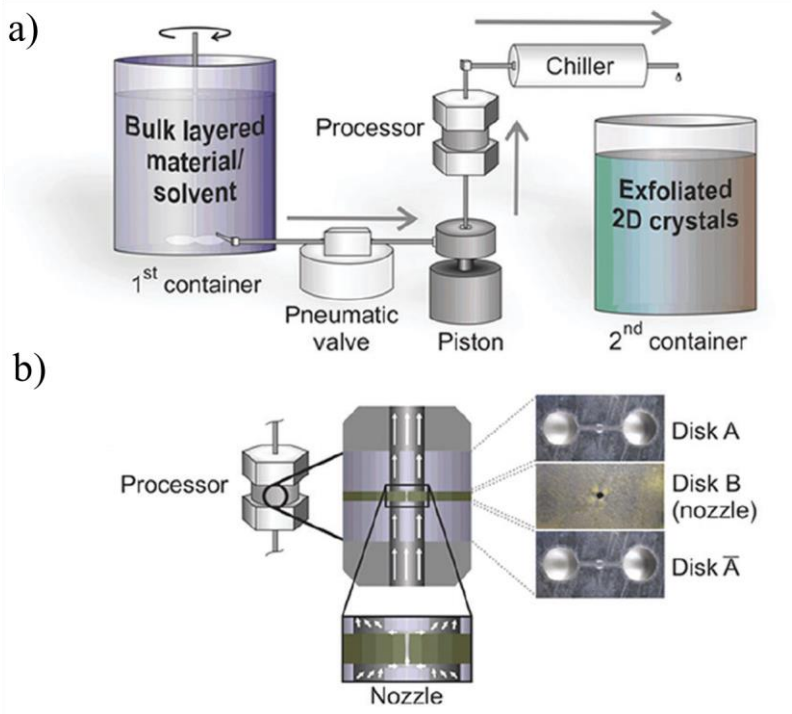

Figure 9: Schematic illustration of the wet-jet mill system [86].

Immediately after, the sample is cooled down in form of a liquid dispersion by means of a chiller [86], [87].

Overall, the WJM process enables the large-scale production (litre scale) of defect-free and high quality single-/few-layers crystal dispersions (gram per litre-scale), in short times (second-scale), which can be used in context that require a large amount of 2D materials [86]. For instance, in the case of graphene, a concentration of 10 g L^{-1} is achieved for both single- and few-layer 2D crystal flakes dispersion [86], [87]. The exfoliation yield, defined as the ratio between the weight of the processed material and the weight of the starting graphite flakes, is 100% with an average time to produce one gram of exfoliated graphite is 2.55 min [86]. Therefore, the WJM process has a production capability of single-/few-layer crystals up to 2 L h^{-1} [86].

2.2.3 Purification

After the exfoliation process, a heterogeneous composition, containing flakes of different thickness (and, in some cases, even un-exfoliated materials), is produced. For this reason, the as-prepared dispersion must be purified *via* sedimentation-based separation (SBS) [91], consisting of ultra-centrifugation process. Thanks to SBS, it is possible to separate the thinnest flakes from the thickest ones by exploiting their sedimentation rate in response to a centrifugal force applied on them.

The sedimentation coefficient (*s)*, which is the time needed for flakes to sediment, is described by the Svedberg equation [102], [103]:

$$s = \frac{m(1 - \vartheta'\rho)}{f}$$

where ϑ' is the partial specific volume (the volume that each gram of the solute occupies in solution), ρ is the density of the solvent, f is the frictional coefficient due to the motion through the solvent towards the bottom of the ultracentrifuge tube. As shown by the previous equation, thick and large flakes (having larger mass), sediment faster than small and thin flakes (having smaller mass), which are thus maintained in dispersion during the SBS process. Thus, dispersions with flakes of different lateral sizes can be obtained by tuning the centrifugal forces [77], [84].

2.3 Chemical vapour deposition

Chemical vapor deposition (CVD) is one of the main bottom-up techniques allowing the deposition of thin films of several 2D materials [77], [104], [105], as well as crystalline or amorphous crystals, among them polycrystalline silicon [106] and diamond [107], from solid, liquid or gaseous precursors of many substances [108]. The temperature of the substrate, temperature ramp, and

growth duration are fundamental growth parameters that define the type of occurring reaction, which must be tuned carefully to obtain high-quality 2D crystals. Several precursors are vaporized and transported into the deposition chamber and, subsequently, are combined in a reaction chamber. The combined gases are exposed to the substrate, which is heated at elevated temperatures (> 600 °C) under low pressure (10^{-7} mPa). Thus, the precursors flow into the furnace and their molecules react near the catalytic surface, leaving the atoms free to diffuse inside the catalyst or on its surface, forming a material film on the substrate surface. Consequently, the temperature is decreased down to room temperature, allowing for the nucleation of crystals' atoms on the substrate, combining into larger clusters. Finally, waste gases are then pumped out from the reaction chamber.

Despite with this technique it is possible to obtain high-quality crystals, unfortunately, the CVD approach is interesting for proof-of-concept devices [109], [110], or for high-added-value applications due to the expensive equipment, [111] as well as the high energy needed for the device fabrication [112].

2.4 Molecular beam epitaxy

Molecular beam epitaxy (MBE) is a technique widely used and well suited for the deposition and growth of high-quality epitaxial structures, such as graphene, III-V, or II-VI semiconductors [113], on a variety of substrates such as SiC [114], Al_2O_3 [115], [116], Mica [117], [118], SiO_2 [117], Ni [119], Si [120], h-BN [121], MgO [122], etc., in the 400 – 1100 °C range, to obtain crystals with atomic thickness [113]. This technique can be used in research and in industrial applications in markets where highly specialized devices are required, such as for semi-transparent large-area electrodes, most of all in view of integration with Si technology. Since MBE is a thermal process, crystals will be deposited in the amorphous or nanocrystalline phase [77].

Nevertheless, these layered crystals are produced with a large domain size distribution of defective crystals [119], due to the lack of layer control [119], because MBE is not a self-limited process, relying on the reaction between the deposited species [113].

In fact, despite the conceptual simplicity, a great technological effort is required to produce systems that yield the desired quality in terms of materials purity, uniformity, and interface control. For example, the control of the vacuum environment and the quality of the source materials should allow higher crystal quality compared to non-ultra-high vacuum (UHV)-based techniques [84].

However, it may be possible to produce large-area single crystal on a wide variety of dielectric and metallic substrates, with further optimizations. In addition, the fine-control of doping, and the growth of hybrid heterostructures, it has been investigated. Moreover, the use of chemical beam epitaxy (CBE) [123] to grow graphene in a catalytic mode can be also studied, taking advantage of the CBE ability to grow or deposit multiple materials, such as dielectrics [124] or layered materials, on the top of graphene, to form heterostructures.

Chapter 3

Characterization of 2D Metal Monochalcogenides (MMCs)

This chapter provides a detailed morphological and structural characterization of 2D crystals-based dispersions (GaSe, GaS, and GeSe) obtained by sonication-assisted LPE approach.

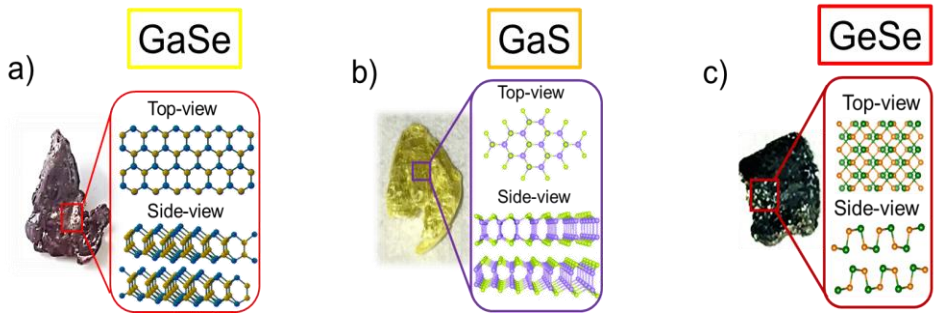

Figure 10: Photographs of the as-synthetized GaSe crystal with the a) GaSe, b) GaS and c) GeSe crystal structures top and side view [127], [128], [129].

In this work, the GaSe, GaS, and GeSe crystals (see **Figure 10**), obtained through direct synthesis by Bridgman-Stockbarger method [125], were exfoliated in the 2D form by ultrasonicated-assisted LPE in anhydrous 2-propanol (IPA - ACS Reagent, ≥ 99.8%, Sigma-Aldrich), followed by SBS.

Table 1. Exfoliation parameters used for the production of the samples.

Material	Starting Concentration	Sonication Time	Centrifuged Parameters
GaSe	1 g L^{-1}	15 h	700g for 20 min at 15 °C
GaS	1 g L^{-1}	15 h	900g for 20 min at 15 °C
GeSe	1 g L^{-1}	15 h	700g for 20 min at 15 °C

Briefly, 50 mg of crystals were pulverized and added to 50 mL of solvent and ultracentrifuged in a bath sonicator (Branson® 5800 cleaner, Branson Ultrasonics). The as-produced dispersions were ultracentrifuged (Optima™ XE-90 with a SW32Ti rotor, Beckman Coulter) and separated from un-exfoliated bulk crystals, collecting approximately 80% of the supernatant from the batch. **Table 1** reports the exfoliation parameters of all materials. The use of IPA as the solvent presents significant benefits in processability thanks to its non-toxicity and low-boiling point (82.5 °C) [93]. Moreover, this solvent has been successfully used to exfoliate the monochalcogenides of group-III and group-IV transition metal [49], [57], [126]–[129].

The morphology of the samples was characterized by transmission electron microscopy (TEM) and atomic force microscopy (AFM) techniques in order to evaluate their lateral dimension and thickness, respectively. The concentration of all dispersions was evaluated by optical absorption spectroscopy. Finally, the Raman spectroscopy and X-ray diffraction (XRD) were carried out to observed the structural properties and surface chemical composition. More details about the characterization techniques are reported in Appendix A.

3.1Morphological characterization

The morphology of the MMCs-dispersions was characterized by means of TEM and AFM in order to evaluate the lateral size and the thickness value of the flakes, respectively. **Figures 11a-c** report representative TEM images of GaSe, GaS, and GeSe flakes, respectively, whereas the correspondent statistical TEM analysis are shown in **Figure 11g-i**. The TEM images were acquired with a JEM 1011 (JEOL) TEM (thermionic W filament), operating at 100 kV. The samples were prepared by drop casting the dispersions onto ultrathin C-on-holey C-coated Cu grids and dried overnight under vacuum. The morphological and statistical analyses were performed using ImageJ

software (NIH) and OriginPro 9.1 software (OriginLab), respectively. While the GaSe and GeSe flakes display irregular shapes with sharp edges, the GaS flakes present a nearly rectangular shape and regular edges. The lateral size data follow a log-normal distribution, peaked at ~ 45, ~ 67.5, and ~ 36 nm for GaSe, GaS, and GeSe, respectively.

The representative AFM images of all samples are shown in **Figure 11d-f.** The AFM images were taken with an XE-100 AFM (Park System, Korea) equipped with PPP-NCHR cantilevers (Nanosensors, Switzerland) having a tip diameter <10 nm. The images were collected in

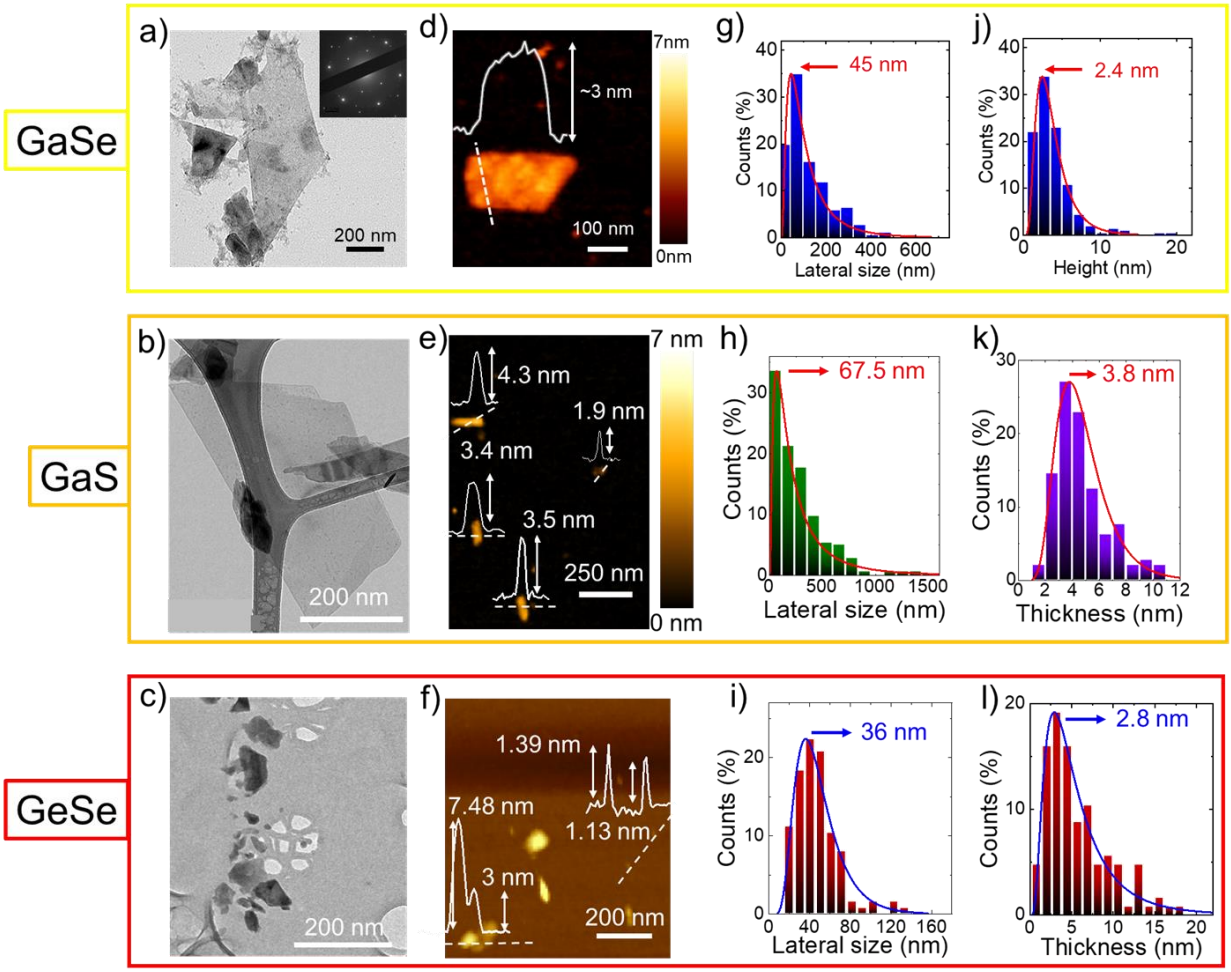

Figure 11: Morphological Characterization of MMCs materials: GaSe (yellow box), GaS (orange box) and GeSe (red box). a-c) TEM and d-f) AFM images with relative statistical distributions of (g-i) lateral size and (j-l) thickness, respectively [127], [128], [129].

intermittent contact (tapping) mode and processed through Gwyddion 2.53 software (http://gwyddion.net/). For AFM samples preparations, the dispersions were deposited by drop casting onto mica sheets (G250-1, Agar Scientific Ltd.) in N_2 and heating to 100°C for 15 - 20 min to dry the sample and remove solvent residues. The measured height profiles ranging between 1.1 and 7.5 nm are attributed to few (≤ 5)-layer flakes, considering the thicknesses of monochalcogenides monolayers (values in the range 0.75 – 1.5 nm [72], [130]–[132]). From AFM statistics (**Figure 11j-l**), fitted by a log-normal distribution, the estimated thickness values of the GaSe, GaS and GeSe flakes are ~ 2.4, ~ 3.8, and ~ 2.8 nm, respectively, where the statistical data were analyzed by using OriginPro 2018 software.

3.2 Optical and structural characterization

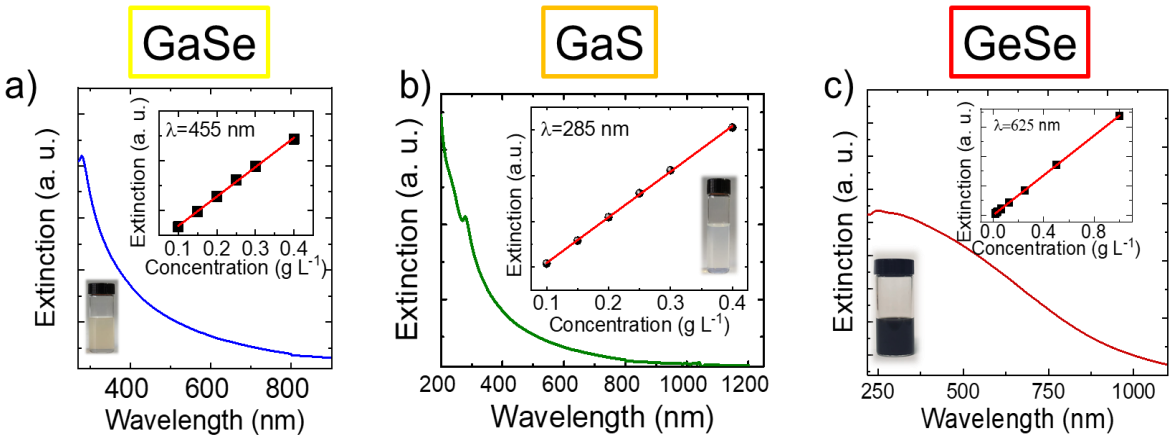

Figure 12: Optical extinction measurements of the a) GaSe, b) GaS and c) GeSe dispersion. The top insets report the extinction *vs* known volume of the dispersions. The bottom inset display a photografh of samples exfoliated in IPA [127], [128], [129].

The optical extinction measurements were carried out in order to evaluate the concentration of the dispersions. The measurements on nanoflakes dispersion were performed using a Cary Varian 5000 UV−vis spectrometer. **Figure 12a-c** shows the optical extinction spectrum of the GaSe, GaS, and GeSe dispersion, respectively, while the slopes of the linear fitting of the extinction *vs* concentration (Ext(λ) *vs* C) plot are reported in the insets. Optical extinction measurements of

controlled dilutions/concentrations of all samples allow the extinction coefficients to be estimated using the Beer-Lambert Law (see Appendix A.3).

The concentration values of the as-produced dispersions were measured by weighting the solid material content in a known volume of the dispersions. The concentration values of different dispersions and corresponding extinction coefficients are reported in **Table 2**.

***Table* 2.** Values of the different wavelengths (λ), extinction coefficient (ε(λ)) and Concentration (C) for all investigated 2D MMCs samples.

	λ (nm)	ε(λ) (L g^{-1} m^{-1})	C (g L^{-1})
GaSe	455	113	0.20
GaS	285	199	0.20
GeSe	625	136	0.22

The crystal structures of the bulk and exfoliated materials were characterized by XRD and Raman spectroscopy. X-ray diffraction (XRD) measurements were performed by PANalytical Empyrean using Cu Kα radiation. While the Raman spectroscopy measurements were carried out using a Renishaw microRaman Invia 1000 mounting a 50× objective, with an excitation wavelength of 532 nm for GaSe and GaS samples and 633 nm for GeSe and an incident power of 1 mW. The samples for XRD and Raman measurements were prepared by depositing powder crystals of GaSe, GaS, and GeSe and corresponding as-produced dispersions onto Si/SiO_2 substrates and Au-coated Si/SiO_2 substrates, respectively, subsequently dried under vacuum.

The acquired XRD patterns show the hexagonal structure of bulk GaSe and GaS (**Figure 13a, b**) and prove that the crystals, in agreement JCPDS 37-931 and ICSD-173940 cards are found in the most stable (lowest energy) polytype (*i.e.*, ε-GaSe and β-GaS, respectively), as reported in

literature[133]–[136]. The XRD GeSe analysis confirms the orthorhombic (*Pnma*) structure of bulk GeSe, as shown in **Figure 13c**. In the XRD pattern of exfoliated samples does not appear any extra peak, which can be attributed to crystalline impurities.

The crystalline integrity and the absence of other chemical species (*e.g.*, Ga_2Se_3, Ga_2O_3, GeO_2, etc.) in the as-produced monochalcogenides dispersions were also demonstrated by Raman spectroscopy. The Raman measurements were carried out with an excitation wavelength (λ_{exc}) of 532 nm for GaSe and GaS, and 633 nm for GeSe.

The GaSe crystals exhibit two out-of-plane vibration modes A_{1g}^1 at ~ 134 cm^{-1} and A_{1g}^2 at ~ 308 cm^{-1}, and two in-plane vibration modes E_{2g}^1 at ~ 212 cm^{-1} and E_{1g}^2 at ~ 251 cm^{-1}, as shown in **Figure 13d**. In the exfoliated GaSe spectrum, the E_{1g}^2 mode is indistinguishable from the background signal, while A_{1g}^1 and E_{2g}^1 modes shift to lower and higher wavenumbers, respectively. Previous theoretical and experimental studies demonstrate that the softening of the A_{1g}^1 and the strengthening of the E_{2g}^1 with the decrease of the thickness, which can be explained by the reduction of the inter-layer forces [137]. Moreover, the results exclude the signatures attributed to polymorph crystal (*i.e.* Ga_2Se_3), oxidized phase (*i.e.* Ga_2O_3), and amorphous/crystalline Se (a-/c-Se) modes, which are observed at ~ 155 cm^{-1}, [138] ~ 200 cm^{-1}, [139] and between 135 and 160 cm^{-1}, [140]–[142] respectively.

Despite, for GaS, the non-degenerate Raman active optical modes should be six (*i.e*, $2A_{1g} + 2E_{1g} + 2E_{2g}$) [143]–[145], the most experimentally observed are A_{1g}^1, A_{1g}^2 and E_{2g}^1 [143], [144]. The same modes are found in the exfoliated GaS flakes (**Figure 13e**), and their intensities decrease as the number of layers decreases. In the case of few-layer crystals, the A_{1g}^1 peak position undergoes a red-shift compared to the bulk crystal, due to the reduced impact of the interlayer interaction on

phonon restoring forces [145]. In the case of the exfoliated GaS, Raman spectrum does not display peaks related to other crystalline species beyond GaS (*e.g.* Ga_2O_3).

The group space (D_{2h}^{16}) of GeSe provides 12 Raman active optical modes: $4A_g$ + $2B_{1g}$ + $4B_{2g}$ + $3B_{3g}$ [146]–[148] The Raman spectra of the bulk and exfoliated GeSe samples display the most intense Raman modes at ~ 152 cm^{-1}, attributing to the out-of-plane mode (B_{3g}^1) and at ~ 176 cm^{-1} and ~ 190 cm^{-1}, which are attributed to the two in-plane modes (A_g^2 and A_g^1, respectively) [146]–[148]. As shown the **Figure 13f**, in the exfoliated material, the A_g^2 peak is slightly blue-shifted with decreasing of layers, while the other two peaks (B_{3g}^1 and A_g^1) approximately keep the same positions.

Generally, Raman analysis can be used as an accurate tool for determining the thickness of the graphene and other 2D crystals [145], [149], [150]. Contrary to the other aforementioned samples (GaSe and GaS) [52], [137], [145], [151], for GeSe, this is not possible because discrepant results have been reported on the reproducibility of thickness-dependent shifts of their peaks due to variation of the interlayer forces [61], [72], [152], [153].

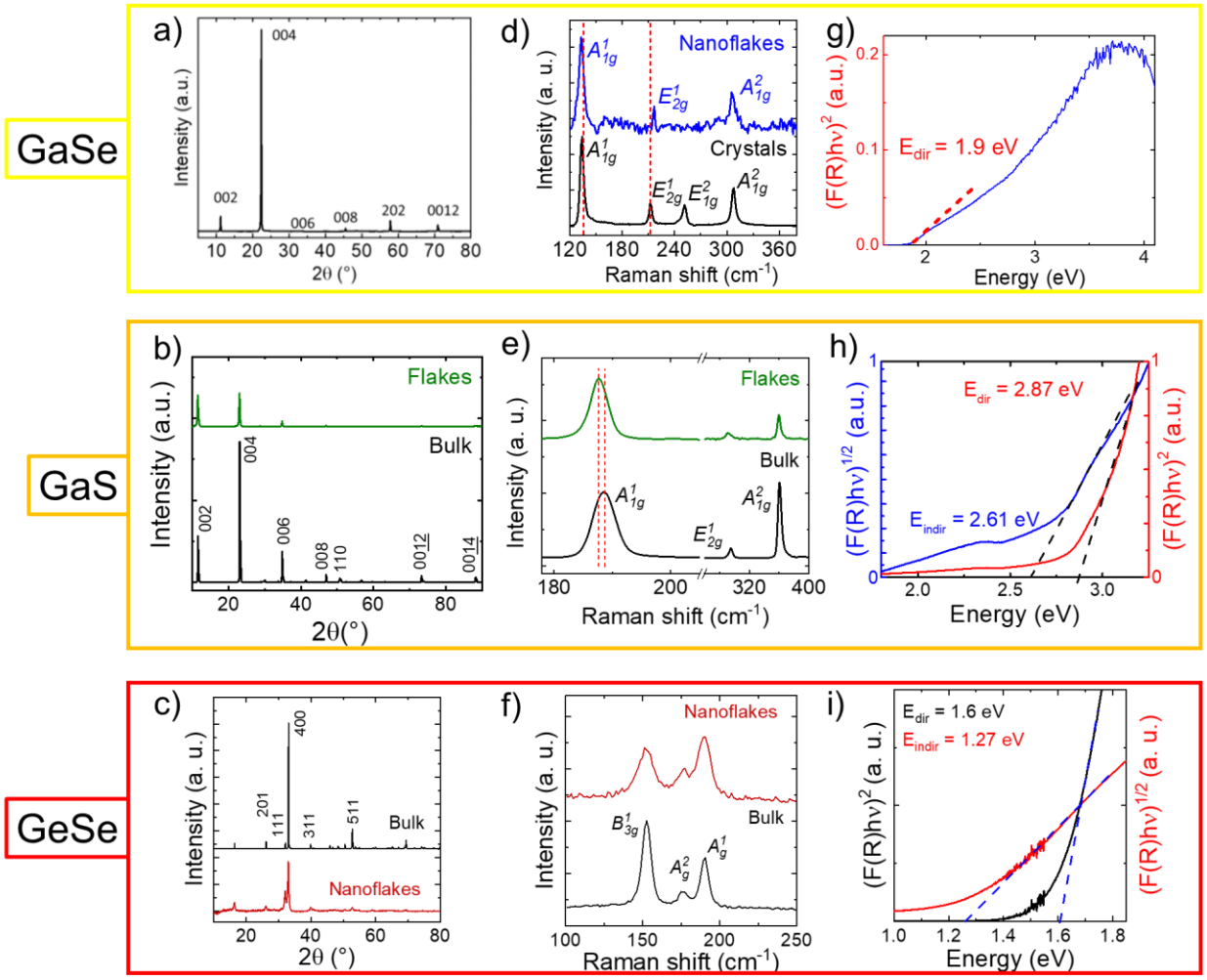

Figure 13: *a*-c) XRD diffractograms and d-f) Raman spectra of GaSe, GaS and GeSe bulk and exfoliated samples. The diffraction and The Raman modes assigned to GaSe, GaS and GeSe structures are shown g-i) $(F(R)h\nu)^n$ *vs* $h\nu$ (Tauc plots) for the GaSe, GaS and GeSe nanoflakes for both direct (n = 2) and indirect interband transitions (n = 0.5) [127], [128], [129].

The E_g values of the MMCs flakes were determined through diffusive reflectance spectroscopy (DRS) measurements using the Kubelka-Munk theory of reflectance (*R*) phenomenon [154], [155]. More in detail, the E_g is estimated by fitting the linear part of $(F(R)h\nu)^n$ *vs* $h\nu$ (Tauc plots of GaSe, GaS, and GeSe, shown in **Figure 13g-i**, respectively), where $(F(R)h\nu)^n = Y(h\nu - E_g)$ is the Tauc relation, in which $F(R)$ is the Kubelka –Munk function, defined as $F(R) = (1-R)^2/2R$, h is Planck's constant, ν is the photon's frequency, and Y is a proportionality constant [154], [155]. The nature

of the electronic transitions is indicated by the exponent, distinguishing between direct (n = 2) and indirect (n = 0.5) interband transitions. Due to the pseudodirect gap behaviour of GaSe, **Figure 13g** shows only the estimated direct E_g of the GaSe (E_g = 1.9 eV), while **Figure 13h** and **13i** report the Tauc plots of the GaS and GeSe flakes film, respectively, for both n = 2 and n = 0.5, from which has been estimated a direct E_g of ~ 2.9 eV and an indirect E_g of ~ 2.6 eV for GaS, while for GeSe the direct E_g value is ~ 1.6 eV and the indirect E_g is ~ 1.27 eV, respectively.

Chapter 4

Metal Monochalcogenides for PEC Water Splitting

In this chapter, metal monochalcogenides, a new class of theoretically predicted photo(electro)catalysts for water splitting reactions, are characterized through photoelectrochemical (PEC) techniques, providing new insight into their feasible application in real PEC-type water electrolyzers. First, the basic principles of PEC water splitting are introduced. Then, the main Figure of Merits (FoM) of photoelectrochemical cells are described in order to provide a subsequent evaluation of the PEC properties of two representative MMCs, namely GaSe and GeSe, in various aqueous media, showing acidic, neutral or alkaline pH.

4.1 Fundamentals of Photoelectrochemical (PEC) Water Splitting

Photocatalytic water splitting in a PEC cell was demonstrated for the first time in 1972 by Fujishima and Honda, using a semiconducting material, namely TiO_2, as a photoanode [156]. Later on, several PEC cells based on semiconductor liquid junctions have been rationalized and designed, opening the way toward an extensive and ever-growing research area [157]–[159]. Generally, a PEC system consists of a photoelectrode (anode or cathode) or two photoelectrodes (tandem system) and a counter electrode immersed in an aqueous electrolyte, and the PEC water splitting reaction is based on the photovoltaic effect in semiconductor materials drived by light [160]–[162]. When light (photons) irradiates on a photoelectrode, holes and electrons are produced in the valence band (VB) and conduction band (CB), respectively. Photoexcited carriers are transferred to surface active sites, and while the excited electrons participate in the hydrogen evolution reaction (HER) to obtain H_2, the excited holes take part in the oxidation evolution reaction (OER) to generate O_2 [47], [163], as shown in **Figure 14**.

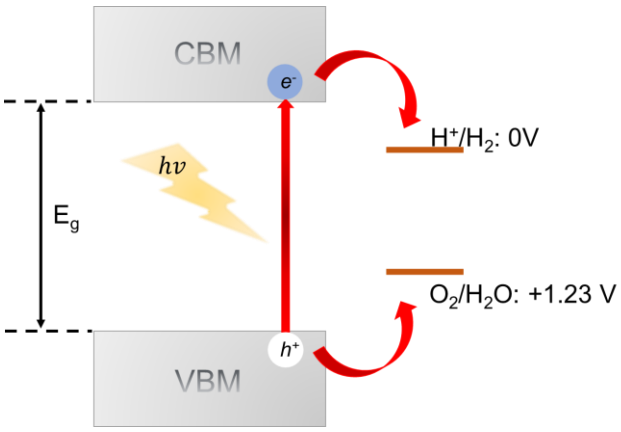

Figure 14: Schematics mechanism involved in PEC water splitting.

The redox potentials are described by two half-reactions, which are expressed when the pH of the electrolyte is zero (pH = 0) by the following reactions:

$$4H^+ + 4e^- \rightarrow 2H_2 \qquad E^0_{red} = 0\ V\ vs\ NHE$$

$$2H_2O \rightarrow O_2 + 4H^+ + 4e^- \qquad E^0_{ox} = +1.23\ V\ vs\ NHE$$

where *NHE* is the normal hydrogen electrode. According to the Nernst equation, the water reduction and oxidation potentials depend on the pH of the solution, shifting the water's redox energy levels by 0.059 per unit pH [47], [164], [165].

According to the half water splitting reactions, the overall water splitting reaction can be expressed as:

$$2h\nu + H_2O_{(liq)} \rightarrow \frac{1}{2}O_{2(gas)} + H_{2(gas)} \qquad E_{overall\ reaction} = +1.23\ V$$

The HER and OER reactions are discussed in more detail below.

- *Hydrogen evolution reaction (HER)*

Hydrogen evolution reaction involves more steps. In the first step (Volmer reaction) the hydrogen is electrochemically adsorbed on the catalyst surface, which is necessary for HER. In acidic condition, the Volmer step proceeds by an initial discharge of the hydronium ion (H_3O^+), while in alkaline media, this step proceeds by the discharge of H_2O, forming H_{ads}. The subsequent step is either electrochemical desorption (Heyrovsky step), or the chemical recombination (Tafel recombination step). The hydrogen evolution reaction pathways in both acidic and alkaline solutions are summarized here below.

In acidic conditions:

$$H_3O^+ + e^- \rightleftharpoons H_{ads} + H_2O \qquad \text{Volmer step}$$

$$H_{ads} + H_3O^+ + e^- \rightleftharpoons H_2 + H_2O \qquad \text{Heyrovsky step}$$

or

$$2H_{ads} \rightleftharpoons H_2 \qquad \text{Tafel step}$$

In alkaline conditions:

$$H_2O + e^- \rightleftharpoons H_{ads} + OH^- \qquad \text{Volmer step}$$

$$H_2O + H_{ads} + e^- \rightleftharpoons H_2 + OH^- \qquad \text{Heyrovsky step}$$

or

$$2H_{ads} \rightleftharpoons H_2 \qquad \text{Tafel step}$$

Practically, the optimal balance between adsorption and desorption steps leads to an efficient HER, as described by the empirical Sabatier principle exemplified by the so-called Volcano plot (*i.e.*, exchange current density (j_0) as a function of hydrogen adsorption free energy (ΔG_{H^+})) [166]. Briefly, a candidate HER-catalyst must have a ΔG_{H^+} close to zero ((ΔG_{H^+}) = 0) [166], to have an optimal binding of the hydrogen atom to the electrode surface. In fact, if this bond is too strong, the reaction−desorption step will limit the overall reaction rate, while if it is too weak, the adsorption step will limit the reaction rate [167]. As shown in the volcano plot in **Figure 15**, platinum is a good electrocatalyst for HER, but due to its high cost and low availability, large-scale use is not possible. For this reason, in the last few years, several 2D semiconductors have been studied as HER electrocatalysts [158].

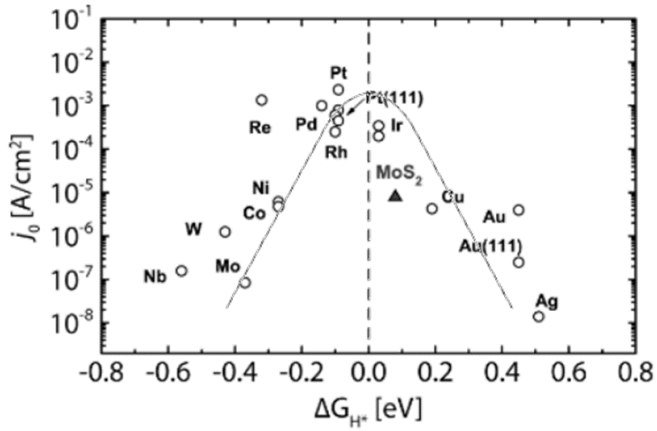

Figure 15: Volcano plot, *i.e.*, exchange current density as a function of hydrogen adsorption free energy for several materials. Adapt from [167].

- *Oxygen evolution reaction (OER)*

The second important reaction in the water splitting process is the OER. This reaction includes several proton/electron couples processes to generate molecular O_2 [165], [168]. Below the reactions involved in the OER process are report for both acidic and alkaline media.

In acidic solutions:

$$2H_2O \rightleftharpoons 4H^+ + O_2 + 4e^-$$

In alkaline solutions:

$$4OH^- \rightleftharpoons 2H_2O + O_2 + 4e^-$$

In acidic media, the O_2 is obtained by oxidation and splitting of two H_2O molecules. Differently, in alkaline media, the OER reaction proceeds by an initial hydroxyl groups OH^-, forming H_2O and O_2 molecules [165]. The best electrocatalysts for OER are RuO_2 and IrO_2 [169]–[171], enabling for water splitting electrolysers showing overpotential of ~1.5 V at current density higher than 10 mA cm^{-2} [172], [173].

Thermodynamically, the production of H_2 and O_2 through water splitting reaction is an endothermic process, with a positive change of the Gibbs free energy, given by

$$\Delta G^0 = -n\,F\Delta E^0 = +237\ KJ\ mol^{-1}$$

where F is the Faraday's constant ($F = 96485\ C\ mol^{-1}$), n is the number of transferred electrons (in this case, $n = 2$), and ΔE^0 is the standard potential of the electrochemical cell ($\Delta E^0 = 1.23\ V$). Indeed, the minimum energy needed to drive the HER and OER is 1.23 eV, as anticipated in the above equations.

Therefore, as a necessary condition, the ideal photocatalyst materials for an efficient water splitting process should possess suitable band gap energy (*e.g.*, the E_g of the semiconductors must exceed the free energy of water splitting of 1.23 eV), and good band positions (*i.e*, conduction band minimum (CBM) energy (E_{CBM}) of semiconductor higher than the reduction potential of H^+/H_2 ($E_{CBM} > E(H^+/H_2)$) and t valence band maximum (VBM) energy (E_{VBM}) of semiconductor lower than the reduction potential of O_2/H_2O ($E_{VBM} > E(O_2/H_2O)$)) [47], [127], [128].

During water splitting process, there are thermodynamic energy losses due to several factors, such as the recombination of the photogenerated charge carriers in bulk or at the surface or the relatively slow rate of the reactions, and an overpotential is required the reaction to occur on its surface [164].

For these reasons, materials with a band gap energy between 1.6 eV and 3.2 eV are typically required to attain the whole water splitting reaction [164]. **Figure 16** reports a comparison between water redox potentials and the band positions of some semiconductors. In addition, a good photocatalyst should also have strong light absorption, high chemical stability, efficient charge transport, low cost, and high earth-abundance [164], [165].

In this context, 2D materials emerged as potential photocatalysts for water splitting reactions, in which their electronic structure can be tuned by controlling the number of layers in order to fulfil the fundamental requirements for HER and OER reactions.

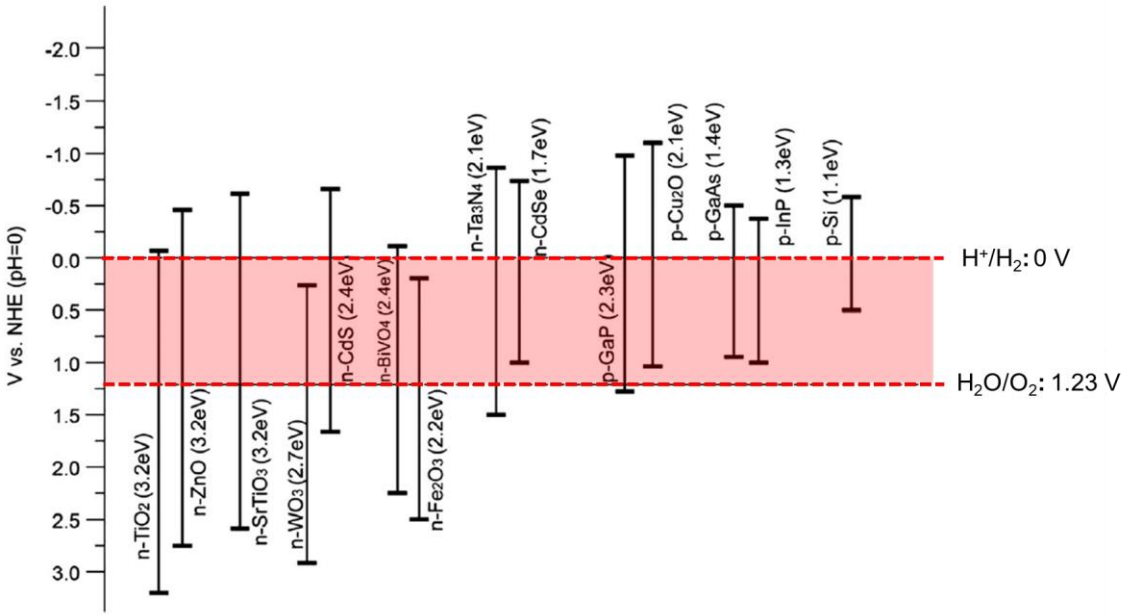

Figure 16: Band gap positions (band gap values expressed in eV) of several semiconductor materials with respect to the reduction and oxidation potentials of water splitting at pH = 0 [164].

Furthermore, in 2D materials, the recombination process is intrinsically mitigated, since the distance between the photogenerated charges and the surface is virtually reduced to zero, suppressing the electron-hole recombination losses [47].

4.2 Photoelectrochemical cell

Figure 17 shows two PEC cells using a photoanode (**Figure 17a**) and photocathode (**Figure 17b**), respectively. As mentioned before, the main components of a PEC cell are the photoelectrode (anode or cathode), a counter electrode, and the electrolyte.

When a semiconductor electrode is immersed in an electrolyte solution, electron transfer occurs at the semiconductor/electrolyte interface so that the electrochemical potential (Fermi level (E_f)) is balanced. More in detail, if E_f is more negative than the electrolyte solution reduction potential, electrolyte solution accepts electrons from a semiconductor, while if E_f is more positive than the electrolyte solution reduction potential, electrolyte solution donates electrons to a semiconductor [161], [164]. As result of the electrochemical potential equilibrium between semiconductor and electrolyte, a band bending within semiconductor takes place, producing a space charge region, inducing an electric field. This electric field plays an important role in the PEC reactions on photoelectrodes, as it drives the separation of the photogenerated charges (electrons and holes) [174].

In a photoelectrode with n-type semiconductors, used as photoanode, as-generated holes, accumulated on the surface of the semiconductors, participate at the oxidation reaction, while the electrons, the majority charge carrier, reach a counter electrode via an external circuit, and are

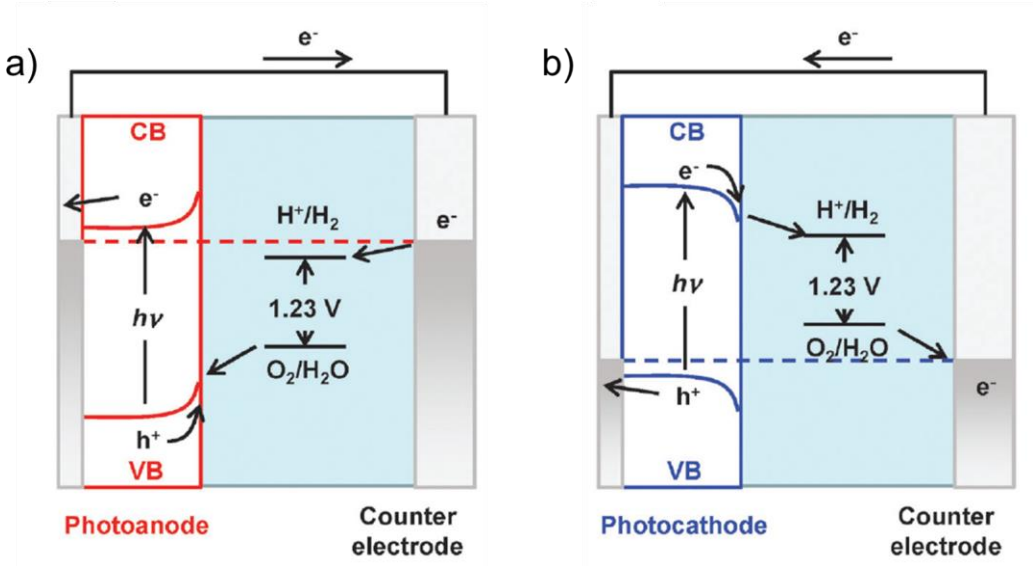

Figure 17: Schematic representation of PEC water splitting system using a) photoanode and b) photocathode. Adapted from [161].

consumed in reduction reaction, as shown the **Figure 17a**. An inverse behaviour occurs with a p-type semiconductor, used as photocathode, in which the minority charge carrier are electrons and work for the production of hydrogen, as shown in **Figure 17b**.

4.2.1 Efficiency and figures of merit (FoM)

The overall thermodynamic efficiency of water splitting is the most important indicator of a PEC water splitting cell [157], [175]. The standard solar-to-hydrogen conversion efficiency (η_{STH}) is defined as the ratio between the chemical energy produced and the solar energy input measured under broadband solar Air Mass 1.5 Global (AM 1.5 G, irradiance = 1000 W m^{-2}) illumination without the applied voltage between the working electrode (WE) and counter electrode (CE), as shown in the following equation [157], [175]

$$\eta_{STH} = \left[\frac{J_{sc} \times 1.23 \times \eta_F)}{P}\right]_{AM\ 1.5G}$$

where J_{sc} is the short-circuit photocurrent density (mA cm^{-2}), η_F is the faradaic efficiency for hydrogen evolution, and P is the incident light power density (mW cm^{-2}).

The efficiency and performance of the PEC electrolyzer can be influence by different factors: efficiencies of light absorption, charge separation, charge transport, and charge collection/reaction efficiency [176].

Although the efficiency is the key Figures of Merit (FoM) for electrochemical solar energy-conversion systems, other FoM are typically used to characterize the photoelectrochemical performances of a single photoelectrode by means of three-electrode configuration measurements. Such FoM are the applied bias photon-to-current metric (Φ_{ABPE}), the onset potential (V_{OP}), the cathodic photocurrent density at 0 V *vs.* RHE ($J_{0\ \mathrm{V}\ vs.\ \mathrm{RHE}}$); the anodic photocurrent density at 1.23 V *vs.* RHE ($J_{1.23\ \mathrm{V}\ vs.\ \mathrm{RHE}}$), the ratiometric power-saved metric for HER ($\Phi_{\mathrm{saved,HER}}$) and the ratiometric power-saved metric for OER ($\Phi_{\mathrm{saved,OER}}$), and the external quantum efficiency (EQE) [157], [162], [175], [177]–[179].

The applied bias photon-to-current metric (Φ_{ABPE}) to evaluate the PEC performance of the photoelectrode can be calculated as [162], [175], [177]–[180]

$$\Phi_{ABPE} = \frac{J_{ph}(1.23 - |E_{app} - E_{ocp}|)}{P}$$

where J_{ph} is the photocurrent density (mA cm^{-2}), E_{app} is the applied potential to electrode, E_{ocp} is the open circuit at which J_{ph} was measured, and P is the incident light power density (mW cm^{-2}).

The onset potential (V_{OP}) is defined as the potential at which the photocurrent related to the HER (hydrogen evolution reaction) or OER (oxygen evolution reaction) is observed.

While the ratiometric power-saved metrics are calculated by [157], [162], [175], [177]–[179]

$$\Phi_{saved} = \frac{\eta_F \times |j_{ph,m}| \times [E_{light}(j_{ph,m}) - E_{dark}(j_{ph,m})]}{P} = \frac{\eta_F \times |j_{ph,m}| \times V_{ph,m}}{P}$$

where η_F is the current-to-hydrogen (or oxygen) faradaic efficiency assumed to be 100%, P is the power of the incident illumination, and $j_{ph,m}$ and $V_{ph,m}$ are the photocurrent and photovoltage at the maximum power point, respectively. The j_{ph} is the difference between the current under illumination of a photocathode and the current of the corresponding catalyst. The photovoltage V_{ph} is the difference between the potential applied to the photocathode under illumination (E_{light}) and the potential applied to the catalyst electrode (E_{dark}) to obtain the same current density. The subscript "m" stands for "maximum".

While, the efficiency of a PEC device can be calculated from its EQE, which is also named incident photon-current conversion efficiency (IPCE) [180]. More in detail, the EQE is defined as the ratio between the number of carriers collected by a device (*e.g.*, solar cell or photodetector) and the number of photons with a given wavelength impinging the device, and it is given by following equation [181]

$$EQE\ (\lambda) = \frac{1}{q}\frac{hc}{\lambda}\frac{I_{PH}}{P_{light}} = 1240\frac{R}{\lambda}$$

where q is the electronic charge, h is Planck's constant, and c is the speed of light, I_{PH} is the generated photocurrent density (A m^{-2}), λ is the incident light wavelength (nm), P_{light} is the photon flux (W m^{-2}), and R is the responsivity (A W^{-1}).

4.3 Photoelectrodes fabrication

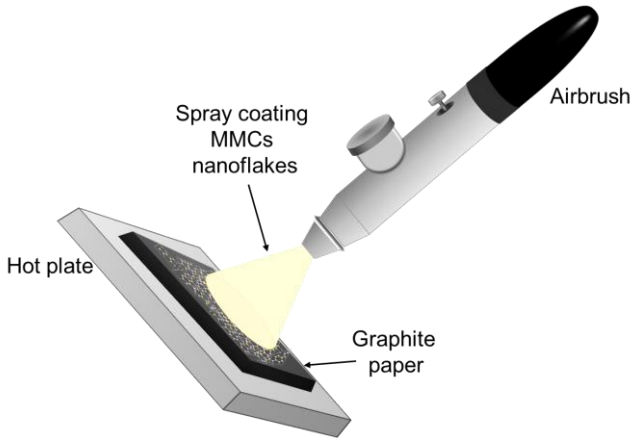

Figure 18: Schematic illustration of the production of MMCs photoelectrodes by spray coating. The MMCs flakes were deposited onto graphite paper.

The MMCs dispersions, produced via LPE in IPA, were deposited onto graphite paper by spray coating (mass loading of MMCs flakes = 0.1 mg cm^{-2}) for the photoelectrodes fabrication, as shown the **Figure 18**. Graphite paper was used as the substrate because it acts as an inert current collector as well as being a cheap and flexible substrate [182]. At the same time, the spray coating technique has a great potential for large-scale production and is used for fast deposition of dispersions on both rigid and flexible substrates. In fact, it is suitable for different substrate shapes, dimensions, and morphologies [183]. This technique consists in forcing printing dispersion through a nozzle which forms a fine aerosol. An important parameter to obtain a uniform coating is the distance between the nozzle and the substrate, in fact, short distances form thick and irregular films because of solvent accumulation on the surface, while too long distances will result in large material wastes [183].

The substrate was placed on a heated plate in order to favour rapid evaporation of the solvent.

The temperature to which the substrate is exposed depends on the solvent used, and, in our cases, it was 60 °C.

Figure 19a shows a representative photograph of as-produced MMCs photoelectrodes, which was manually bent to evidence its mechanical flexibility. As shown by SEM imaging (**Figure 19b**), the photoelectrodes present a laminar structure, in which MMCs flakes preferentially orient

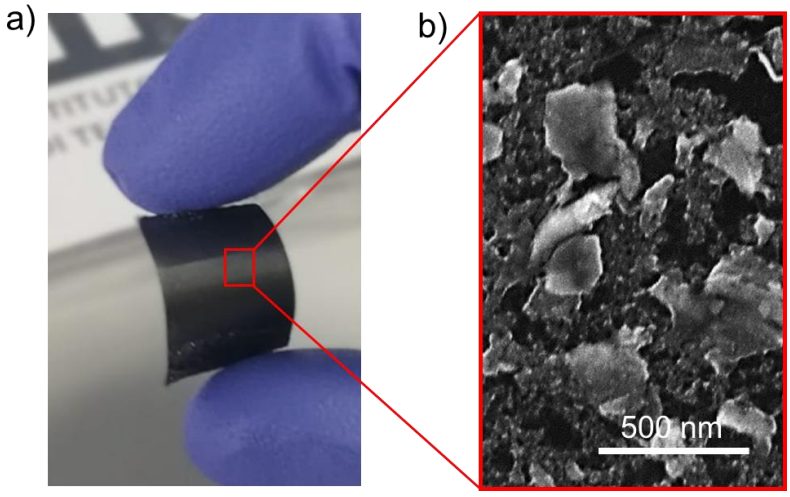

Figure 19: a) Photograph of a MMCs photoelectrodes, and b) its corresponding SEM image. Adapted from [127].

horizontally to the substrate plane.

4.4 Photoelectrochemical measurements of MMCs and results

In this work, the electrochemical measurements on the photoelectrodes were carried out in a flat-bottom fused silica cell using a three-electrode cell of the potentiostat/galvanostat station (VMP3, Biologic), controlled *via* own software.

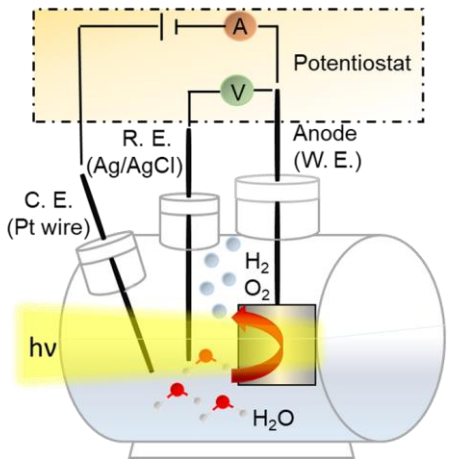

Figure 20: Schematic diagram of experimental setup for electrochemical measurements**.** Adapted from [127].

Figure 20 shows the schematic illustration of the PEC cell used for the characterization of our materials, forming the WE. In particular, a Pt wire was used as the CE, while saturated KCl Ag/AgCl is used as the reference electrode (RE). Measurements were performed in 200 mL of 0.5 M H_2SO_4 (99.999% purity, Sigma Aldrich), or 1 M KCl (99.999% purity, Sigma Aldrich), or 1 M KOH (99.999% purity, Sigma Aldrich) at room temperature. The pH of the electrolytic solutions was measured with Oakton ION 700 ISE/pH Meter. Before each measurement, the solution was degassed to remove the dissolved O_2 from electrolyte by flowing N_2 gas, and afterwards, during the experiments, a constant N_2 flow was maintained to avoid re-dissolution of molecular O_2 in the electrolyte. The applied potential between the WE and RE can be converted to the reversible hydrogen electrode (RHE) according to the Nernst equation:

$$E_{RHE} = E_{ref} + E^0_{ref} + 0.059pH$$

where E_{RHE} is the potential of the WE against the electrolyte solution with respect to the RHE, E_{ref} is the potential of the WE measured with respect to a RE, and E^0_{ref} is the potential of the RE with respect to the normal hydrogen electrode (NHE) [161]. Linear Sweep Voltammetry (LSV)

measurements were performed to evaluate the response of photoelectrodes both under dark and simulated sunlight. A 300 W Xenon light source LS0306 (Lot Quantum Design), equipped with AM1.5G filters, was used to 1 Sun.

4.4.1 Gallium Selenide

The PEC water splitting activity of the GaSe-based photoelectrodes was evaluated in both acidic and alkaline electrolytes. The cathodic and anodic linear sweep voltammetry (LSV) scans are displayed in **Figure 21a** and **Figure 21b**, respectively. The measurements were performed in both anodic and cathodic directions under chopped simulated 1 sun illumination, and the LSV curves were acquired at 5 mV s^{-1} scan rate.

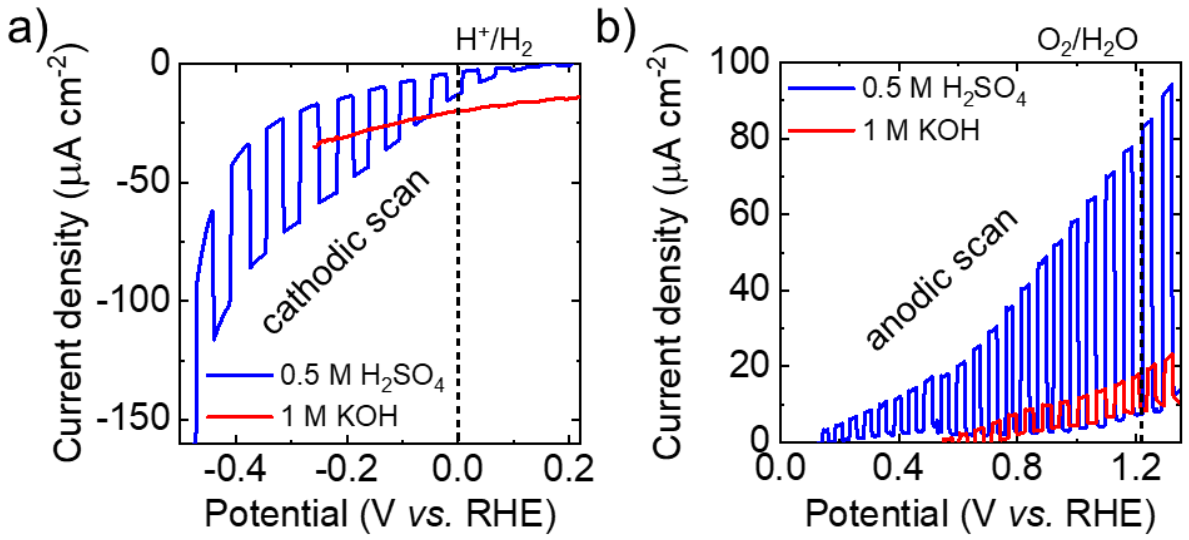

Figure 21: LSV scans measured for GaSe photoelectrodes for a) HER and b) OER under chopped simulated sunlight (AM 1.5 G illumination) in 0.5 M H_2SO_4 and 1 M KOH. The black dashed lines indicate the redox potential for H^+/H_2 and O_2/H_2O at 0 V *vs* RHE and +1.23 V *vs* RHE, respectively [127].

In 0.5 M H_2SO_4, the photoelectrodes show a positive onset potential (V_{OP}) of + 0.14 V *vs.* RHE, which is defined as the potential at which the photocurrent related to the HER (hydrogen evolution reaction) or OER (oxygen evolution reaction) is observed. In order to evaluate the performance of

photoelectrodes the cathodic and anodic photocurrent density at 0 V *vs.* RHE ($J_{0\ V\ vs.\ RHE}$) and at 1.23 V *vs.* RHE ($J_{1.23\ V\ vs.\ RHE}$), respectively, were measured. The estimated value of the $J_{0\ V\ vs.\ RHE}$ is – 9.3 μA cm^{-2} for HER, while $J_{1.23\ V\ vs.\ RHE}$ is + 83.4 μA cm^{-2} for OER. The calculated ratiometric power-saved values (Φ_{saved}) for HER and OER are $\Phi_{saved,HER}$ = 0.09% and $\Phi_{saved,HER}$ = 0.25%, respectively.

In 1 M KOM, the photoelectrodes show a clear photoanodic behaviour, while the cathodic LSV scans show a significant negative dark current density (< − 10 μA cm^{-2} for applied potential < + 0.2 V vs RHE). The negligible anodic current density is due to the formation of oxidized species promote by the alkaline electrolyte, which can decompose to form soluble products (*e.g.*, GaO_2^-) during cathodic LSV scans [184], [185].

Figure 22 reports the absolute photocurrent density of the photoelectrodes (defined as the

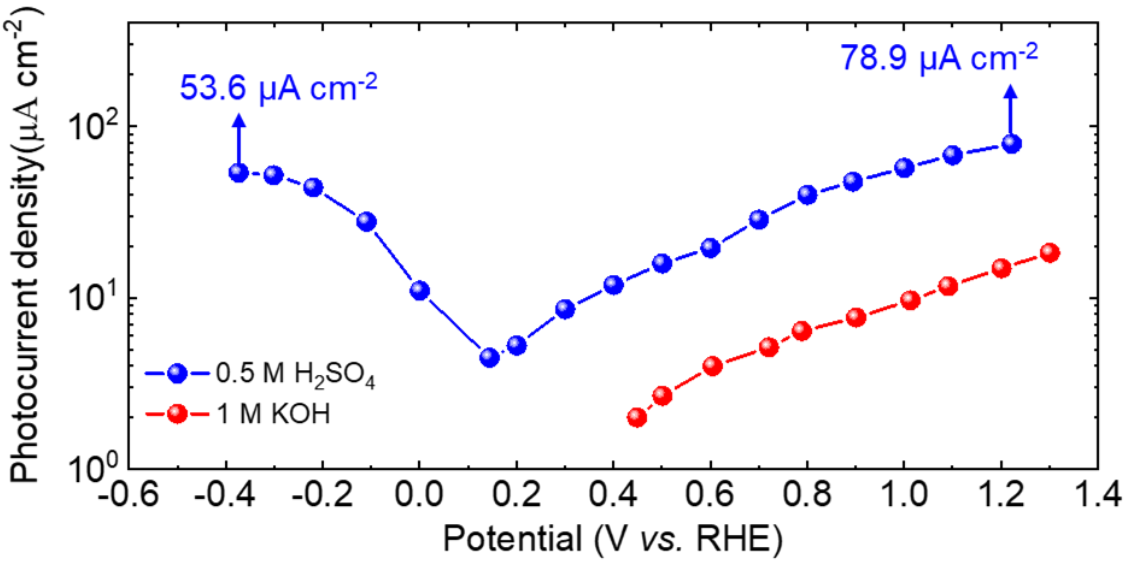

Figure 22: Absolute photocurrent density of the photoelectrodes as a function of the applied potential measured in 0.5 M H_2SO_4 and 1 M KOH [127].

difference between current under illumination and in the dark) as a function of the applied potential, showing maximum values of the photocurrent density in 0.5 M H_2SO_4. However, the

PEC performance can be improved by engineering the photocathodes architecture and optimizing the electrolyte solution.

4.4.2 Germanium Selenide

The photo(electro)catalytic properties of GeSe nanoflakes, produced by LPE, were evaluated as either photocathodes and photoanodes for water splitting reactions under chopped simulated AM 1.5 G illumination in aqueous solutions with different pH (*i.e.*: 0.5 M H_2SO_4, pH 0.3; 1 M KCl, pH 6.5; 1 M KOH, pH 14).

The best results were found in 0.5 M H_2SO_4 and 1 M KCl, in which the cathodic (negative) photocurrent density at 0 V *vs.* RHE ($J_{0\ V\ vs.\ RHE}$) is of – 10.9 μA cm^{-2} with an onset potential V_{OP} = + 0.30 V (see **Figure 23a**), and the anodic (positive) photocurrent density at 1.23 V *vs.* RHE ($J_{1.23\ V\ vs.\ RHE}$) is of + 31.0 μA cm^{-2} with an V_{OP} of + 0.48 V (see **Figure 23b**), respectively. These

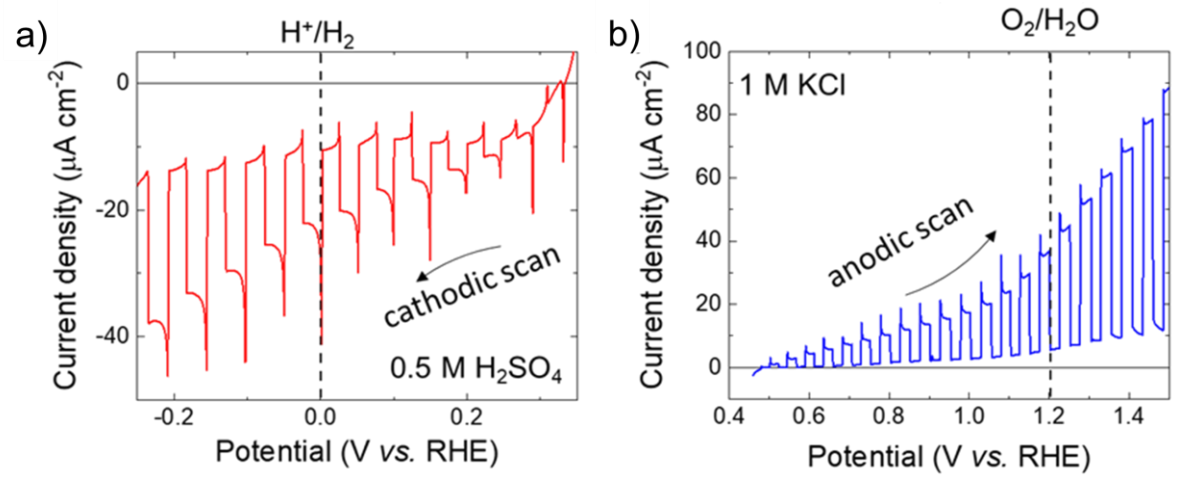

Figure 23: a) cathodic LSV curve in 0.5 M H_2SO_4, and b) cathodic LSV curve in 1 M KOH. The measurements were performed under chopped simulated sunlight (*i.e.*, AM 1.5 G illumination) [128].

results evidence that the GeSe flakes are promising materials to be used in water photoelectrolysis cells, as previously observed for GaSe flakes.

Whereas, when the GeSe-based photoelectrodes were tested in 1M KOH solution (pH 14), the data indicate that the graphite papers (the current collector used for GeSe photoelectrodes) exhibit significant dark current during both cathodic and anodic operations, as shown in **Figure 24a,b** respectively, making hard the reliable analysis of the photoresponse of GeSe nanoflakes.

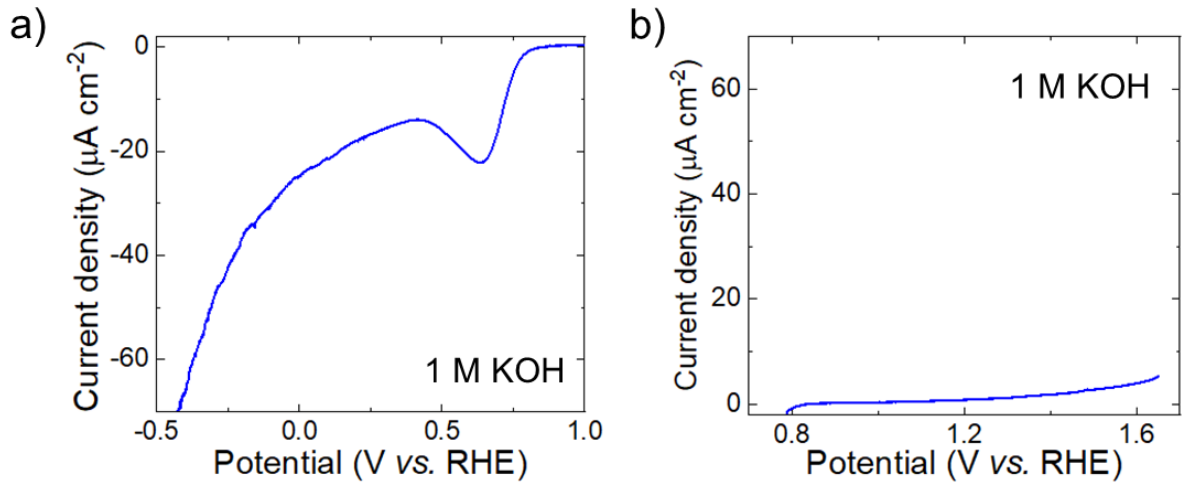

Figure 24: LSV curves measured for GeSe photoelectrodes for a) the HER (cathodic scan) and b) the OER (anodic scan) in 1 M KOH under chopped simulated sunlight [128].

Chapter 5

MMCs for PEC-type Photodetectors

In this chapter, the MMCs nanoflakes were exploited as solution-processable materials for the realization of PEC-type photodetectors in aqueous electrolytes. More in detail, the PEC characterization of MMCs-based photoelectrodes proves photoanodic and photocathodic responses in aqueous media as a function of the wavelength and the illumination intensity. Consequently, these results directly enable PEC-type photodetectors for UV-visible light to be conceived.

5.1 Self-Powered Photodetectors

Photodetectors are systems that can convert an optical signal into an electrical signal [186]. They play a key role in many fields, including sensing systems for video imaging [187], optical and telecommunication [188], [189], and biomedical devices [190]. Recently, many studies about photodetectors based on 2D materials have been carried out, benefiting from the excellent optoelectrical and structural properties of these materials. In particular, self-powered photodetectors, have attracted significant interest in the context of self-powered photodetectors. The latter can operate without an external power source, resulting more portable and adaptable than conventional photodetectors [186], [191]. In addition, these devices require simple and low-cost fabrication processes [192]. Depending on their configuration, self-powered photodetectors can be classified into three types: p–n junction photodetectors, Schottky junction photodetectors, and photoelectrochemical-type (PEC-type) photodetectors [186], [193]. The photovoltaic effect of semiconductors originates the photoresponse of self-powered photodetectors [186], [193]. Briefly, electron-hole pairs are produced under illumination conditions, and their subsequent separation,

as well as the directional movement of photogenerated electrons, generate a photocurrent [186], [193]. The difference between a PEC-type photodetector and the p-n and Schottky junctions is that the latter promotes separation of the photogenerated electron-hole pairs from the built-in electric field [186]. On the other hand, PEC-type photodetectors promote the separation of the photogenerated electron-hole pairs due to the energy barrier between the electrode materials and the electrolyte and completes the current loop by exchanging electrons with the electrolyte [186].

The most important FoM to evaluate the performance of the photodetector is the responsivity (R), which is the ratio of photocurrent density to irradiated light power density.

5.1 Results

The photoelectrodes, produced by spray coating of the MMCs nanoflakes dispersion onto graphite paper (see the previous Chapter), were exploited as PEC-type photodetectors in a three-electrode system at different illumination wavelengths (275, 455, 505, and 625 nm) in aqueous electrolytes. The illumination wavelengths used for different materials correspond to energies above their E_g, *i.e.*, 1.9, 2.9, and 1.27 eV for GaSe, GaS and GeSe, respectively. The light-emitting diodes (LEDs) M275 (Thorlabs), M455L3 (Thorlabs), M505L3 (Thorlabs), and M625L3 (Thorlabs) were used as monochromatic source for wavelengths (λ) of 275 nm, 455 nm, 505 nm, and 625 nm, respectively. The light intensity of the LEDs was adjusted through source meter (2612B Dual-Channel System SourceMeter, Keithley)-controlled LED driver (LEDD1B, Thorlabs). The illumination intensity of the LED was calibrated by means of an optical power and energy meter (PM100D, Thorlabs).

5.1.1 Gallium Selenide

The measurements of GaSe flakes in 0.5 M H_2SO_4 upon three different illuminations with wavelengths in the visible spectral range, *i.e.*, 455, 505, and 625 nm, are reported in **Figure 25a**. The applied potentials were limited between −0.3 V and +0.8 V *versus* RHE to avoid (photo)electrochemical degradation of the photoelectrodes due to high reductive and oxidative conditions. The maximum values of R of the GaSe photodetectors were found under illumination at 455 nm, namely 157 mA W^{-1} at −0.3 V *vs* RHE and 117 mA W^{-1} at +0.8 V *vs* RHE).

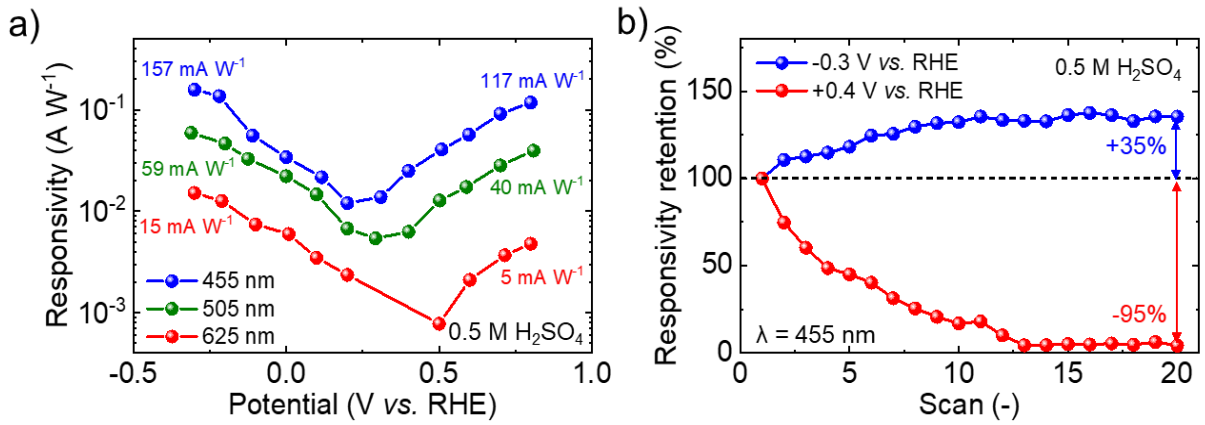

Figure 25: a) Responsivity of PEC-type GaSe photodetectors in 0.5 M H_2SO_4 as a function of the applied potential upon three different illumination wavelengths in the visible spectral range: 455, blue; 505, green; 625 nm, red (light intensity: 63.5 μW cm^{-2}). b) Responsivity retention of the GaSe photodetectors in 0.5 M H_2SO_4 at cathodic and anodic operations at −0.3 V *vs* RHE and +0.4 V *vs* RHE, respectively [127].

Figure 25b shows the photoelectrodes' stability, which was evaluated by measuring the responsivity of the devices during 20 subsequent LSV scans in both cathodic and anodic regime at -0.3 V *vs* RHE and +0.4 V *vs* RHE, respectively. Clearly, GaSe photodetectors exhibited a durable responsivity (+35% after 20 LSV scans) under cathodic operation, while the responsivity progressively degraded during anodic operation (−80% after 20 LSV scans). This degradation is tentatively ascribed to the anodic potential-induced evolution of O_2 (*i.e.*, OER), as well as to progressive oxidation of the GaSe flakes [184]. The same analyses were performed in alkaline

media (1 M KOH). **Figure 26a** and **26b** report the responsivity of GaSe photodetectors and the stability of the PEC responses, respectively, in 1 M KOH. The responsivity values are lower than in the acidic media, and a similar photodetector degradation under anodic potentials was observed in 1 M KOH. In addition, no cathodic photoresponse was observed in alkaline conditions.

Based on these results, the photocurrent density of the GaSe photodetectors at a fixed potential of

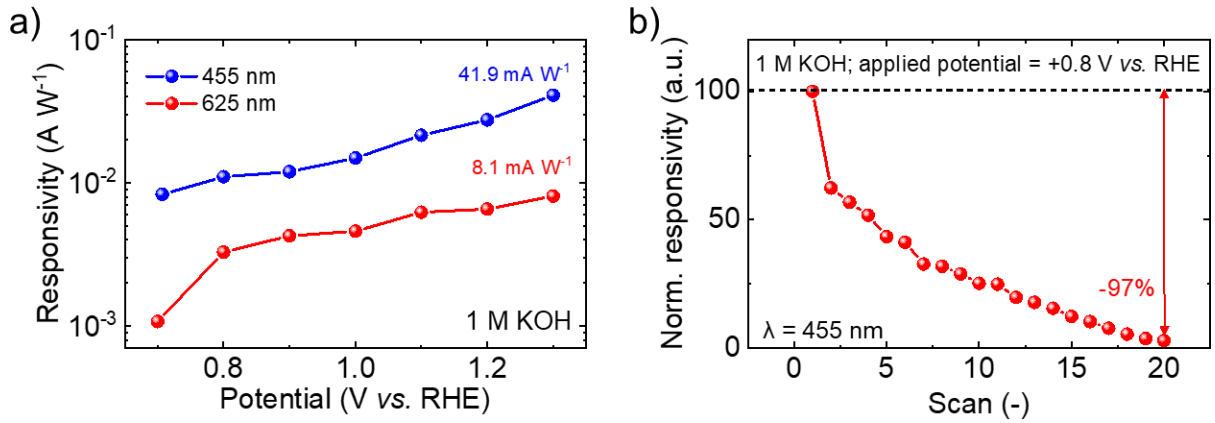

Figure 26: a) Responsivity of PEC-type GaSe photodetectors in 1 M KOH as a function of the applied potential upon two different illumination wavelengths in the visible spectral range: 455 and 625 nm **(**light intensity: 63.5 μW cm^{-2}**)**. b) Responsivity retention of the GaSe photodetectors in 1 M KOH applied potential of +0.8 V *vs* RHE [127].

-0.3 V *versus* RHE as a function of the light intensity was evaluated in 0.5 M H_2SO_4 (**Figure 27a**). The photocurrent density increases with increasing the light intensity. Typically, the photocurrent density *vs.* light intensity data is fitted with a power law, *i.e.*:

$$\text{photocurrent density} \propto (\text{light intensity})^{\gamma}$$

where γ is a factor determining the response of the photocurrent to light intensity. For light intensity ≤ 56.7 μW cm^{-2}, the experimental data can be fitted with a linear fit with γ is 0.97. Considering that γ = 1 indicates negligible charge recombination and trapping processes, it can be concluded that GaSe flakes maximize the surface area available for PEC reactions, canceling out the photocharge recombination processes [118]. As shown in **Figure 27a**, the responsivity (~0.16

A W^{-1}) is retained with increasing the light intensity (up to the tested values of 56.7 μW cm^{-2}). Another important parameter is the response time. **Figure 27b** displays the normalized photocurrent as a function of the time, showing rise time (τ_R) and fall time (τ_F) of 855 and 720 ms, respectively. These values are significantly inferior to solution-processed PEC-type photodetectors (typically in the order of 10 s) [194].

5.1.2 Gallium Sulfide

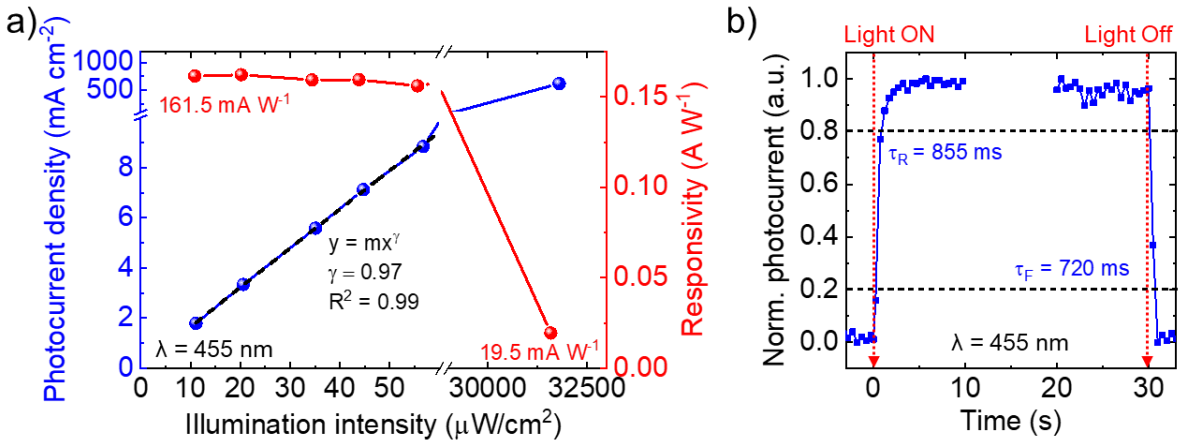

Figure 27: a) Photocurrent density (blue y-axis) and responsivity (red y-axis) of the GaSe photodetectors at −0.3 V *versus* RHE as a function of the light intensity. Dashed black line indicates the curve fitting of the data measured at low-light intensity. b) Normalized photocurrent of the GaSe photodetector at applied potential of −0.3 V versus RHE measured over time after an illumination pulse of 30 s (wavelength = 405 nm, light intensity = 63.5 μW cm^{-2}). The rise and fall time of the photocurrent response are reported [127].

The GaS photodetectors were tested in different aqueous electrolytes in a range from acidic to alkaline (1 M H_2SO_4 (pH 1), 1 M Na_2SO_4 (pH 6), and 1 M KOH (pH 14) under four different illumination wavelengths, namely 275, 455, 505, and 625 nm. Since the measured photoresponses of GaS photodetectors for illumination wavelength of 505 and 625 nm were zero (or below-detection sensitivity), **Figure 28a-c** reports the anodic linear sweep voltammetry (LSV) measurements for the GaS photodetectors under chopped illumination (frequency = 0.33 Hz) at

excitation wavelengths of 275 and 455 nm with an intensity of 1.3 mW cm^{-2}. Moreover, the PEC properties of GaS nanoflakes were also tested under cathodic condition, but the preliminary cathodic LSV measurements did not show any photocathodic response. For this reason, GaS nanoflakes were analyzed only as photoanodes. The responsivities of the GaS photoanodes as a function of the applied potential in the three media and as a function of the wavelength were reported in **Figure 28d** and **Figure 28e**, respectively. As shown in **Figure 28d**, the highest recorded responsivities are under the 275 nm illumination with an intensity of 1.3 mW cm^{-2} (1.8

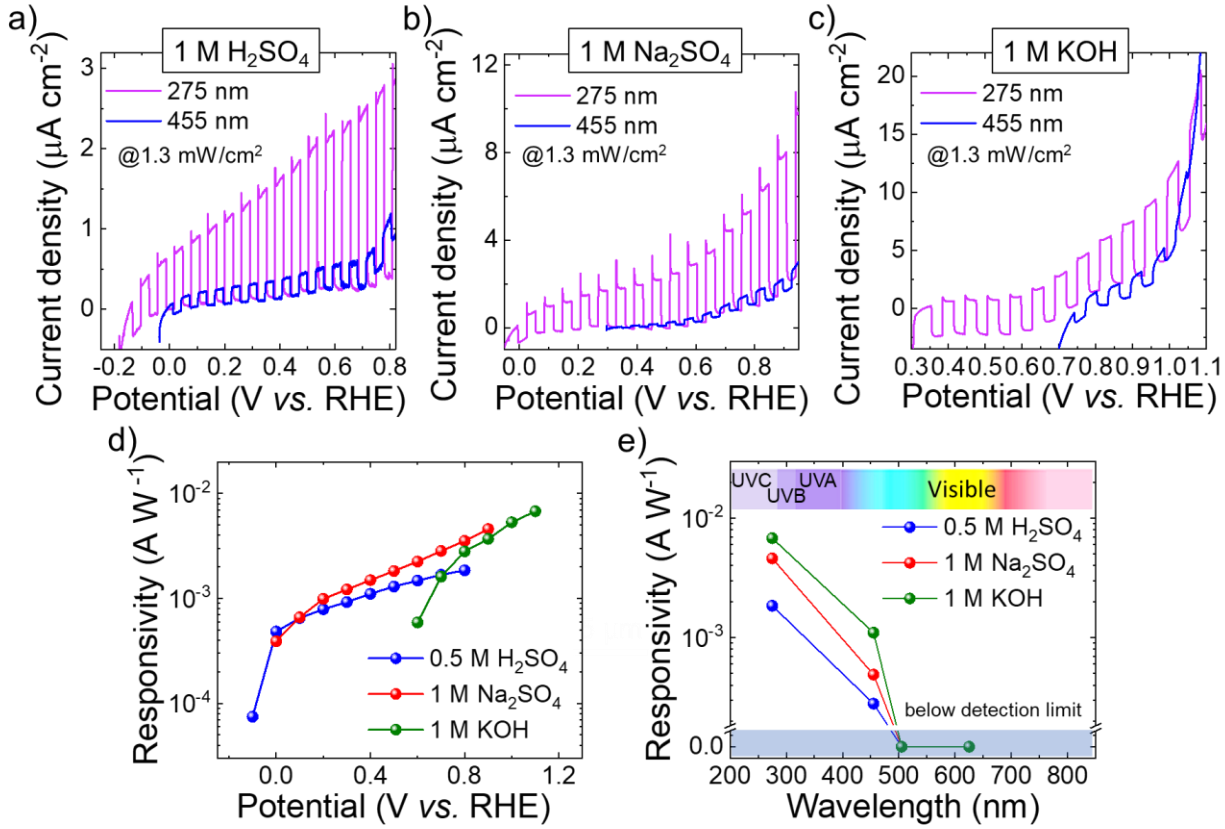

Figure 28: LSV scans measured for GaS PEC-type photodetectors under UV (275 nm) and blue (455 nm) illumination with intensity of 1.3 mW cm^{-2} in a) 0.5 M H_2SO_4, b)1 M Na_2SO_4 and c) 1M KOH. d) Responsivity of PEC-type GaS photodetectors in 0.5 M H_2SO_4, 1 M Na_2SO_4 and 1M KOH as a function of the applied potential under 275 nm illumination with intensity of 1.3 mW cm^{-2}. e) Wavelength dependence of the device responsivity under the same illumination intensity of 1.3 mW cm^{-2} in all investigated aqueous media [129].

mA W^{-1} for 1 M H_2SO_4 at 0.8 V *vs.* RHE, 4.6 mA W^{-1} for 1 M Na_2SO_4 at 0.9 V *vs.* RHE, and 6.8 mA W^{-1} for 1 M KOH at 1.1. V *vs.* RHE). **Figure 28e** indicates that the GaS photodetectors show UV-selective light detection, indicating that exfoliated GaS is a promising material for UV-sensitive applications. In addition, the high responsivity to UV light (275 nm) suggests the direct bandgap transition as the main pathway driving the PEC activity of the devices. Meanwhile, the low photoresponse for blue light can be attributed to either indirect bandgap absorption or sub-bandgap states, which can also contribute to the photoresponse to blue light in solid-state photodetectors based on isolated GaS flakes [52].

To evaluate the structural properties of GaS flakes, Raman analyses were performed on the GaS photodetectors after PEC tests. As shown in **Figure 29a**, Raman spectra are similar to the one measured for the as-produced GaS flakes, which means that structural integrity is preserved. Moreover, to evaluate the stability of GaS photodetectors, the responsivity retention of the GaS photoelectrodes as a function of the number of the LSV scans is displayed in **Figure 29b**, in which the devices exhibit the most stable PEC performance in 1 M KOH. In KOH, the responsivity retention after 20 LSV scans is 49.9%.

Probably, this degradation is due to a mechanical delamination of the GaS photoelectrodes induced by progressive gas evolution (*i.e.*, O_2 evolution due to OER), as reported for the GaSe (see previous section and ref. [127]) and GeSe [128]). Prospectively, the engineering of devices through the use of polymeric (*e.g.*, sulfonated tetrafluoroethylene-based fluoropolymer-copolymer - Nafion)

[128], [195] or conductive (*e.g.*, carbon nanotubes) binders [196], [197] could help to stabilize further the performance of the GaS photoelectrodes.

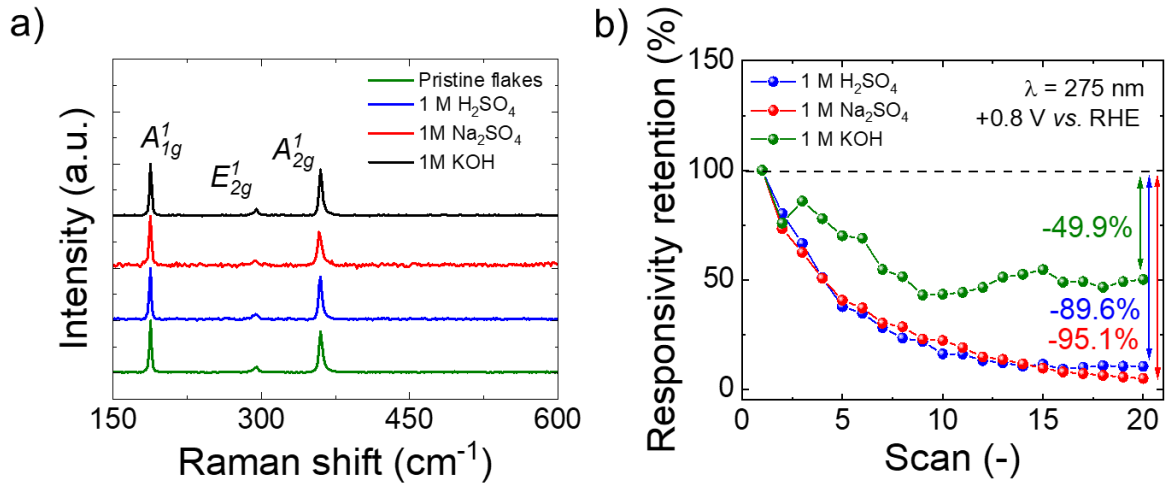

Figure 29: a) Comparison between the Raman spectrum of the pristine GaS flakes and Raman spectra of the GaS photoelectrode after PEC stability tests (20 LSV scans) in all investigated solutions (1 M H_2SO_4, 1 M Na_2SO_4, and 1 M KOH). b) Responsivity retention of the GaS photodetectors in all investigated solutions as a function of the number of the LSV scan at +0.8 V vs RHE [129].

5.1.3 Germanium Selenide

The PEC performance of GeSe nanoflakes were evaluated in a three-electrode system in different aqueous electrolytes: 0.5 M H_2SO_4 (pH 0.3), 1 M KCl (pH 6.5), 1 M KOH (pH 14), investigating the photoresponse for blue, green and red (namely 455, 505, and 625 nm) light (intensity = 63.5 μW cm^{-2}). The responsivities were measured LSV and were reported as a function of the applied potential in **Figure 30a**. The range of the applied potentials was limited within suitable ranges for both cathodic and anodic operations to avoid photoelectrode degradation. In all the investigated media, the photodetectors showed the highest R for illumination wavelength of 455 nm. The R decreases with increasing the illumination wavelength to 455 nm and 625 nm, indicating that the photons with the highest energy (*e.g.*, ~2.7 eV for illumination wavelength = 455 nm) can efficiently excite the exfoliated GeSe. In 0.5 M H_2SO_4, the values of the responsivity are 316.6

and 95.5 mA W^{-1} at −0.5 and +0.8 V *vs* RHE, respectively, and in 1 M KOH, the values are 234.5 and 248.3 mA W^{-1} at −0.1 and +0.9 V *vs* RHE, respectively. For the highest value of R (*i.e.*, 316.6 mA W^{-1} in 0.5 M H_2SO_4), the external quantum efficiency (EQE) was also evaluated. The EQE is calculated as EQE = 100 × (responsivity/λ) × 1240 W nm A^{-1}, in which λ is given in nm and the responsivity in A W^{-1}, obtaining an EQE of 86.3%. This value approaches the theoretical limit of

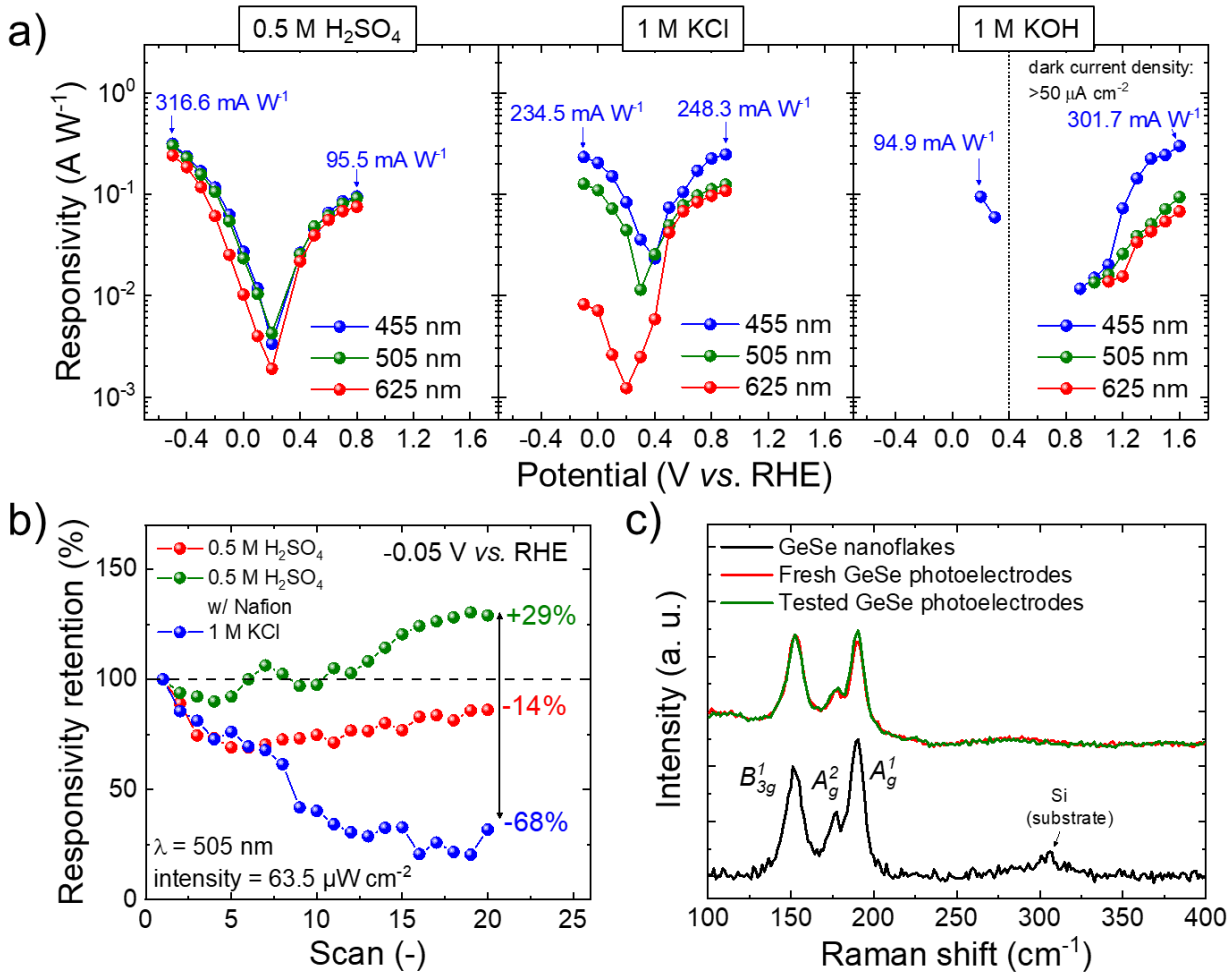

Figure 30: a) Responsivity of PEC-type GeSe photodetectors as a function of the applied potential in the 0.5 M H_2SO_4, 1 M KCl, and 1 M KOH under three different illumination wavelengths in the visible spectral range: 455 nm, 505 nm, and 625 nm. Light intensity: 63.5 μW cm^{-2}. b) Responsivity retention of the GeSe photodetectors at −0.05 V *vs* RHE in 0.5 M H_2SO_4 and 1 M KCl. c) Raman spectra (λ_{exc} = 633 nm) of the GeSe nanoflakes deposited on Si substrate, fresh GeSe photoelectrodes, and tested Ge photoelectrodes [128].

100% of PEC-type photodetectors. The stability of GeSe photodetectors was evaluated in 0.5 M H_2SO_4, and 1 M KCl, exhibiting the most stable responsivity in acidic solution. **Figure 30b** shows the responsivity retention as a function of the LSV scan. In order to improve the electrochemical activity of the photoelectrode, a Nafion film atop the photocatalytic GeSe film was used, contrasting the possible delamination of the GeSe nanoflakes due to the redox reaction [195]. Initially, during the first 10 LSV scans, the photoelectrodes did not display an improvement of the responsivity, but an increase of +29% was observed during the subsequent LSV scans because of the hydration of the Nafion coating. Raman measurements were performed to assess the chemical and structural integrity of the GeSe nanoflakes after the stability test for cathodic operation in 0.5 M H_2SO_4, as shown in **Figure 30c**. The structural properties of GeSe nanoflakes are preserved during cathodic condition.

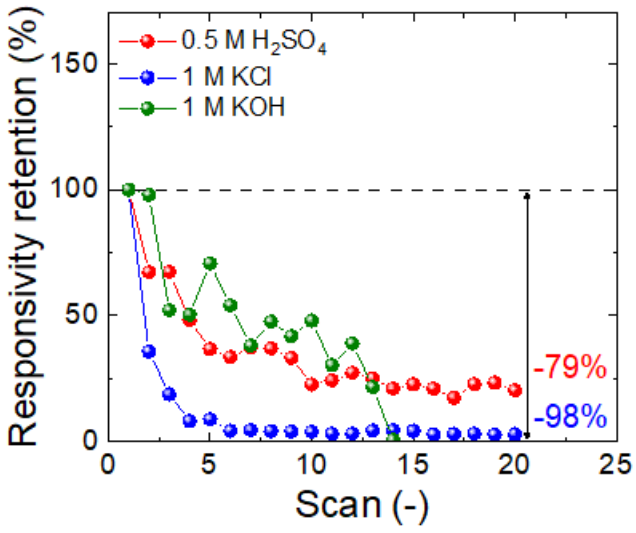

Figure 31: Responsivity retention of the GeSe photodetectors during anodic operation in 0.5 M H_2SO_4 at +0.4 V vs RHE, 1 M KCl at +0.9 V vs RHE, and 1 M KOH at +1.2 V vs RHE [128].

The stability tests of GeSe photodetectors were also performed during anodic operation in the investigated media, *i.e.*, 0. 5 M H_2SO_4, 1 M KCl, and 1 M KOH (**Figure 31**). After 20 LSV scans, R decrease in all the cases, suggesting a degradation of the photoelectrodes under anodic potential due to an oxidation of the GeSe flakes.

Figure 32 shows the photocurrent density *vs.* light intensity (photocurrent density $\propto$ (light intensity)$^{\gamma}$) at 0 V *vs.* RHE in 0.5 M H_2SO_4 (**Figure 32a**) and 1 M KCl (**Figure 32b**), respectively. Form power law fit of the photocurrent density, the values of γ are 0.56 and 0.83 in 0.5 M H_2SO_4 and 1 M KCl, respectively. In the first case, γ indicates significant charge recombination of the photogenerated charges, while, when $\gamma \sim 1$, all photogenerated charges take part to the redox reaction. Hence, the measured value of $\gamma = 0.83$ in 1 M KCl indicates a satisfactory utilization of the photogenerated charges to carry out the redox reaction. As shown in **Figure 32a**, the R

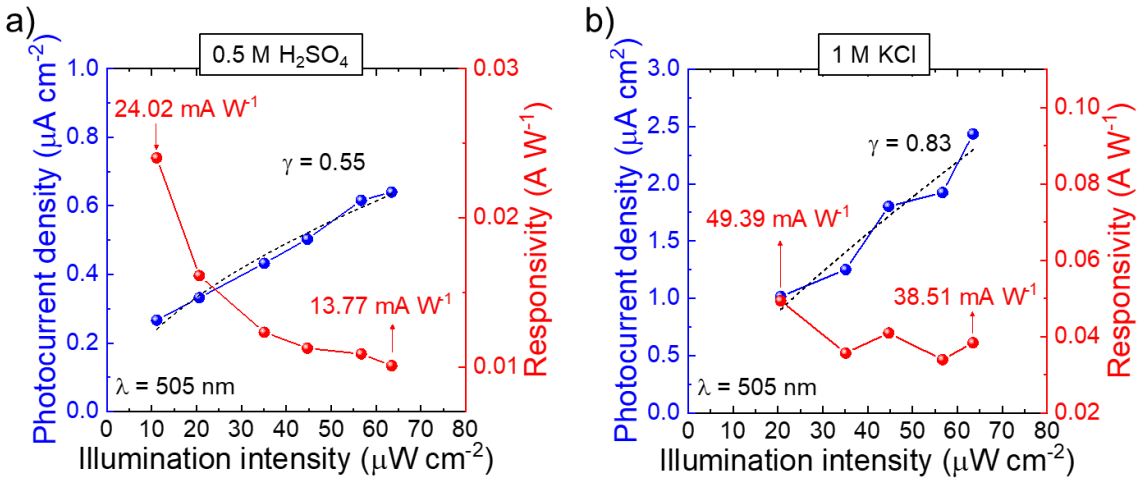

Figure 32: Photocurrent density (blue y-axis) and responsivity (red y-axis) of the GeSe photodetectors as a function of the light intensity a) at 0 V *versus* RHE in 0.5 M H_2SO_4 and b) at 0 V *versus*. RHE in 1 M KCl, respectively. Dashed black line indicates the curve fitting of the data [128].

decreases with increasing the light intensity, instead in **Figure 32b** is well-retained due to the intrinsic maximization of the electrochemically accessible surface area, as well as to the nearly zero distance between the photogenerated charges and the catalytic surface area.

Chapter 6

$PtTe_2$: an insight into structural and electronic properties

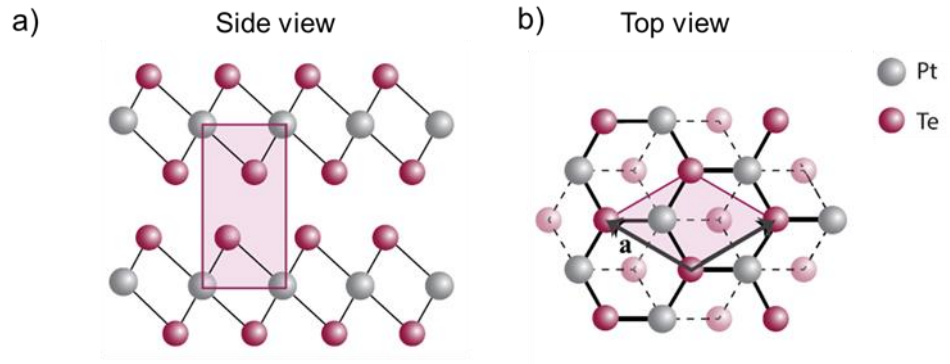

Figure 33: $PtTe_2$ crystal structures a) side and b) top view [198].

Recently, the PtX_2 (X=Se, Te, S) class of materials has attracted the interest of the scientific community. As a matter of fact, this class of transition-metal dichalcogenides (TMDs) combines the advantages and the application capabilities of van der Waals bulk semiconductors with the fundamental interest rising from the existence of type-II Dirac fermions.

While the band structure of PtX_2 has been led to nearly complete comprehension, collective electronic excitations have been studied only in the infrared range of the electromagnetic spectrum. On the other hand, the comprehension of the excitation spectrum of collective modes in the visible-ultraviolet is crucial in order to devise broadband photodetectors, ultraviolet-imaging applications and broadband plasmonic devices.

In this chapter, structural and electronic characterization of $PtTe_2$ crystal was probed by means of the combination of spectroscopic tools and theoretical calculations. The $PtTe_2$ crystal was synthetized by the self-flux method [198], [199]. **Figure 33a, b** report the schematic illustration of the side and top views crystal structure of $PtTe_2$, respectively. In particular, the surface structural corrugation and surface thermal expansion were evaluated by means of helium atom scattering (HAS).

In addition, the broad-band excitation spectrum of the $PtTe_2$ was explored, using electron energy-loss spectroscopy (EELS) complemented by detailed *ab initio* calculations.

EELS probes the broadband dielectric response of the system to a negatively charged probe, allowing for spectral contributions from both plasmonic modes and nonvertical transitions from valence-band to conduction-band electronic states. Therefore, EELS investigations supplement the studies of the absorption and emission processes of TMDs in the long-wavelength limit involving only vertical transitions from occupied to unoccupied states.

In contrast with metals, whose plasmon resonances are due to the excitation of free charge carriers, TMDs can provide plasmon resonance dominated by interband transitions taking the advantage of a higher absorptivity and less sensitivity to dimension. Interband plasmonic resonances are related to the generation of electron-hole pairs, appealing for various energy conversion processes, stimulating a host of novel developments in optoelectronic elements, ranging from photocatalysis up to thermoplasmonics.

Moreover, understanding the dependence of the lattice constant on temperature and the comprehension of the broadband excitation spectrum of crystals of $PtTe_2$ is important to implement this material in devices in nanoelectronics or optoelectronic applications such as photodetectors [200], [201], ultraviolet-imaging applications [202], and broadband plasmonic devices [203], [204]. More details about the used techniques are reported in Appendix A.

6.1Structural corrugation and surface thermal expansion of $PtTe_2$

The as-synthetized crystal was cleaved by scotch tape in air before introducing it into an ultra-high vacuum (UHV) system. The cleanliness and order of the surface were checked by low-energy electron diffraction (LEED). LEED analysis allowed to determine the symmetry of the two-dimensional surface lattice of the sample acquiring its reciprocal lattice (Figure 33b). Figure 33a

shows the diffraction pattern of the clean PtTe2 obtained with an incident electron energy of about 88 eV.

The structural corrugation and the lattice constant were calculated by HAS angular distributions

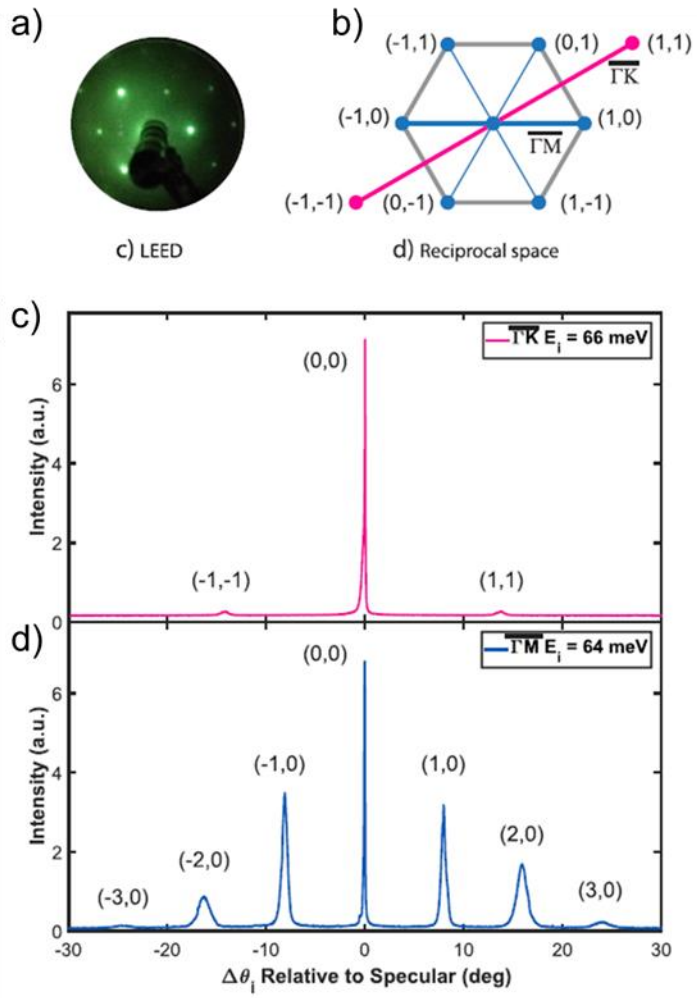

Figure 34: a) LEED pattern acquired at incident beam energy of 88 eV. b) Reciprocal lattice structure of $PtTe_2$. c) Angular distribution of He scattered by $PtTe_2$ along $\overline{\boldsymbol{\Gamma M}}$ and d) $\overline{\boldsymbol{\Gamma K}}$ directions [198].

measurements. **Figure 34c**, **d** report the HAS angular distributions measured from $PtTe_2$ (kept at 110 K) along $\overline{\Gamma M}$ and $\overline{\Gamma K}$ directions (the two main high-symmetry directions) with an incident energy of 64 meV and 66 meV, respectively. Clearly, the sample appears more corrugated along $\overline{\Gamma M}$, in fact the high intensity second ((-2,0) and (2,0)) and third ((-3,0) and (3,0)) order diffraction

peaks are observed. While along $\overline{\Gamma K}$ direction, the specular peak is dominant and the two peaks (-1,-1) and (1,1), which correspond at first-order diffraction, show a low intensity. The He angular distributions scattering from $PtTe_2$ were also performed in-plane (blue spectrum) and out-of-plane

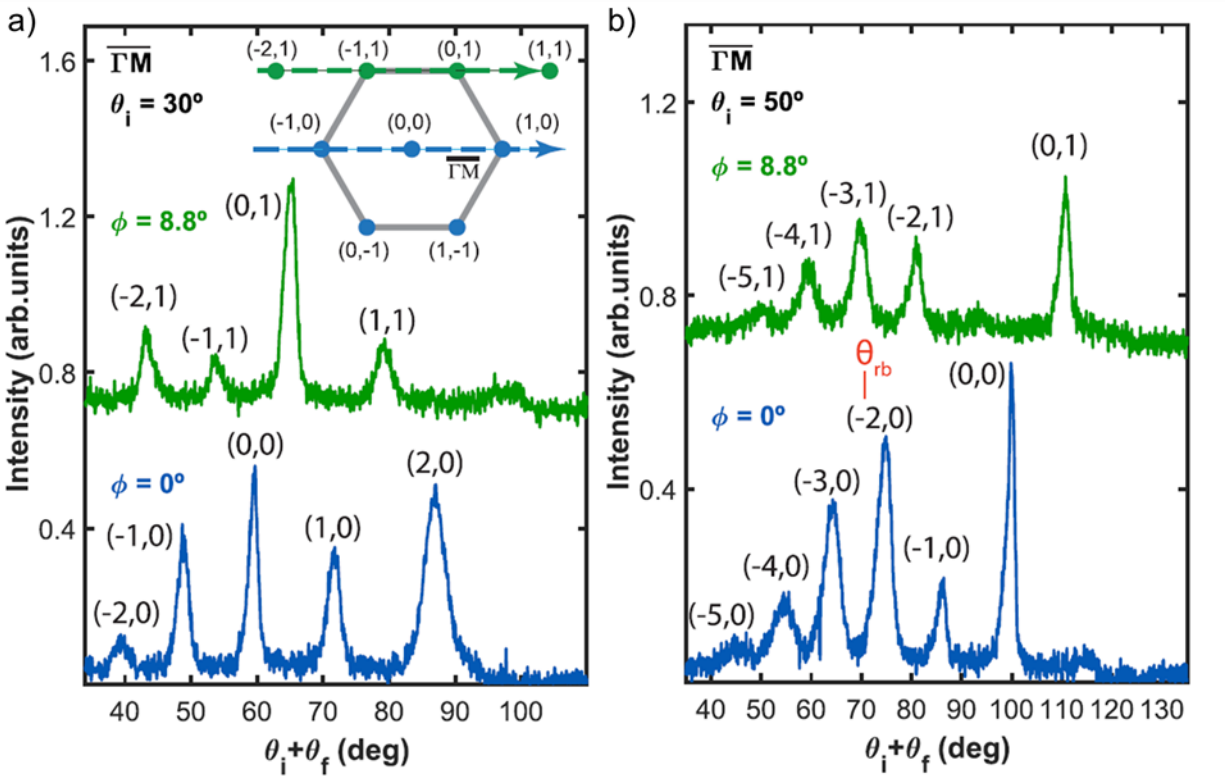

Figure 35: Angular distribution of He scattered by $PtTe_2$ along $\overline{\Gamma M}$ in-plane and out-of-plane, acquired at two different incident angle a) $\theta_i = 30°$ and b) $\theta_i = 50°$. The incident energy is of 49.5 meV and the surface temperature of 90 K [198].

(green spectrum) for two different angles of incident beam $\theta_i = 30°$ and $\theta_i = 50°$ along $\overline{\Gamma M}$ direction at an incident energy of 49.5 meV and at a surface temperature (T_s) of $PtTe_2$ of 90 K. The results are shown in **Figure 35a, b**. The measurements appear with low background, showing at θi = 30° the second-order diffraction peaks both in-plane and out-of-plane angular distributions, while at θi = 50° up to the fifth-order diffraction peaks are resolved in-plane angular distribution. The distribution of the peaks represents a rainbow effect [205], presenting a maximum at 28° (rainbow

angle $\Delta\theta_{rb}$) from the specular peak. The maximum surface corrugation amplitude can be estimated through the angular position of $\Delta\theta_{rb}$ [206], by the following relation

$$\zeta_m = \frac{a}{\pi} tan(\frac{\Delta\theta_{rb}}{2})$$

where a is the lattice constant along the scattering direction. The calculated value along the scattering direction ($\overline{\Gamma M}$) is ζ_m = 0.33 Å. The calculated ζ_m is similar to corrugation values of other layered materials [207], [208]. Among the in-plane diffraction peaks, the specular peak (0,0) exhibits high intensity with a specular reflectivity (normalized to the incident He beam) of ~ 0.5%. While the $PtTe_2$ surface total absolute reflectivity, defined as the ratio between measured diffraction peaks and the incident beam intensity, is ~ 4.5%. The lattice constant was determined by fitting the angular position of several helium angular distributions measurements.

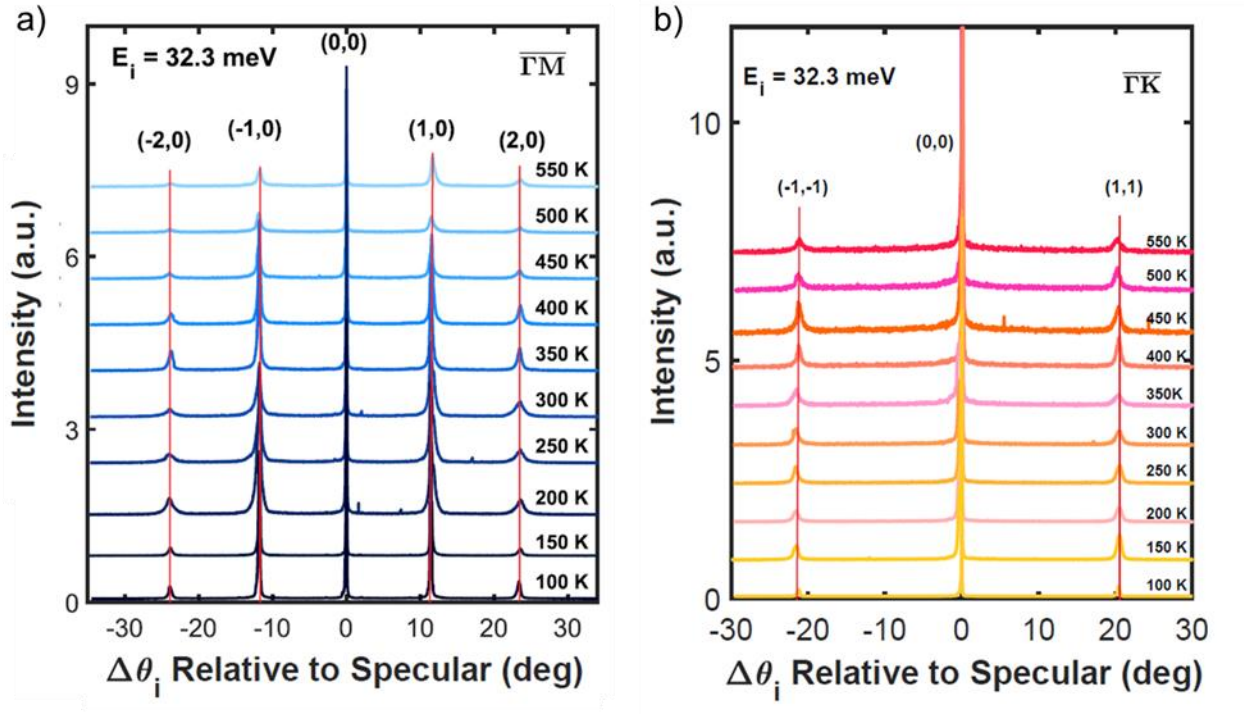

Figure 36: Angular distribution of He scattered by $PtTe_2$ along a) $\overline{\Gamma M}$ and b) $\overline{\Gamma K}$ directions, measured in a T_s range between 100 and 550 K. The incident energy is of 32.3 meV [198].

In fact, in order to obtain an accurate value of the lattice constant, more than 20 spectra were acquired under different conditions both in-plane and out-of-plane. From the spectra analysis, the estimated value of the lattice constant is a = (3.96 ± 0.05) Å. This value is similar to one reported in literature [209].

The lattice constant was evaluated with the increase of the surface temperature in a range from 100 to 550 K. All the spectra were acquired with an incident beam energy of 32.3 meV and along $\overline{\Gamma M}$ and $\overline{\Gamma K}$ directions (**Figure 36a, b** respectively). The angular distributions of He atoms scattered from $PtTe_2$ surface show the first- and second-order diffraction peaks for $\overline{\Gamma M}$ direction, in which the position of the diffracted peaks does not change when the surface temperature increase. A similar trend was verified along $\overline{\Gamma K}$ direction. The lattice constant value undergoes no variation in the temperature range between 100 and 550 K. This evidence that the surface thermal expansion of $PtTe_2$ is zero within the experimental error.

6.2 Electron-phonon coupling constant of $PtTe_2$

By increasing the Ts, additional inelastic scattering of the incoming He atoms are leaded by thermal vibrations of the surface atoms. This leads to thermal attenuation of the coherent diffraction intensities. This thermal attenuation can be described by Debye-Waller model [210]. The Debye-Waller factor relates the intensity $I(T_s)$ of a diffraction peak with the intensity I0 from a lattice at rest by the following relation

$$I(T_s) = I_0 e^{-2w(T_s)}$$

where $e^{-2w(T_s)}$ is the DW factor. In a specular geometry ($\theta_i = \theta_f$), the DW exponent can be written as

$$2W(T_s) = \frac{3\Delta k_{iz}^2 T_S}{M K_B \Theta_D^2}$$

where Δk_{iz}^2 is the squared normal component of the incident wave vector, M is the mass of the surface unit cell, k_B is the Boltzmann constant, Θ_D is the Debye temperature. **Figure 37** show the thermal attenuation of He specular intensity *vs.* the surface temperature of $PtTe_2$ at E_i = 49.5 meV along the two main directions, *i.e.*, $\overline{\Gamma M}$ (blue circles) and $\overline{\Gamma K}$ (magenta diamonds), respectively. Since, in the HAS approach, He atoms at thermal energies are diffracted by the surface charge

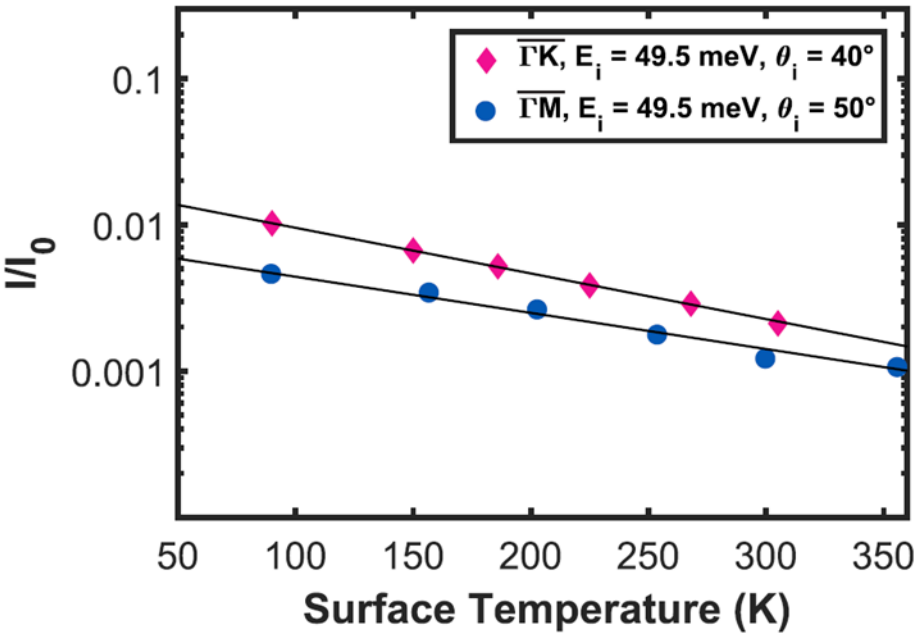

Figure 37: He specular intensity *vs.* the T_s of $PtTe_2$ at E_i = 49.5 meV along $\overline{\Gamma M}$ (blue circles) and $\overline{\Gamma K}$ (magenta diamonds) [198].

density corrugation, and in particular, the inelastic scattering coincides with the scattering by phonon-induced charge density oscillations [211]. In fact, the inelastic atom scattering intensity can be approximately proportional to the electron-phonon (e-p) coupling constant ($\lambda_{e\text{-}ph}$) for a specific phonon mode [210], [211]. Thus, the information on the $\lambda_{e\text{-}ph}$ can be provided by the DW exponent, which when $T > \Theta_D$ becomes approximately linear in T ($2W(T) = -\ln[I(T)/I_0]$) and is proportional to $\lambda_{e\text{-}ph}$ for a conducting surface [210], [212], [213]:

$$-\frac{\partial lnI(T)}{k_B \partial} = \frac{2W}{k_B T} = \frac{2n_{sat}}{\pi\phi} k_{iz}^2 a_c \lambda_{e-ph}$$

where ϕ is the work function (4.52 eV for $PtTe_2$ [214]), a_c the area of the surface unit cell (a_c = 14.03 Å^2), and $n_{sat} = \lambda_{TF}/c_0$ is the number of conducting layers of thickness c_0 within the inter-layer Thomas–Fermi (TF) screening length λ_{TF}. By the previous equations a simple form of $\lambda_{e\text{-}ph}$ can be written as:

$$\lambda_{e-ph} = \frac{6\pi\phi}{n_{sat} a_c M k_B^2 \Theta_D^2}$$

where $M\Theta_D^2$ is estimated from the slope of I/I_0 *vs.* surface temperature plot, providing a value of 4.5 x 10^6 amu K^2 and 4 x 10^6 amu K^2 for $\overline{\Gamma K}$ and $\overline{\Gamma K}$ data, respectively. The value of estimated n_{sat} for MX_2 class is n_{sat} = 2 [215]. The calculated value of e–ph coupling strength $\lambda_{e\text{-}ph}$ is ∼0.38 and ∼0.42 for data taken along $\overline{\Gamma K}$ and $\overline{\Gamma K}$, respectively. The obtained values are consistent with theoretical value ($\lambda_{e\text{-}ph}$ = 0.35) reported in literature [216].

6.3The broadband excitation spectrum of $PtTe_2$

Plasmonic modes in each class of van der Waals semiconductors have their own peculiarities, along with potential technological capabilities. Many innovative applications, widely used in our daily lives, are based on the exploitation of collective properties of matter (ferromagnetism, superconductivity, the quantum Hall effect, and plasmonic excitations). Therefore, the comprehension of collective electronic excitations is crucial in order to develop new disruptive technologies for health, telecommunications, energy, etc. In particular, the novel field of plasmonics has recently emerged, in consideration of the progress of nanotechnology and nanofabrication. Herein, the broadband excitation spectrum of bulk crystals of $PtTe_2$ was further characterized by electron energy loss spectroscopy (EELS) with particular respect to the nature and the propagation of plasmonic modes. Combining a hemispherical analyzer with a

monochromatic electron beam, parallel readout of momentum and energy is feasible, allowing the acquisition of complete dispersion relations. This technique also permits deeper analyses, including acquisition at different values of (i) primary electron beam energy and (ii) incidence angle to shed light on the interplay of the various modes in the excitation spectrum and, moreover, on the nature and the propagation of plasmonic modes (surface plasmons and interband plasmons).

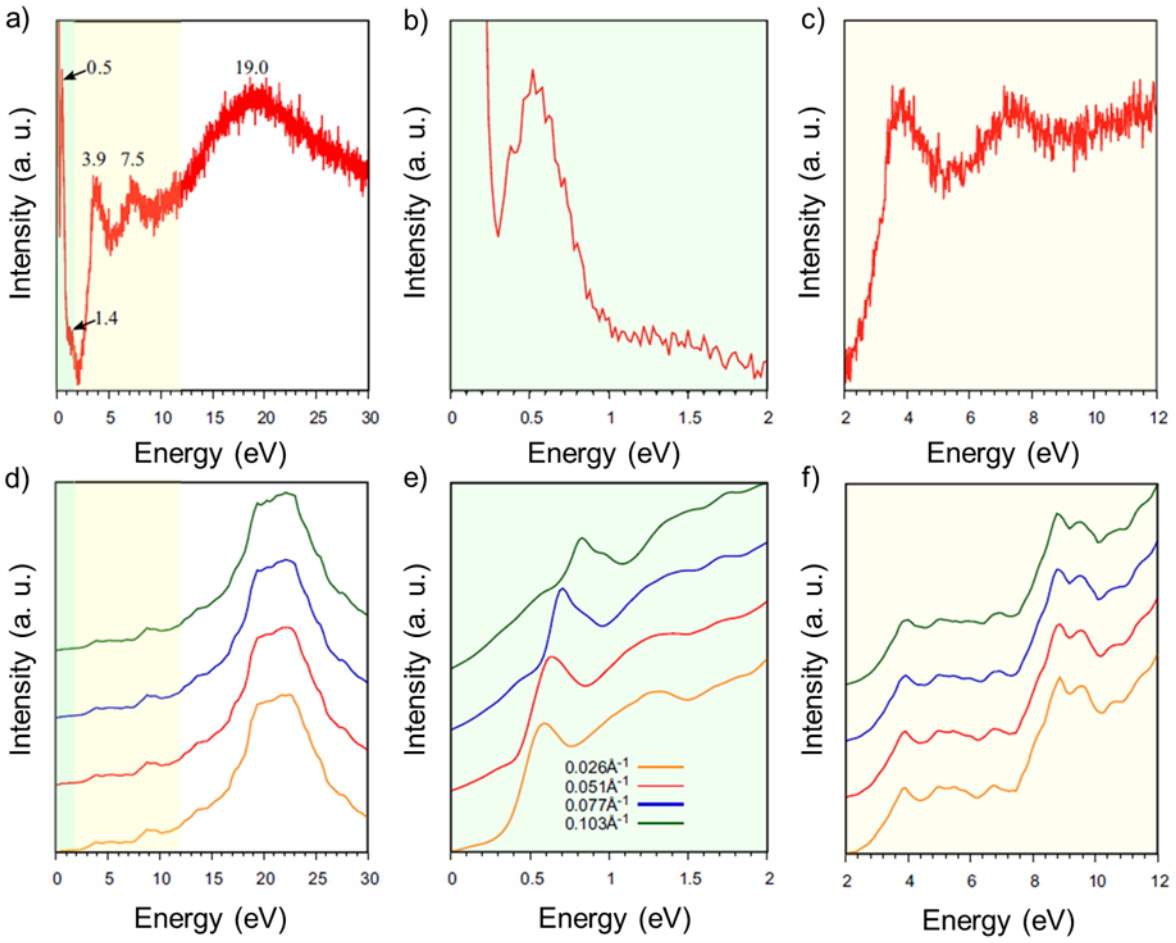

Figure 38: a) Broadband EELS spectrum for bulk PtTe2. a) Broadband EELS spectrum measured in reflection mode having a primary electron beam energy of 100 eV for a bulk crystal of PtTe2. b) - c) Several distinct peaks at the energies 0.5, 1.4, 3.9, 7.5 and 19.0 eV, shown in the EELS spectrum. d) –f) Experimental broadband EELS spectrum captured by the loss function obtained from ab initio calculations. e) Experimental broadband EELS spectrum for different moment values. f) Intra-band dominant peaks at 3.9 and 7.5 eV [199].

The experimental analysis has been corroborated by the available ab initio tools on electronic properties of the $PtTe_2$.

The reflection EELS experiments were performed in an ultra-high vacuum (UHV) chamber with a base pressure of about 10^{-10} mbar at room temperature by means of an EELS apparatus with two 50 mm hemispherical deflectors, for both monochromator and analyzers. The kinetic energy of the primary electron beam was 100 eV, positioned at an incident angle of 45° with respect to the surface normal. **Figure 38a** presents the excitation spectrum measured in an energy range from 0 to 30 eV. The broadband EELS spectrum shows distinct peaks at an energy of ∼0.5, ∼1.4, ∼3.9, ∼7.5, and ∼19.0 eV. According to a previous study reported in the literature [217], the lowest-energy peak at 0.5 eV is identified as an intraband three-dimensional (3D) Dirac plasmon excitation in bulk $PtTe_2$, which disperses with momentum (**Figure 38b**). The other excitations at an energy of ∼1.4, ∼3.9, ∼7.5, and ∼19.0 eV are interband transitions, which are relatively less dispersive compared to the intraband 3D Dirac plasmon peak. Experimental data show very good agreement with theoretical simulations of loss functions obtained from *ab-initio* calculations, as shown **Figure 38c-d**, in which the highest intensity peak in experiment, as well as the ab initio calculations, is at 19.0 eV. The comparison of the calculated orbital-resolved density of states (DOS), shown in **Figure 39a, b**, with electron energy loss spectra allow to assignment of the spectral features to transitions between specific electronic states. The peaks located at ∼3.9, ∼7.5 and ∼19.0 eV indicate the $Pt_{5d} \rightarrow Pt_{5d}$, $Te_{5p} \rightarrow Te_{5d}$, and $Te_{5s} \rightarrow Te_{5d}$ transitions, respectively.

It is also evaluated the broadband EELS spectrum of $PtTe_2$ thin films using the STEM-EELS

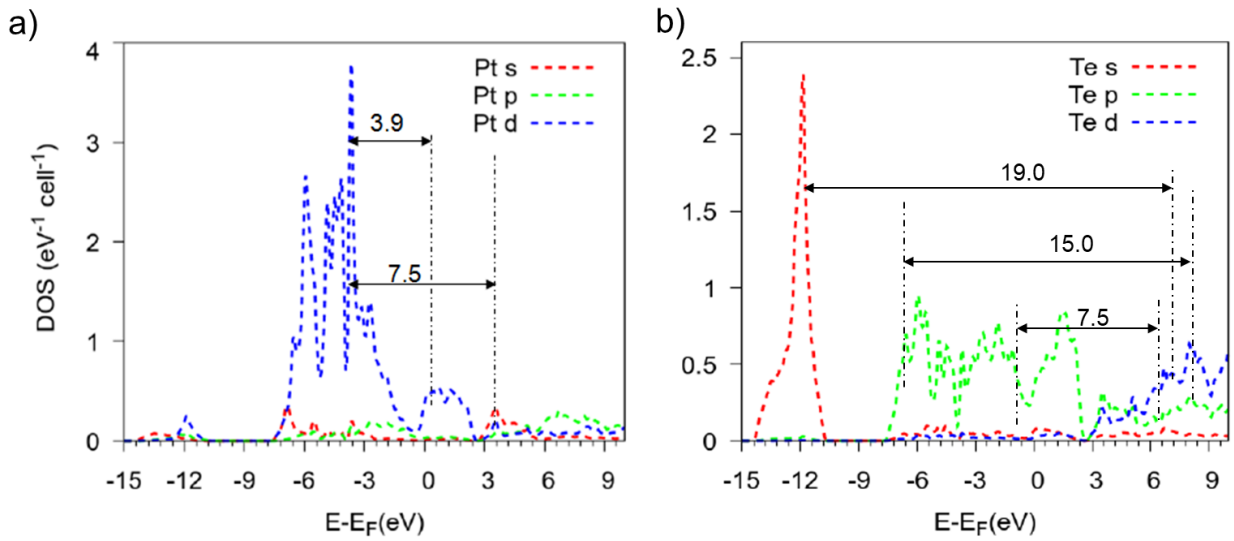

Figure 39: Orbital-resolved density of states corresponding to a) Pt orbitals and b) Te orbitals [199].

method. **Figure 40a** displays a STEM image of $PtTe_2$ flake, produced by LPE. This flake presents an inhomogeneous thickness. Thus, the STEM-EELS experiments were employed in different regions (indicated by the yellow letters in **Figure 40b**) with different thicknesses in order to evaluate the dependence of the $PtTe_2$ EELS spectrum from thickness. Points A, B, and C show a lower thickness with an asymmetrical shape peak at ~23 eV, while for the thicker region (point D) the shape of the peak is symmetrical with a corresponding centroid around ~20.5 eV. Point E, situated far from $PtTe_2$ flake, presents only the zero-loss peak. **Figure 40c** reports the broadband STEM-EELS spectra normalized to the zero-loss peak maximum. Io order to evaluate the difference in the shape of the peaks, **Figure 40d** displays the broadband STEM-EELS spectra normalized to the peak at ~20 eV.

Our STEM-EELS investigation suggests that in $PtTe_2$ the momentum-integrated (over the collection angle) high-energy EELS peak changes in both line shape and energy position as a function of thickness. Specifically, an asymmetrical line shape, centered at about 23 eV, is recorded for thinner regions (about 30 $PtTe_2$ unit cells along the c axis), whereas a symmetrical line shape, with a corresponding centroid around 20.5 eV, is revealed for thicker regions (about

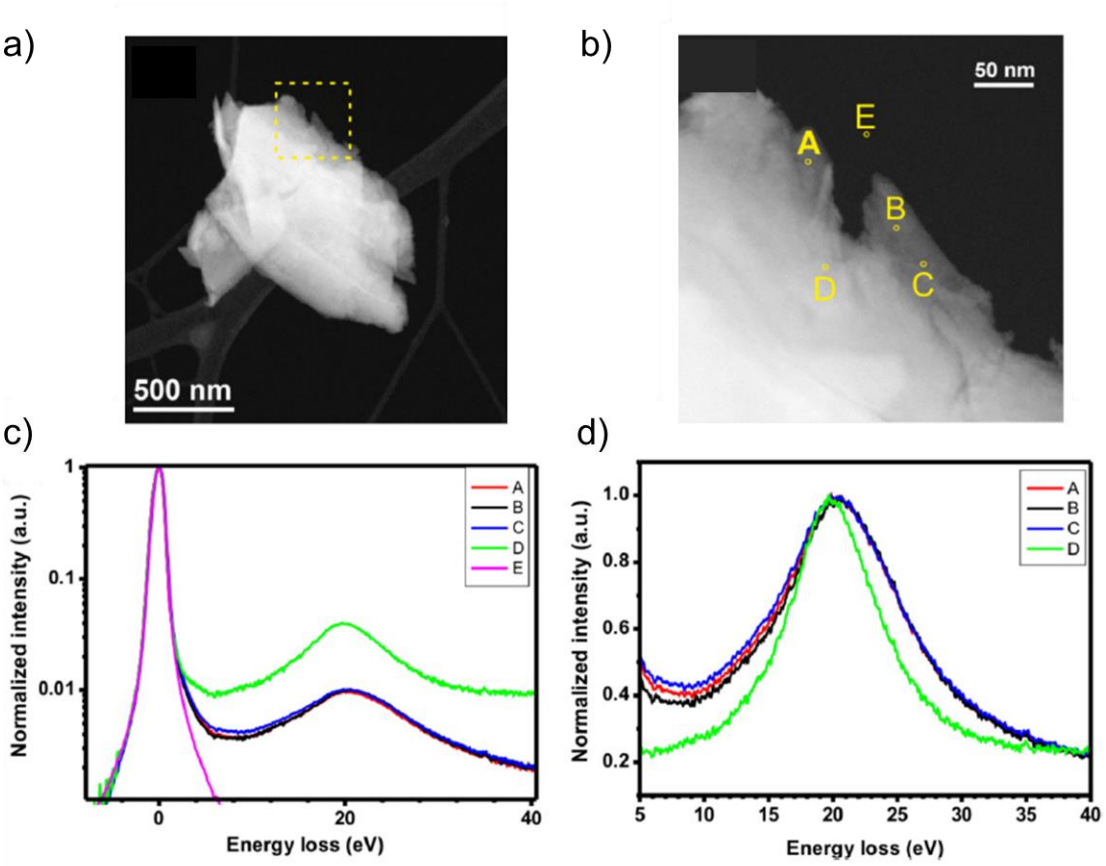

Figure 40: a) High-angle annular dark-field (HAADF)-STEM image of a $PtTe_2$ flake, partially suspended over a gap in the amorphous carbon backing film. b) Magnified detail of a); points A, B and C have a lower thickness (lower brightness in HAADF-STEM mode, corresponding to ~0.2λ) than point D (corresponding to ~0.8λ). c) Spectrum referred to point E; only the zero-loss peak appears, *i.e.*, 35 nm away from the $PtTe_2$ flake. Intensity is normalized to the zero-loss peak maximum. d) The broadband STEM-EELS spectra acquired for points A, B, C and D. The intensity is normalized to the peak at ~20 eV to highlight the differences in the shape of the lines of the peaks corresponding to different thicknesses [199].

120 $PtTe_2$ unit cells along the c axis). This is in contrast to other layered materials such as graphene and phosphorene. The high-energy EELS peak in $PtTe_2$ is redshifted with increasing thickness. The change in the line shape, with an asymmetrical shape characterizing the thinner regions, is ascribable to the multiple contributions (*i.e.*, due to regions with different thickness) to the spectra acquired in the thinner regions of the flakes. This peculiarity can be exploited for characterizing the thickness of $PtTe_2$ thin films. Similar physics is expected to play out in other members of the family as well, including $PdTe_2$ and $PtSe_2$.

Although there are several open challenges in plasmonics with 2D semiconductors, the plasmonic excitations in novel materials beyond graphene are still totally unexplored. In this chapter, the combination of spectroscopic tools and DFT offers an insight into structural and electronic properties of $PtTe_2$. The practical exploitation of high-energy excitations is generally challenging both from a fundamental as well as technological perspective for diverse applications, ranging from nanoelectronics, nanophotonics, and nanomedicine.

Conclusions

In conclusion, in this thesis, I evaluated the use of novel two-dimensional (2D) materials in solar energy applications, aiming to prove their potential as photocatalysts for water splitting devices.

To target a large-scale and low-cost material production approach, liquid-phase exfoliation (LPE) was exploited to produce 2D material-based dispersions compatible with large-area solution-processed deposition methods.

For example, I successfully obtained several dispersions based on LPE flakes of metal monochalcogenides (MMCs) (GaSe, GaS, and GeSe) for solar energy conversion devices.

Then, such dispersions were used for the implementation of photoelectrodes by spray coating onto graphite paper current collectors. The MMCs based photoelectrodes were investigated for PEC water splitting reactions, *i.e.*, hydrogen evolution reaction (HER) and oxygen evolution reaction (OER). In particular, GaSe photoelectrodes were tested in 0.5 M H_2SO_4 pH 0.3 and 1 M KOH pH 14, under the simulated sunlight, showing the best PEC performance in acidic conditions, with a cathodic photocurrent density at 0 V *vs.* RHE ($J_{0V\ vs.\ RHE}$) of –9.3 μA cm^{-2}, and a ratiometric power saved metric for HER 0.09%. In anodic conditions, the photoelectrode presented a photocurrent density at +1.23 V *vs.* RHE ($J_{1.23\ V\ vs.\ RHE}$) of 83.4 μA cm^{-2} and a ratiometric power saved metric for OER of 0.25%. On the other hand, GeSe based photoelectrodes were investigated in different media (0.5 M H_2SO_4 (pH 0.3), 1 M KCl (pH 6.5), 1 M KOH (pH 14)).

The GeSe photoelectrodes reached a $J_{0V\ vs.\ RHE}$ at 0 V *vs.* RHE of -10.9 μA cm^{-2} in 0.5 M H_2SO_4, while GeSe photoanodes displayed a $J_{1.23\ V\ vs.\ RHE}$ at +1.23 V *vs.* RHE of 31.0 μA cm^{-2} in 1 M KCl

In order to evaluate the catalytic activity, the MMCs-based photoelectrodes were also investigated to realize PEC-type photodetectors operating in different aqueous media, ranging from acidic to alkaline solutions (*i.e.*, 0.5 M H_2SO_4 (pH 0.3), 1 M Na_2SO_4 (pH = 6), 1 M KCl (pH 6.5), 1 M KOH (pH 14)) under different illumination wavelengths (namely 275, 455, 505, and 625 nm) corresponding to energy above their experimentally measured band gap.

The GaSe photodetectors showed a responsivity up to ~0.16 A W^{-1} upon 455 nm illumination at light intensity up to 63.5 µW cm^{-2} (at an applied potential of –0.3 V *vs.* RHE). The stability analysis of the GaSe photodetectors evidenced a durable operation in 0.5 M H_2SO_4 for PEC HER. *Viceversa*, degradations effects have been observed in both alkaline and anodic operation (*i.e.*, during OER) due to highly oxidizing environment and O_2 evolved-induced (photo-)oxidation effects.

While PEC-type 2D GaS photodetectors displayed a relevant UV-selective photoresponse. The measured responsivities (R) are 1.8 mA W^{-1} in 1 M H_2SO_4 (at 0.8 V *vs.* RHE), 4.6 mA W^{-1} in 1 M Na_2SO_4 (at 0.9 V *vs.* RHE), and 6.8 mA W^{-1} in 1 M KOH (at 1.1. V *vs.* RHE), respectively, under 275 nm illumination wavelength with an intensity of 1.3 mW cm^{-2}.

Finally, the best value of R was displayed by GeSe photodetectors. The GeSe photodetectors reached responsivity up to 316.6 mA W^{-1} at –0.5 V *vs.* RHE under 455 nm excitation wavelength in acidic electrolyte, which corresponds to an external quantum efficiency of 86.3%.

The R of our photodetectors are superior to those of several self-powered and low-voltage solution-processed photodetectors. Prospectively, the performances could be improved by optimizing the MMCs photoelectrodes, for example, by varying the thickness of MMCs films as well as by incorporating charge selective layers or co-catalysts. Overall, our research provides new insight

into the exploitation of the PEC properties of MMCs nanoflakes, paving the way towards their use in PEC applications, including photoelectrocatalysis, photodetectors, sensors, and other innovative optoelectronics devices.

Lastly, the study conducted on $PtTe_2$ provided structural and electronic information. The $PtTe_2$ surface shows a structural corrugation of ~ 0.33 Å, with a lattice constant of a = 3.96 ± 0.05 Å, which is independent of surface temperature between 100 and 550 K. The electron-phonon coupling constant, $\lambda_{e\text{-}ph}$, of $PtTe_2$ was evaluated by measuring the thermal attenuation of the elastic He-diffraction peak of this material. The calculated value is between 0.38 and 0.42. Finally, it was investigated the broadband excitation spectrum of bulk crystals and thin layers of $PtTe_2$.

Overall, the LPE of MMCs in their few-layer flakes by means of ultrasonication proved the production of novel type of photoelectrocatalysts for water splitting reactions, *i.e.*, hydrogen evolution reaction (HER) and oxygen evolution reaction (OER), as well as for photoelectrochemical (PEC)-type photodetectors. However, in view of their industrial use, the realization of these devices must be achieved by upscaling the exfoliation method. In this context, BeDimensional S.p.A. scale-up the production of high-quality 2D materials at industrial level by means of innovative wet-jet milling (WJM) setup. Prospectively, the technologies developed by BeDimensional may help my proof-of-concept devices to move from the laboratory to an industrially relevant environment. For this reason, my future research activity will focus on the industrial-scale production of 2D materials-based photoelectrodes, while further improving the performance of the latter. In particular, the production of advanced photoelectrodes could be achieved by optimizing the morphological features of the nanoflakes films in terms of thickness and electrochemically accessible surface area/porosity. In addition, the device efficiency can be enhanced by using addition of sacrificial reagents which help to control the electron-hole

recombination process. Moreover, the addition of one or more sacrificial agents (such as methanol, 2-propanol, and sodium sulfide/sodium sulfite), into the electrolytic solution of PEC devices, can potentially improve the stability of the current devices.

Appendix A

Characterization techniques of 2D material

A.1 Electron energy loss spectroscopy (EELS)

Electron energy-loss spectroscopy (EELS) is an analytical technique that is based on inelastic scattering of electrons in a sample [218]. In fact, when an electron interacts with the atomic electrons of the sample, it can undergo a loss of energy due to inelastic scattering, and this study offers information on the types of crystal excitation in a spatial region close to the surface. Energy losses, ranging from a few tenths of meV up to several hundred eV, depend on mainly three processes [219]:

1. Excitations of lattice vibrations of atoms relative to the clean surface (optical phonons and acoustic phonons) and/or vibrations of adsorbate molecular or atomic species.
2. Excitations of electronic transitions involving the valence band (inter- or intra-band single-particle excitations), surface, and volume plasmons.
3. Excitations of deep electronic states (core-level excitations).

In this technique, two different geometries can be used: transmission and reflection geometry. The first uses high energy electron beams (50-200 KeV) [219] and concerns the study of the volume properties of a solid, while the second configuration is used in the study of surface modes. Furthermore, reflection EELS spectroscopy turns out to be much more sensitive to the conditions of the solid surface than transmission spectroscopy, due to the low free path of electrons in the medium due to their high cross section. Similarly to optical spectroscopy, EEL spectroscopy offers information on the density of both filled and empty electronic states in a solid with the advantage

of being able to easily change the energy of the incident electron and access a wide range of energy without changes in the equipment [218]. The major disadvantage of this technique is its low resolution compared to that of optical spectroscopy, which can reach 1 meV in HREELS spectrometers. Transmission EELS spectroscopy has a resolution of about 0.5-0.05 eV, while for reflection EELS the best resolution obtainable is a few meV.

A.2 Helium atom scattering (HAS)

Helium Atom Scattering (HAS) is a very useful surface probe technique due to its high surface sensitivity and non-destructive effects [206]. Due to low energy (about 20-150 meV), the incident atom beam does not penetrate into the bulk and the atoms can approach the surface no more than 3-4 Å away from the surface layer, in contrast to the other incident beam, such as electron beam

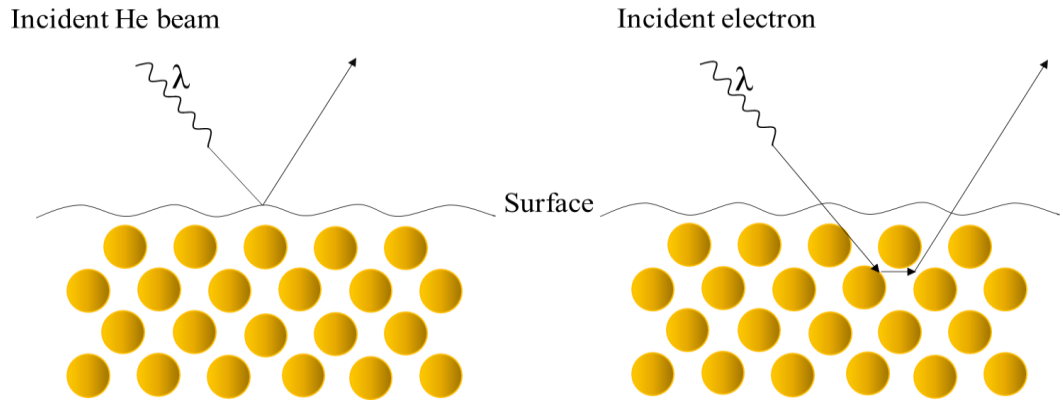

Figure 41: Schematic illustration of the different interaction mechanism of He atoms and electrons with the crystal.

(**Figure 41**). Thus, this technique is appropriated for studying the structural and dynamic properties of metallic, semiconducting, and insulating surfaces [206]. In particular, the chemical inertness of helium atoms makes the HAS technique very interesting for studying adsorption on insulating

surfaces because the incident He beam does not affect the surface structure and also does not give rise to surface charging effects.

Based on their scattering geometries, the equipment used for HAS experiments can be classified into two different groups:

1) “fixed angle” systems, in which the angle between the incident and outgoing beam is fixed;

2) systems that allow the detector to be rotated on two axes regardless of the incidence conditions.

The latter technique is the most favorable for structural studies because it has the advantage that all diffraction intensities can be recorded for a given scattering geometry, allowing for easier comparison with calculations.

On the other hand, the main disadvantage of this configuration is that it does not allows differential pumping of the detector, generally resulting in a smaller dynamic range of measured intensities compared to the differential pumping "fixed angle" systems used in TOF experiments.

A.3 Optical absorption spectroscopy

In order to evaluate the concentration of the LPE-produced dispersions, especially in view of industrial-scale applications, the absorption spectroscopy is a key characterization technique [97]. The phenomenon of refraction consists of the propagation of light in media having different refractive indices, leading to a bending of the light beam.

When a light-beam propagates through a liquid dispersion containing micrometric particles it is partially scattered or absorbed by the particles [220]. This phenomenon can be measured by optical absorption spectroscopy and the variation in intensity can be explained by Beer-Lambert

law [221]: a reduction in intensity is proportional to the initial intensity before the beam interacting with the sample. This can be described by the following equation:

$$dI = -\beta C(z)dz$$

where the change in intensity (*dI*) depends on C and l that are the sample concentration and the path length respectively while β is a proportionality constant.

The previous equation can be integrated for the length of the entire path length, finding the following relation:

$$C = \frac{A}{\varepsilon l}$$

where A is the Absorbance defined as $A = -log_{10}(\frac{I}{I_0})$ and ε, found experimentally, is the molar attenuation coefficient in the material sample.

A.4 Raman spectroscopy

Thanks to its versatility, Raman spectroscopy is one of the most important tools in the characterization of the different material allotropes [149], [222]–[224]. Unlike the optical absorption technique, in which most of the scattered light has the same frequency as the incident one (Rayleigh scattering), Raman spectroscopy is a technique based on inelastic scattering making use of a monochromatic laser source. The photons impinging on the sample are absorbed and re-emitted with the same or different frequency while the scattered photons have a reduced or increased frequency, a process known as Raman scattering [223]. Raman scattering is a very weak process (~ 10^{-5} % of the incident beam) and it is possible to distinguish two different Raman scattering processes, *i.e.*, Stokes and anti-Stokes scattering. In Stokes scattering, the frequency of scattered light is reduced with respect to the incident one, due to the photons' excitation, while in

anti-Stokes scattering the crystal is cooled down during the process because the frequency of the scattered light is increased [225] due to the dissipation of the thermal phonons in the crystal lattice. From the Raman scattering, it is possible to obtain characteristic features in terms of Raman shifts providing valuable information about vibrational, rotational, and low-frequency modifications in the samples.

Regarding the Raman spectrometer, the laser source is guided through an optical system, where it is shaped, focused, and transmitted thanks to mirrors hitting the sample. Subsequently, the scattered beam is focused again into an entrance slit and the surface of the sample can be observed with an optical microscope. Finally, the photon counting is performed by a Charge-Coupled Device that can detect the resulting beam, providing the Raman spectrum.

A.5 Atomic force microscopy (AFM)

Atomic-force microscopy (AFM) is a high-resolution scanning probe technique, capable to outperform optical microscopy by overcoming the problems of the diffraction limit, and with respect to the latter, it is demonstrated that AFM has a sub-nanometer resolution, being more than 1000 times higher [226].

In this technique, the morphological information (*i.e.*, highness and roughness of the sample) is collected by a mechanical probe, which "touches" the sample's surface.

In addition to morphology, the AFM can provide structural, mechanical, and electrical characterization of many materials, including graphene and related two-dimensional materials, with high sensitivity. Going beyond simple topography measurements, there are a myriad of mechanical and electrical characterization techniques that are based on the AFM's cantilever [227].

An AFM typically consists of a holder that supports an oscillating small spring-like cantilever [226]. A silicon sharp tip is fixed to the free end of the cantilever, while the detector records its deflection and motion. The sample is mounted on the sample stage drive that allows transferring the sample with a 3-axis manipulator.

Very accurate scanning is possible by accurate and precise movements of the piezoelectric elements. The typical AFM configuration enables the tip-sample interaction, transducing macro-scale motion of the cantilever, in fine movements. The cantilever motion can be used to quantify the interaction between the tip and sample. For example, within the most common different aspects, it is possible to evaluate the deflection (displacement with respect to the equilibrium position), the amplitude of an imposed oscillation of the cantilever, or the shift in the resonance frequency of the cantilever. The detector measures the deflection of the cantilever and converts it into an electrical signal. The intensity of this signal will be proportional to the displacement of the cantilever.

In this context, AFM presents static and dynamic modes, according to the nature of the tip motion. In static contact mode, the tip is "dragged" across the surface of the sample and the topology is measured using the deflection of the cantilever through the feedback signal. On the other hand, the dynamic modes are divided into tapping mode (also called intermittent contact, or, after the detection mechanism, amplitude modulation AFM) in which the cantilever is driven to oscillate up and down at its resonance frequency, and non-contact mode (or, after the detection mechanism, frequency modulation AFM), in which the tip of the cantilever does not contact the sample surface.

A.6 Electronic microscopy

In optical microscopy, the image resolution is physically limited because of the Abbe diffraction limit, which is ~250 nm, taking into account a visible range (from 380 to 740 nm) light source [228]. However, unlike the optical microscopes, in scanning electron microscopy (SEM) and transmission electron microscopy (TEM) the image resolution is not limited by lenses and mirrors, and a few nm resolution is obtained by a combination of the size of the electron spot, avoiding the problem due to the smaller de Broglie wavelength of electrons [229], and the interaction volume [230]. In fact, electrons, but in general all matter, exhibit a wave-like behavior [231] in which the de Broglie wavelength (λ) is associated to a massive particle and is related to its momentum, p, through the Planck constant, h [231]:

$$\lambda = \frac{h}{p}$$

Thus, SEM and TEM allow the study of (nano)materials up to the atomic scale by breaking the diffraction limit of the optical microscopy.

A.6.1 Transmission electron microscopy (TEM)

In a TEM experiment, the sample under analysis is placed on a perforated grid. TEMs are capable of performing high-resolution imaging of thin samples at the nanoscale [232]; hence, high-energy incident electron beam is required [232]. The related image is formed by the interaction of electrons transmitted through the sample; the image is magnified and focused on an imaging device, such as a fluorescent screen, a layer of photographic film, or to be detected by a sensor such as a charge-coupled device [232]. In the TEM technique, electrons are emitted from an electron gun (consisting of a tungsten filament or a source of lanthanum hexaboride) by thermionic or field emission under UHV conditions [232]. When the gun is connected to a high

voltage source (from 60 to 200 kV), it emits electrons and then the electron beam is created (analogue of a lamp that emits light rays in an optical microscope) [232]. Due to the electron's small mass, high vacuum conditions (typically up to 10^{-7} Pa) are required to avoid interactions or deflections with gas particles [232]. Subsequently, the electrons are injected into the microscope column thanks to the acceleration voltages, ~ 100 keV, and directed through a system of double or triple electromagnetic condensing lenses in order to illuminate the sample under examination [232]. The passage of electrons through the sample determines a scattering by the electrostatic potentials of the atoms [232].

A.6.2 Scanning electron microscopy (SEM)

Scanning electron microscopy is an imaging technique able to show both the morphology and information on the chemical composition of samples [230]. In particular, with this technique, it is possible to study the defects in 2D materials, examining any part of the sample [230].

In fact, in SEM imaging, the image is produced by the interaction of electrons with the surface of the samples. An electron beam (ø ~ 1 nm), condensed by a peculiar lens, is extracted by an anode, with an acceleration voltage in the range between 5 and 20 kV [233]. The beam, interacting with the surface, performs a line-by-line scan, varying the current through the scanning coils and producing the respective image [234]. Electrons are then emitted by the sample following the interaction with the electron beam [234].

Electrically conductive samples are needed for conventional imaging. Non-conductive samples can accumulate charge when scanned by the electron beam and this causes artefacts [234]. In fact, in the case of non-conductive samples, in order to withstand the high-vacuum conditions and the

high-energy beam of electrons, they can be prepared by low-vacuum sputter coating or by high-vacuum evaporation to increase their electrical conductivity and stabilize them [230].

SEM imaging involves two types of electrons: elastically scattered electrons and secondary low-energy (< 5 eV) inelastic electrons. Inelastically scattered electrons are suitable for surface imaging, providing information inside a few nm of sample. On the other hand, back-scattered electrons are higher in energy and give information about the sample's volume [234].

Heavier elements backscatter electrons more strongly, hence they can detect areas of different chemical composition [230]. Besides, when the electron beam hitting the surface removes core-shell electrons from the sample, characteristic x-rays are emitted. In this way, through the analysis of the emitted radiation, a chemical analysis of the sample is possible, by energy-dispersive X-ray spectroscopy (EDX) [234].

Usually, SEM instruments have chambers that can also tilt an object providing a continuous rotation of 360° [230]. Samples are mounted on a sample's holder with a conductive tape to be electrically grounded and prevent the accumulation of electrostatic charges [230].

References

[1] A. K. Geim and K. S. Novoselov, "The rise of graphene," *Nat. Mater.*, vol. 6, no. 3, pp. 183–191, Mar. 2007.

[2] M. J. Allen, V. C. Tung, and R. B. Kaner, "Honeycomb Carbon: A Review of Graphene," *Chem. Rev.*, vol. 110, no. 1, pp. 132–145, Jan. 2010.

[3] P. S. Karthik, A. L. Himaja, and S. P. Singh, "Carbon-allotropes: synthesis methods, applications and future perspectives," *Carbon Lett.*, vol. 15, no. 4, pp. 219–237, Oct. 2014.

[4] M. F. L. De Volder, S. H. Tawfick, R. H. Baughman, and A. J. Hart, "Carbon Nanotubes: Present and Future Commercial Applications," *Science (80-.).*, vol. 339, no. 6119, pp. 535–539, Feb. 2013.

[5] E. Pop, D. Mann, Q. Wang, K. Goodson, and H. Dai, "Thermal Conductance of an Individual Single-Wall Carbon Nanotube above Room Temperature," *Nano Lett.*, vol. 6, no. 1, pp. 96–100, Jan. 2006.

[6] B. K. Kaushik and M. K. Majumder, "Carbon nanotube: Properties and applications," in *Carbon Nanotube Based VLSI Interconnects*, Springer, 2015, pp. 17–37.

[7] J. M. Schnorr and T. M. Swager, "Emerging Applications of Carbon Nanotubes †," *Chem. Mater.*, vol. 23, no. 3, pp. 646–657, Feb. 2011.

[8] M. Endo, T. Hayashi, Y. A. Kim, and H. Muramatsu, "Development and Application of Carbon Nanotubes," *Jpn. J. Appl. Phys.*, vol. 45, no. 6A, pp. 4883–4892, Jun. 2006.

[9] P. L. de Andres, R. Ramírez, and J. A. Vergés, "Strong covalent bonding between two graphene layers," *Phys. Rev. B*, vol. 77, no. 4, p. 045403, Jan. 2008.

[10] A. H. Castro Neto, F. Guinea, N. M. R. Peres, K. S. Novoselov, and A. K. Geim, "The electronic properties of graphene," *Rev. Mod. Phys.*, vol. 81, no. 1, pp. 109–162, Jan. 2009.

[11] D. R. Cooper *et al.*, "Experimental Review of Graphene," *ISRN Condens. Matter Phys.*, vol. 2012, pp. 1–56, 2012.

[12] F. Bonaccorso, Z. Sun, T. Hasan, and A. C. Ferrari, "Graphene photonics and optoelectronics," *Nat. Photonics*, vol. 4, no. 9, pp. 611–622, Sep. 2010.

[13] A. S. Mayorov *et al.*, "Micrometer-Scale Ballistic Transport in Encapsulated Graphene at Room Temperature," *Nano Lett.*, vol. 11, no. 6, pp. 2396–2399, Jun. 2011.

[14] A. A. Balandin *et al.*, "Superior Thermal Conductivity of Single-Layer Graphene," *Nano Lett.*, vol. 8, no. 3, pp. 902–907, Mar. 2008.

[15] C. Lee, X. Wei, J. W. Kysar, and J. Hone, "Measurement of the Elastic Properties and Intrinsic Strength of Monolayer Graphene," *Science (80-.).*, vol. 321, no. 5887, pp. 385–388, Jul. 2008.

[16] J. K. Wassei and R. B. Kaner, "Graphene, a promising transparent conductor," *Mater. Today*, vol. 13, no. 3, pp. 52–59, Mar. 2010.

[17] R. R. Nair *et al.*, "Fine Structure Constant Defines Visual Transparency of Graphene," *Science (80-.).*, vol. 320, no. 5881, pp. 1308–1308, Jun. 2008.

[18] S. Eigler, "A new parameter based on graphene for characterizing transparent, conductive materials," *Carbon N. Y.*, vol. 47, no. 12, pp. 2936–2939, Oct. 2009.

[19] Q. H. Wang, K. Kalantar-Zadeh, A. Kis, J. N. Coleman, and M. S. Strano, "Electronics and optoelectronics of two-dimensional transition metal dichalcogenides," *Nat. Nanotechnol.*, vol. 7, no. 11, pp. 699–712, Nov. 2012.

[20] M. Chhowalla, H. S. Shin, G. Eda, L.-J. Li, K. P. Loh, and H. Zhang, “The chemistry of two-dimensional layered transition metal dichalcogenide nanosheets,” *Nat. Chem.*, vol. 5, no. 4, pp. 263–275, Apr. 2013.

[21] L. Najafi *et al.*, “Microwave-induced Structural Engineering and Pt Trapping in 6R-TaS2 for Hydrogen Evolution,” *Small*, 2020.

[22] A. Kuc and T. Heine, “The electronic structure calculations of two-dimensional transition-metal dichalcogenides in the presence of external electric and magnetic fields,” *Chem. Soc. Rev.*, vol. 44, no. 9, pp. 2603–2614, 2015.

[23] W. Choi, N. Choudhary, G. H. Han, J. Park, D. Akinwande, and Y. H. Lee, “Recent development of two-dimensional transition metal dichalcogenides and their applications,” *Mater. Today*, vol. 20, no. 3, pp. 116–130, Apr. 2017.

[24] A. Splendiani *et al.*, “Emerging photoluminescence in monolayer MoS2,” *Nano Lett.*, vol. 10, no. 4, pp. 1271–1275, Apr. 2010.

[25] M. Wang *et al.*, “Wafer-Scale Growth of 2D PtTe 2 with Layer Orientation Tunable High Electrical Conductivity and Superior Hydrophobicity,” *ACS Appl. Mater. Interfaces*, vol. 12, no. 9, pp. 10839–10851, Mar. 2020.

[26] A. Politano *et al.*, “Tailoring the Surface Chemical Reactivity of Transition-Metal Dichalcogenide PtTe 2 Crystals,” *Adv. Funct. Mater.*, vol. 28, no. 15, p. 1706504, Apr. 2018.

[27] M. Yan *et al.*, “Lorentz-violating type-II Dirac fermions in transition metal dichalcogenide PtTe2,” *Nat. Commun.*, vol. 8, no. 1, p. 257, Dec. 2017.

[28] H. Ma *et al.*, “Thickness-Tunable Synthesis of Ultrathin Type-II Dirac Semimetal PtTe 2 Single Crystals and Their Thickness-Dependent Electronic Properties,” *Nano Lett.*, vol. 18, no. 6, pp. 3523–3529, Jun. 2018.

[29] R. A. B. Villaos *et al.*, “Thickness dependent electronic properties of Pt dichalcogenides,” *npj 2D Mater. Appl.*, vol. 3, no. 1, p. 2, Dec. 2019.

[30] S.-D. Guo and Y. Wang, “Small compressive strain-induced semiconductor–metal transition and tensile strain-enhanced thermoelectric properties in monolayer PtTe 2,” *Semicond. Sci. Technol.*, vol. 32, no. 5, p. 055004, May 2017.

[31] B. Lei, Y.-Y. Zhang, and S.-X. Du, “Prediction of structured void-containing 1T-PtTe 2 monolayer with potential catalytic activity for hydrogen evolution reaction,” *Chinese Phys. B*, vol. 29, no. 5, p. 058104, May 2020.

[32] L. Fu *et al.*, “Highly Organized Epitaxy of Dirac Semimetallic PtTe 2 Crystals with Extrahigh Conductivity and Visible Surface Plasmons at Edges,” *ACS Nano*, vol. 12, no. 9, pp. 9405–9411, Sep. 2018.

[33] J. B. Mc Manus *et al.*, “Low-temperature synthesis and electrocatalytic application of large-area PtTe 2 thin films,” *Nanotechnology*, vol. 31, no. 37, p. 375601, Sep. 2020.

[34] P. K. Cheng, C. Y. Tang, X. Y. Wang, S. Ma, H. Long, and Y. H. Tsang, “Passively Q-switched Ytterbium-doped fiber laser based on broadband multilayer Platinum Ditelluride (PtTe2) saturable absorber,” *Sci. Rep.*, vol. 9, no. 1, p. 10106, Dec. 2019.

[35] X. Hu *et al.*, “Infrared Nanoimaging of Surface Plasmons in Type-II Dirac Semimetal PtTe 2 Nanoribbons,” *ACS Nano*, vol. 14, no. 5, pp. 6276–6284, May 2020.

[36] G. Antonius, D. Y. Qiu, and S. G. Louie, “Orbital Symmetry and the Optical Response of Single-Layer MX Monochalcogenides,” *Nano Lett.*, vol. 18, no. 3, pp. 1925–1929, Mar. 2018.

[37] H. Cai, Y. Gu, Y.-C. Lin, Y. Yu, D. B. Geohegan, and K. Xiao, “Synthesis and emerging properties of 2D layered III–VI metal chalcogenides,” *Appl. Phys. Rev.*, vol. 6, no. 4, p. 041312, Dec. 2019.

[38] A. S. Sarkar and E. Stratakis, “Recent Advances in 2D Metal Monochalcogenides,” *Adv. Sci.*, p. 2001655,

Sep. 2020.

[39] S. Barraza-Lopez and T. P. Kaloni, “Water Splits To Degrade Two-Dimensional Group-IV Monochalcogenides in Nanoseconds,” *ACS Cent. Sci.*, vol. 4, no. 10, pp. 1436–1446, Oct. 2018.

[40] C. Chowdhury, S. Karmakar, and A. Datta, “Monolayer Group IV-VI Monochalcogenides: Low-Dimensional Materials for Photocatalytic Water Splitting,” *J. Phys. Chem. C*, vol. 121, no. 14, pp. 7615–7624, Apr. 2017.

[41] Y. Guo, S. Zhou, Y. Bai, and J. Zhao, “Oxidation Resistance of Monolayer Group-IV Monochalcogenides,” *ACS Appl. Mater. Interfaces*, vol. 9, no. 13, pp. 12013–12020, Apr. 2017.

[42] H. R. Jappor and M. A. Habeeb, “Optical properties of two-dimensional GaS and GaSe monolayers,” *Phys. E Low-dimensional Syst. Nanostructures*, vol. 101, pp. 251–255, Jul. 2018.

[43] Y. Cui, L. Peng, L. Sun, Q. Qian, and Y. Huang, “Two-dimensional few-layer group-III metal monochalcogenides as effective photocatalysts for overall water splitting in the visible range,” *J. Mater. Chem. A*, vol. 6, no. 45, pp. 22768–22777, 2018.

[44] C.-H. Ho, M.-H. Hsieh, and C.-C. Wu, “Photoconductance and photoresponse of layer compound photodetectors in the UV-visible region,” *Rev. Sci. Instrum.*, vol. 77, no. 11, p. 113102, Nov. 2006.

[45] P. Hu, Z. Wen, L. Wang, P. Tan, and K. Xiao, “Synthesis of Few-Layer GaSe Nanosheets for High Performance Photodetectors,” *ACS Nano*, vol. 6, no. 7, pp. 5988–5994, Jul. 2012.

[46] H. Chen, Y. Li, L. Huang, and J. Li, “Intrinsic defects in gallium sulfide monolayer: a first-principles study,” *RSC Adv.*, vol. 5, no. 63, pp. 50883–50889, 2015.

[47] H. L. Zhuang and R. G. Hennig, “Single-Layer Group-III Monochalcogenide Photocatalysts for Water Splitting,” *Chem. Mater.*, vol. 25, no. 15, pp. 3232–3238, Aug. 2013.

[48] D. J. Late *et al.*, “GaS and GaSe Ultrathin Layer Transistors,” *Adv. Mater.*, vol. 24, no. 26, pp. 3549–3554, Jul. 2012.

[49] N. Curreli *et al.*, “Liquid-Phase Exfoliated Gallium Selenide for Light-Driven Thin-Film Transistors,” *Adv. Electron. Mater.*, p. 2001080, Jan. 2021.

[50] K. Kato and N. Umemura, “Sellmeier equations for GaS and GaSe and their applications to the nonlinear optics in GaS_xSe_1−x,” *Opt. Lett.*, vol. 36, no. 5, p. 746, Mar. 2011.

[51] Y. J. Ding and W. Shi, “Widely tunable monochromatic THz sources based on phase-matched difference-frequency generation in nonlinear-optical crystals: A novel approach,” *Laser Phys.*, vol. 16, no. 4, pp. 562–570, Apr. 2006.

[52] Y. Lu *et al.*, “Controlling Defects in Continuous 2D GaS Films for High-Performance Wavelength-Tunable UV-Discriminating Photodetectors,” *Adv. Mater.*, vol. 32, no. 7, p. 1906958, Feb. 2020.

[53] P. Hu *et al.*, “Highly Responsive Ultrathin GaS Nanosheet Photodetectors on Rigid and Flexible Substrates,” *Nano Lett.*, vol. 13, no. 4, pp. 1649–1654, Apr. 2013.

[54] C. Yang, P. Lu, W. Huang, and J. Chen, “Mechanical stabilities and nonlinear properties of monolayer Gallium sulfide under tension,” *Superlattices Microstruct.*, vol. 80, pp. 80–90, Apr. 2015.

[55] Y. Guo, S. Zhou, Y. Bai, and J. Zhao, “Defects and oxidation of group-III monochalcogenide monolayers,” *J. Chem. Phys.*, vol. 147, no. 10, p. 104709, Sep. 2017.

[56] Y. Ma, Y. Dai, M. Guo, L. Yu, and B. Huang, “Tunable electronic and dielectric behavior of GaS and GaSe monolayers,” *This J. is c Own. Soc.*, vol. 15, p. 7098, 2013.

[57] E. Petroni *et al.*, “Liquid-Phase Exfoliated Indium–Selenide Flakes and Their Application in Hydrogen Evolution Reaction,” *Small*, vol. 14, no. 26, p. 1800749, May 2018.

[58] A. Harvey *et al.*, “Preparation of Gallium Sulfide Nanosheets by Liquid Exfoliation and Their Application As Hydrogen Evolution Catalysts,” *Chem. Mater.*, vol. 27, no. 9, pp. 3483–3493, May 2015.

[59] A. Okazaki, “The Crystal Structure of Germanium Selenide GeSe,” *J. Phys. Soc. Japan*, vol. 13, no. 10, pp. 1151–1155, Oct. 1958.

[60] S. M. Yoon, H. J. Song, and H. C. Choi, “p-Type Semiconducting GeSe Combs by a Vaporization-Condensation-Recrystallization (VCR) Process,” *Adv. Mater.*, vol. 22, no. 19, pp. 2164–2167, Mar. 2010.

[61] Y. Ye *et al.*, “Two-Dimensional GeSe as an Isostructural and Isoelectronic Analogue of Phosphorene: Sonication-Assisted Synthesis, Chemical Stability, and Optical Properties,” *Chem. Mater.*, vol. 29, no. 19, pp. 8361–8368, Oct. 2017.

[62] B. Ul Haq, S. AlFaify, A. Laref, R. Ahmed, and M. F. M. Taib, “Dimensionality reduction of germanium selenide for high-efficiency thermoelectric applications,” *Ceram. Int.*, vol. 45, no. 12, pp. 15122–15127, Aug. 2019.

[63] S. Zhang *et al.*, “Structural and electronic properties of atomically thin germanium selenide polymorphs,” *Sci. China Mater.*, vol. 58, no. 12, pp. 929–935, Dec. 2015.

[64] Z. Hu, Y. Ding, X. Hu, W. Zhou, X. Yu, and S. Zhang, “Recent progress in 2D group IV-IV monochalcogenides: Synthesis, properties and applications,” *Nanotechnology*, vol. 30, no. 25. p. 252001, 21-Jun-2019.

[65] F. O. von Rohr, H. Ji, F. A. Cevallos, T. Gao, N. P. Ong, and R. J. Cava, “High-Pressure Synthesis and Characterization of β-GeSe—A Six-Membered-Ring Semiconductor in an Uncommon Boat Conformation,” *J. Am. Chem. Soc.*, vol. 139, no. 7, pp. 2771–2777, Feb. 2017.

[66] P. Zhao *et al.*, “Design of new photovoltaic systems based on two-dimensional group-IV monochalcogenides for high performance solar cells,” *J. Mater. Chem. A*, vol. 5, no. 46, pp. 24145–24152, 2017.

[67] D. J. Xue *et al.*, “GeSe thin-film solar cells fabricated by self-regulated rapid thermal sublimation,” *J. Am. Chem. Soc.*, vol. 139, no. 2, pp. 958–965, Jan. 2017.

[68] B. Mukherjee, Y. Cai, H. R. Tan, Y. P. Feng, E. S. Tok, and C. H. Sow, “NIR Schottky Photodetectors Based on Individual Single-Crystalline GeSe Nanosheet,” *ACS Appl. Mater. Interfaces*, vol. 5, no. 19, pp. 9594–9604, Oct. 2013.

[69] M. Brahma, A. Kabiraj, D. Saha, and S. Mahapatra, “Scalability assessment of Group-IV mono-chalcogenide based tunnel FET,” *Sci. Rep.*, vol. 8, no. 1, p. 5993, Dec. 2018.

[70] R. Fei, W. Kang, and L. Yang, “Ferroelectricity and Phase Transitions in Monolayer Group-IV Monochalcogenides,” *Phys. Rev. Lett.*, vol. 117, no. 9, p. 097601, 2016.

[71] Y. Zhou, M. Zhao, Z. W. Chen, X. M. Shi, and Q. Jiang, “Potential application of 2D monolayer β-GeSe as an anode material in Na/K ion batteries,” *Phys. Chem. Chem. Phys.*, vol. 20, no. 48, pp. 30290–30296, 2018.

[72] H. Zhao *et al.*, “Band Structure and Photoelectric Characterization of GeSe Monolayers,” *Adv. Funct. Mater.*, vol. 28, no. 6, p. 1704855, Feb. 2018.

[73] X. Lv, W. Wei, Q. Sun, F. Li, B. Huang, and Y. Dai, “Two-dimensional germanium monochalcogenides for photocatalytic water splitting with high carrier mobility,” *Appl. Catal. B Environ.*, vol. 217, pp. 275–284, Nov. 2017.

[74] M. Yang, S. Cao, Q. You, L. Bin Shi, and P. Qian, “Intrinsic carrier mobility of monolayer GeS and GeSe: First-principles calculation,” *Phys. E Low-Dimensional Syst. Nanostructures*, vol. 118, p. 113877, Apr. 2020.

[75] Y. Xu *et al.*, “First-principles study on the electronic, optical, and transport properties of monolayer α - and β -GeSe,” *Phys. Rev. B*, vol. 96, no. 24, p. 245421, Dec. 2017.

[76] Y. Ji, M. Yang, H. Dong, T. Hou, L. Wang, and Y. Li, “Two-dimensional germanium monochalcogenide photocatalyst for water splitting under ultraviolet, visible to near-infrared light,” *Nanoscale*, vol. 9, no. 25, pp. 8608–8615, 2017.

[77] F. Bonaccorso, A. Lombardo, T. Hasan, Z. Sun, L. Colombo, and A. C. Ferrari, “Production and processing of graphene and 2d crystals,” *Mater. Today*, vol. 15, no. 12, pp. 564–589, Dec. 2012.

[78] M. Yi and Z. Shen, “A review on mechanical exfoliation for the scalable production of graphene,” *J. Mater. Chem. A*, vol. 3, no. 22, pp. 11700–11715, 2015.

[79] C. Backes *et al.*, “Production and processing of graphene and related materials,” *2D Mater.*, vol. 7, no. 2, p. 22001, 2020.

[80] K. S. Novoselov, “Electric Field Effect in Atomically Thin Carbon Films,” *Science (80-.).*, vol. 306, no. 5696, pp. 666–669, Oct. 2004.

[81] Y. Chen *et al.*, “Mechanically exfoliated black phosphorus as a new saturable absorber for both Q-switching and Mode-locking laser operation,” *Opt. Express*, vol. 23, no. 10, p. 12823, May 2015.

[82] F. Liu *et al.*, “Disassembling 2D van der Waals crystals into macroscopic monolayers and reassembling into artificial lattices,” *Science (80-.).*, vol. 367, no. 6480, pp. 903–906, Feb. 2020.

[83] V. Nicolosi, M. Chhowalla, M. G. Kanatzidis, M. S. Strano, and J. N. Coleman, “Liquid Exfoliation of Layered Materials,” *Science (80-.).*, vol. 340, no. 6139, pp. 1226419–1226419, Jun. 2013.

[84] A. C. Ferrari *et al.*, “Science and technology roadmap for graphene, related two-dimensional crystals, and hybrid systems,” *Nanoscale*, vol. 7, no. 11, pp. 4598–4810, 2015.

[85] F. Torrisi *et al.*, “Inkjet-Printed Graphene Electronics,” *ACS Nano*, vol. 6, no. 4, pp. 2992–3006, Apr. 2012.

[86] A. E. Del Rio Castillo *et al.*, “High-yield production of 2D crystals by wet-jet milling,” *Mater. Horizons*, vol. 5, no. 5, pp. 890–904, 2018.

[87] S. Bellani *et al.*, “Scalable Production of Graphene Inks via Wet-Jet Milling Exfoliation for Screen-Printed Micro-Supercapacitors,” *Adv. Funct. Mater.*, vol. 29, no. 14, p. 1807659, Apr. 2019.

[88] Y. Hernandez *et al.*, “High-yield production of graphene by liquid-phase exfoliation of graphite,” *Nat. Nanotechnol.*, vol. 3, no. 9, pp. 563–568, Sep. 2008.

[89] X. Li, X. Wang, L. Zhang, S. Lee, and H. Dai, “Chemically Derived, Ultrasmooth Graphene Nanoribbon Semiconductors,” *Science (80-.).*, vol. 319, no. 5867, pp. 1229–1232, Feb. 2008.

[90] F. Bonaccorso and Z. Sun, “Solution processing of graphene, topological insulators and other 2d crystals for ultrafast photonics,” *Opt. Mater. Express*, vol. 4, no. 1, p. 63, Jan. 2014.

[91] A. Capasso, A. E. Del Rio Castillo, H. Sun, A. Ansaldo, V. Pellegrini, and F. Bonaccorso, “Ink-jet printing of graphene for flexible electronics: An environmentally-friendly approach,” *Solid State Commun.*, vol. 224, pp. 53–63, Dec. 2015.

[92] H. M. Solomon, B. A. Burgess, G. L. Kennedy, and R. E. Staples, “1-Methyl-2-pyrrolidone (NMP): reproductive and developmental toxicity study by inhalation in the rat,” *Drug Chem. Toxicol.*, vol. 18, no. 4, pp. 271–293, 1995.

[93] W. M. Haynes, “CRC Handbook Chemistry and Physics,” *CRC Press*, 2016.

[94] M. Yi, Z. Shen, X. Zhang, and S. Ma, “Achieving concentrated graphene dispersions in water/acetone mixtures by the strategy of tailoring Hansen solubility parameters,” *J. Phys. D. Appl. Phys.*, vol. 46, no. 2, p. 025301, Jan. 2013.

[95] J. N. Coleman *et al.*, “Two-Dimensional Nanosheets Produced by Liquid Exfoliation of Layered Materials,” *Science (80-.).*, vol. 331, no. 6017, pp. 568–571, Feb. 2011.

[96] M. E. Uddin, T. Kuila, G. C. Nayak, N. H. Kim, B.-C. Ku, and J. H. Lee, “Effects of various surfactants on the dispersion stability and electrical conductivity of surface modified graphene,” *J. Alloys Compd.*, vol. 562, pp. 134–142, Jun. 2013.

[97] F. Bonaccorso, A. Bartolotta, J. N. Coleman, and C. Backes, “2D-Crystal-Based Functional Inks,” *Adv. Mater.*, vol. 28, no. 29, pp. 6136–6166, Aug. 2016.

[98] J. Kang *et al.*, “Solvent Exfoliation of Electronic-Grade, Two-Dimensional Black Phosphorus,” *ACS Nano*, vol. 9, no. 4, pp. 3596–3604, Apr. 2015.

[99] U. Khan, A. O’Neill, M. Lotya, S. De, and J. N. Coleman, “High-Concentration Solvent Exfoliation of Graphene,” *Small*, vol. 6, no. 7, pp. 864–871, Apr. 2010.

[100] M. V. Bracamonte, G. I. Lacconi, S. E. Urreta, and L. E. F. Foa Torres, “On the Nature of Defects in Liquid-Phase Exfoliated Graphene,” *J. Phys. Chem. C*, vol. 118, no. 28, pp. 15455–15459, Jul. 2014.

[101] K. Kouroupis-Agalou *et al.*, “Fragmentation and exfoliation of 2-dimensional materials: a statistical approach †,” 2014.

[102] K. O. Pedersen, “The development of svedberg’s ultracentrifuge,” *Biophys. Chem.*, vol. 5, no. 1–2, pp. 3–18, Jul. 1976.

[103] H. Freundlich, “The Ultracentrifuge. By The Svedberg and Kai O. Pedersen.,” *J. Phys. Chem.*, vol. 44, no. 7, pp. 952–953, 1940.

[104] X. Li *et al.*, “Large-Area Synthesis of High-Quality and Uniform Graphene Films on Copper Foils,” *Science (80-.).*, vol. 324, no. 5932, pp. 1312–1314, Jun. 2009.

[105] S. Mikhailov, *Physics and Applications of Graphene: Experiments*. BoD--Books on Demand, 2011.

[106] J. K. Rath, H. Meiling, and R. E. I. Schropp, “Low-temperature deposition of polycrystalline silicon thin films by hot-wire CVD,” *Sol. Energy Mater. Sol. Cells*, vol. 48, no. 1–4, pp. 269–277, Nov. 1997.

[107] M. Werner and R. Locher, “Growth and application of undoped and doped diamond films,” *Reports Prog. Phys.*, vol. 61, no. 12, pp. 1665–1710, Dec. 1998.

[108] W. Kern and G. L. Schnable, “Low-pressure chemical vapor deposition for very large-scale integration processing—A review,” *IEEE Trans. Electron Devices*, vol. 26, no. 4, pp. 647–657, Apr. 1979.

[109] K. Khan *et al.*, “Recent developments in emerging two-dimensional materials and their applications,” *J. Mater. Chem. C*, vol. 8, no. 2, pp. 387–440, 2020.

[110] Z. Cai, B. Liu, X. Zou, and H.-M. Cheng, “Chemical Vapor Deposition Growth and Applications of Two-Dimensional Materials and Their Heterostructures,” *Chem. Rev.*, vol. 118, no. 13, pp. 6091–6133, Jul. 2018.

[111] T. T. Kodas and M. J. Hampden-Smith, *The chemistry of metal CVD*. John Wiley & Sons, 2008.

[112] B. Liu, M. Fathi, L. Chen, A. Abbas, Y. Ma, and C. Zhou, “Chemical Vapor Deposition Growth of Monolayer WSe 2 with Tunable Device Characteristics and Growth Mechanism Study,” *ACS Nano*, vol. 9, no. 6, pp. 6119–6127, Jun. 2015.

[113] A. Y. Cho and J. R. Arthur, “Molecular beam epitaxy,” *Prog. Solid State Chem.*, vol. 10, pp. 157–191, Jan. 1975.

[114] A. Al-Temimy, C. Riedl, and U. Starke, “Low temperature growth of epitaxial graphene on SiC induced by carbon evaporation,” *Appl. Phys. Lett.*, vol. 95, no. 23, p. 231907, Dec. 2009.

[115] S. K. Jerng *et al.*, “Nanocrystalline Graphite Growth on Sapphire by Carbon Molecular Beam Epitaxy,” *J. Phys. Chem. C*, vol. 115, no. 11, pp. 4491–4494, Mar. 2011.

[116] Z. Liu, J. Tang, C. Kang, C. Zou, W. Yan, and P. Xu, “Effect of substrate temperature on few-layer graphene grown on Al2O3 (0001) via direct carbon atoms deposition,” *Solid State Commun.*, vol. 152, no.

11, pp. 960–963, Jun. 2012.

[117] O. Seifarth, G. Lippert, J. Dabrowski, G. Lupina, W. Mehr, and M. C. Lemme, “Graphene directly grown on SiO2-based insulators,” in *2011 Semiconductor Conference Dresden*, 2011, pp. 1–4.

[118] G. Lippert, J. Dabrowski, M. Lemme, C. Marcus, O. Seifarth, and G. Lupina, “Direct graphene growth on insulator,” *Phys. status solidi*, vol. 248, no. 11, pp. 2619–2622, Nov. 2011.

[119] J. M. Garcia *et al.*, “Multilayer graphene films grown by molecular beam deposition,” *Solid State Commun.*, vol. 150, no. 17–18, pp. 809–811, May 2010.

[120] J. Hackley, D. Ali, J. DiPasquale, J. D. Demaree, and C. J. K. Richardson, “Graphitic carbon growth on Si(111) using solid source molecular beam epitaxy,” *Appl. Phys. Lett.*, vol. 95, no. 13, p. 133114, Sep. 2009.

[121] J. M. Garcia *et al.*, “Graphene growth on h-BN by molecular beam epitaxy,” *Solid State Commun.*, vol. 152, no. 12, pp. 975–978, Jun. 2012.

[122] S. K. Jerng *et al.*, “Graphitic Carbon Growth on MgO(100) by Molecular Beam Epitaxy,” *J. Phys. Chem. C*, vol. 116, no. 13, pp. 7380–7385, Apr. 2012.

[123] W. T. Tsang, “Chemical beam epitaxy of InP and GaAs,” *Appl. Phys. Lett.*, vol. 45, no. 11, pp. 1234–1236, Dec. 1984.

[124] K. Y. Lee *et al.*, “Molecular beam epitaxy grown template for subsequent atomic layer deposition of high κ dielectrics,” *Appl. Phys. Lett.*, vol. 89, no. 22, p. 222906, Nov. 2006.

[125] C. E. Chang and W. R. Wilcox, “Control of interface shape in the vertical bridgman-stockbarger technique,” *J. Cryst. Growth*, vol. 21, no. 1, pp. 135–140, Jan. 1974.

[126] N. Curreli *et al.*, “Liquid Phase Exfoliated Indium Selenide Based Highly Sensitive Photodetectors,” *Adv. Funct. Mater.*, vol. 30, no. 13, p. 1908427, Mar. 2020.

[127] M. I. Zappia *et al.*, “Solution-Processed GaSe Nanoflake-Based Films for Photoelectrochemical Water Splitting and Photoelectrochemical-Type Photodetectors,” *Adv. Funct. Mater.*, vol. 30, no. 10, p. 1909572, Mar. 2020.

[128] G. Bianca *et al.*, “Liquid-Phase Exfoliated GeSe Nanoflakes for Photoelectrochemical-Type Photodetectors and Photoelectrochemical Water Splitting,” *ACS Appl. Mater. Interfaces*, vol. 12, no. 43, pp. 48598–48613, Oct. 2020.

[129] M. I. Zappia *et al.*, “Two-Dimensional Gallium Sulfide Nanoflakes for UV-Selective Photoelectrochemical-type Photodetectors,” *J. Phys. Chem. C*, p. acs.jpcc.1c03597, May 2021.

[130] X. Li *et al.*, “Controlled Vapor Phase Growth of Single Crystalline, Two-Dimensional GaSe Crystals with High Photoresponse,” *Sci. Rep.*, vol. 4, no. 1, p. 5497, May 2015.

[131] D. V. Rybkovskiy *et al.*, “Size-induced effects in gallium selenide electronic structure: The influence of interlayer interactions,” *Phys. Rev. B*, vol. 84, no. 8, p. 085314, Aug. 2011.

[132] R. M. A. Lieth, Ed., *Preparation and Crystal Growth of Materials with Layered Structures*. Dordrecht: Springer Netherlands, 1977.

[133] Y. Tang, K. C. Mandal, J. A. McGuire, and C. W. Lai, “Layer- and frequency-dependent second harmonic generation in reflection from GaSe atomic crystals,” *Phys. Rev. B*, vol. 94, no. 12, 2016.

[134] W. Jie *et al.*, “Layer-Dependent Nonlinear Optical Properties and Stability of Non-Centrosymmetric Modification in Few-Layer GaSe Sheets,” *Angew. Chemie*, vol. 127, no. 4, pp. 1201–1205, Jan. 2015.

[135] A. Kuhn, A. Chevy, and R. Chevalier, “Refinement of the 2 H GaS β-type,” *Acta Crystallogr. Sect. B Struct. Crystallogr. Cryst. Chem.*, vol. 32, no. 3, pp. 983–984, Mar. 1976.

[136] A. Kuhn, A. Bourdon, J. Rigoult, and A. Rimsky, “Charge-density analysis of GaS,” *Phys. Rev. B*, vol. 25,

no. 6, pp. 4081–4088, Mar. 1982.

[137] M. Rahaman *et al.*, "Vibrational properties of GaSe: a layer dependent study from experiments to theory," *Semicond. Sci. Technol.*, vol. 33, no. 12, p. 125008, Dec. 2018.

[138] E. Finkman, J. Tauc, R. Kershaw, and A. Wold, "Lattice dynamics of tetrahedrally bonded semiconductors containing ordered vacant sites," *Phys. Rev. B*, vol. 11, no. 10, pp. 3785–3794, May 1975.

[139] D. Dohy, G. Lucazeau, and A. Revcolevschi, "Raman spectra and valence force field of single-crystalline β Ga2O3," *J. Solid State Chem.*, vol. 45, no. 2, pp. 180–192, Nov. 1982.

[140] P. J. Carroll and J. S. Lannin, "Raman Scattering of amorphous selenium films," *Solid State Commun.*, vol. 40, no. 1, pp. 81–84, 1981.

[141] A. A. Baganich, V. I. Mikla, D. G. Semak, A. P. Sokolov, and A. P. Shebanin, "Raman Scattering in Amorphous Selenium Molecular Structure and Photoinduced Crystallization," *Phys. status solidi*, vol. 166, no. 1, pp. 297–302, Jul. 1991.

[142] G. Lucovsky, A. Mooradian, W. Taylor, G. B. Wright, and R. C. Keezer, "Identification of the fundamental vibrational modes of trigonal, α - monoclinic and amorphous selenium," *Solid State Commun.*, vol. 5, no. 2, pp. 113–117, Feb. 1967.

[143] N. M. Gasanly, A. Aydınlı, H. Özkan, and C. Kocabaş, "Temperature dependence of the first-order Raman scattering in GaS layered crystals," *Solid State Commun.*, vol. 116, no. 3, pp. 147–151, Sep. 2000.

[144] J. C. Irwin, R. M. Hoff, B. P. Clayman, and R. A. Bromley, "Long wavelength lattice vibrations in GaS and GaSe," *Solid State Commun.*, vol. 13, no. 9, pp. 1531–1536, Nov. 1973.

[145] C. Jastrzebski, K. Olkowska, D. J. Jastrzebski, M. Wierzbicki, W. Gebicki, and S. Podsiadlo, "Raman scattering studies on very thin layers of gallium sulfide (GaS) as a function of sample thickness and temperature," *J. Phys. Condens. Matter*, vol. 31, no. 7, p. 075303, Feb. 2019.

[146] H. R. Chandrasekhar and U. Zwick, "Raman scattering and infrared reflectivity in GeSe," *Solid State Commun.*, vol. 18, no. 11–12, pp. 1509–1513, May 1976.

[147] T. Fukunaga, S. Sugai, T. Kinosada, and K. Murase, "Observation of new Raman lines in GeSe and SnSe at low temperatures," *Solid State Commun.*, vol. 38, no. 11, pp. 1049–1052, Jun. 1981.

[148] X. Zhang, Q.-H. H. Tan, J.-B. Bin Wu, W. Shi, and P.-H. H. Tan, "Review on the Raman spectroscopy of different types of layered materials," *Nanoscale*, vol. 8, no. 12, pp. 6435–6450, 2016.

[149] A. C. Ferrari and D. M. Basko, "Raman spectroscopy as a versatile tool for studying the properties of graphene," *Nat. Nanotechnol.*, vol. 8, no. 4, pp. 235–246, Apr. 2013.

[150] L. Najafi, S. Bellani, R. Oropesa-Nuñez, B. Martín-García, M. Prato, and F. Bonaccorso, "Single-/Few-Layer Graphene as Long-Lasting Electrocatalyst for Hydrogen Evolution Reaction," *ACS Appl. Energy Mater.*, vol. 2, no. 8, pp. 5373–5379, Aug. 2019.

[151] L. Quan *et al.*, "The Raman enhancement effect on a thin GaSe flake and its thickness dependence," *J. Mater. Chem. C*, vol. 3, no. 42, pp. 11129–11134, 2015.

[152] Y. Feng *et al.*, "Raman spectra of few-layer phosphorene studied from first-principles calculations," *J. Phys. Condens. Matter*, vol. 27, no. 18, p. 185302, May 2015.

[153] Z. Guo *et al.*, "From Black Phosphorus to Phosphorene: Basic Solvent Exfoliation, Evolution of Raman Scattering, and Applications to Ultrafast Photonics," *Adv. Funct. Mater.*, vol. 25, no. 45, pp. 6996–7002, Dec. 2015.

[154] L. Yang and S. J. Miklavcic, "Revised Kubelka–Munk theory III A general theory of light propagation in scattering and absorptive media," *J. Opt. Soc. Am. A*, vol. 22, no. 9, p. 1866, Sep. 2005.

[155] W. E. Vargas and G. A. Niklasson, "Applicability conditions of the Kubelka–Munk theory," *Appl. Opt.*, vol.

36, no. 22, p. 5580, Aug. 1997.

[156] H. Ahmad, S. K. Kamarudin, L. J. Minggu, and M. Kassim, “Hydrogen from photo-catalytic water splitting process: A review,” *Renew. Sustain. Energy Rev.*, vol. 43, pp. 599–610, Mar. 2015.

[157] S. Bellani, M. R. Antognazza, and F. Bonaccorso, “Carbon-Based Photocathode Materials for Solar Hydrogen Production,” *Advanced Materials*, vol. 31, no. 9. p. 1801446, Mar-2019.

[158] J. H. Kim, D. Hansora, P. Sharma, J.-W. Jang, and J. S. Lee, “Toward practical solar hydrogen production – an artificial photosynthetic leaf-to-farm challenge,” *Chem. Soc. Rev.*, vol. 48, no. 7, pp. 1908–1971, 2019.

[159] R. Sathre *et al.*, “Opportunities to improve the net energy performance of photoelectrochemical water-splitting technology,” *Energy Environ. Sci.*, vol. 9, no. 3, pp. 803–819, 2016.

[160] G. Ma, T. Hisatomi, and K. Domen, “Semiconductors for Photocatalytic and Photoelectrochemical Solar Water Splitting,” in *From Molecules to Materials*, Cham: Springer International Publishing, 2015, pp. 1–56.

[161] T. Hisatomi, J. Kubota, and K. Domen, “Recent advances in semiconductors for photocatalytic and photoelectrochemical water splitting,” *Chem. Soc. Rev.*, vol. 43, no. 22, pp. 7520–7535, Jan. 2014.

[162] L. Najafi *et al.*, “Hybrid Organic/Inorganic Photocathodes Based on WS2 Flakes as Hole Transporting Layer Material,” *Small Struct.*, vol. 2, no. 3, p. 2000098, Mar. 2021.

[163] D. Kang, T. W. Kim, S. R. Kubota, A. C. Cardiel, H. G. Cha, and K.-S. Choi, “Electrochemical Synthesis of Photoelectrodes and Catalysts for Use in Solar Water Splitting,” *Chem. Rev.*, vol. 115, no. 23, pp. 12839–12887, Dec. 2015.

[164] C. Jiang, S. J. A. Moniz, A. Wang, T. Zhang, and J. Tang, “Photoelectrochemical devices for solar water splitting – materials and challenges,” *Chem. Soc. Rev.*, vol. 46, no. 15, pp. 4645–4660, 2017.

[165] M. Gong and H. Dai, “A mini review of NiFe-based materials as highly active oxygen evolution reaction electrocatalysts,” *Nano Res.*, vol. 8, no. 1, pp. 23–39, Jan. 2015.

[166] J. K. Nørskov *et al.*, “Trends in the Exchange Current for Hydrogen Evolution,” *J. Electrochem. Soc.*, vol. 152, no. 3, p. J23, 2005.

[167] J. D. Benck, T. R. Hellstern, J. Kibsgaard, P. Chakthranont, and T. F. Jaramillo, “Catalyzing the Hydrogen Evolution Reaction (HER) with Molybdenum Sulfide Nanomaterials,” *ACS Catal.*, vol. 4, no. 11, pp. 3957–3971, Nov. 2014.

[168] M. Tahir *et al.*, “Electrocatalytic oxygen evolution reaction for energy conversion and storage: A comprehensive review,” *Nano Energy*, vol. 37, pp. 136–157, Jul. 2017.

[169] Y. Lee, J. Suntivich, K. J. May, E. E. Perry, and Y. Shao-Horn, “Synthesis and Activities of Rutile IrO 2 and RuO 2 Nanoparticles for Oxygen Evolution in Acid and Alkaline Solutions,” *J. Phys. Chem. Lett.*, vol. 3, no. 3, pp. 399–404, Feb. 2012.

[170] W. Zhou *et al.*, “Ni3S2 nanorods/Ni foam composite electrode with low overpotential for electrocatalytic oxygen evolution,” *Energy Environ. Sci.*, vol. 6, no. 10, p. 2921, 2013.

[171] C. C. L. McCrory, S. Jung, J. C. Peters, and T. F. Jaramillo, “Benchmarking Heterogeneous Electrocatalysts for the Oxygen Evolution Reaction,” *J. Am. Chem. Soc.*, vol. 135, no. 45, pp. 16977–16987, Nov. 2013.

[172] B. You, N. Jiang, M. Sheng, M. W. Bhushan, and Y. Sun, “Hierarchically Porous Urchin-Like Ni 2 P Superstructures Supported on Nickel Foam as Efficient Bifunctional Electrocatalysts for Overall Water Splitting,” *ACS Catal.*, vol. 6, no. 2, pp. 714–721, Feb. 2016.

[173] M. G. Walter *et al.*, “Solar Water Splitting Cells,” *Chem. Rev.*, vol. 110, no. 11, pp. 6446–6473, Nov. 2010.

[174] K. Sivula, “Metal Oxide Photoelectrodes for Solar Fuel Production, Surface Traps, and Catalysis,” *J. Phys. Chem. Lett.*, vol. 4, no. 10, pp. 1624–1633, May 2013.

[175] R. H. Coridan *et al.*, “Methods for comparing the performance of energy-conversion systems for use in solar fuels and solar electricity generation,” *Energy Environ. Sci.*, 2015.

[176] J. Joy, J. Mathew, and S. C. George, “Nanomaterials for photoelectrochemical water splitting – review,” *Int. J. Hydrogen Energy*, vol. 43, no. 10, pp. 4804–4817, Mar. 2018.

[177] H. C. Rojas *et al.*, “Polymer-based photocathodes with a solution-processable cuprous iodide anode layer and a polyethyleneimine protective coating,” *Energy Environ. Sci.*, vol. 9, no. 12, pp. 3710–3723, 2016.

[178] S. Bellani *et al.*, “Graphene-Based Hole-Selective Layers for High-Efficiency, Solution-Processed, Large-Area, Flexible, Hydrogen-Evolving Organic Photocathodes,” *J. Phys. Chem. C*, vol. 121, no. 40, pp. 21887–21903, Oct. 2017.

[179] S. Bellani, L. Najafi, A. Capasso, A. E. Del Rio Castillo, M. R. Antognazza, and F. Bonaccorso, “Few-layer MoS 2 flakes as a hole-selective layer for solution-processed hybrid organic hydrogen-evolving photocathodes,” *J. Mater. Chem. A*, vol. 5, no. 9, pp. 4384–4396, 2017.

[180] Z. Chen *et al.*, “Accelerating materials development for photoelectrochemical hydrogen production: Standards for methods, definitions, and reporting protocols,” *J. Mater. Res.*, vol. 25, no. 1, pp. 3–16, Jan. 2010.

[181] S. Chander, A. Purohit, A. Nehra, S. P. Nehra, and M. S. Dhaka, “A study on spectral response and external quantum efficiency of mono-crystalline silicon solar cell,” *Int. J. Renew. Energy Res.*, vol. 5, no. 1, pp. 41–44, 2015.

[182] D. Mandal, P. Routh, A. K. Mahato, and A. K. Nandi, “Electrochemically modified graphite paper as an advanced electrode substrate for supercapacitor application,” *J. Mater. Chem. A*, vol. 7, no. 29, pp. 17547–17560, 2019.

[183] F. Aziz and A. F. Ismail, “Spray coating methods for polymer solar cells fabrication: A review,” *Mater. Sci. Semicond. Process.*, vol. 39, pp. 416–425, Nov. 2015.

[184] S. M. Tan, C. K. Chua, D. Sedmidubský, Z. B. Sofer, and M. Pumera, “Electrochemistry of layered GaSe and GeS: Applications to ORR, OER and HER,” *Phys. Chem. Chem. Phys.*, vol. 18, no. 3, pp. 1699–1711, 2016.

[185] Y. Chung and C.-W. Lee, “Electrochemistry of Gallium,” *J. Electrochem. Sci. Technol.*, vol. 4, no. 1, pp. 1–18, 2013.

[186] H. Qiao *et al.*, “Self-Powered Photodetectors Based on 2D Materials,” *Adv. Opt. Mater.*, vol. 8, no. 1, p. 1900765, Jan. 2020.

[187] G. Konstantatos and E. H. Sargent, “Solution-Processed Quantum Dot Photodetectors,” *Proc. IEEE*, vol. 97, no. 10, pp. 1666–1683, Oct. 2009.

[188] J. Mathews, R. Roucka, J. Xie, S.-Q. Yu, J. Menéndez, and J. Kouvetakis, “Extended performance GeSn/Si(100) p-i-n photodetectors for full spectral range telecommunication applications,” *Appl. Phys. Lett.*, vol. 95, no. 13, p. 133506, Sep. 2009.

[189] S. Famà, L. Colace, G. Masini, G. Assanto, and H.-C. Luan, “High performance germanium-on-silicon detectors for optical communications,” *Appl. Phys. Lett.*, vol. 81, no. 4, pp. 586–588, Jul. 2002.

[190] S. Liu, X. Zhang, X. Gu, and D. Ming, “Photodetectors based on two dimensional materials for biomedical application,” *Biosens. Bioelectron.*, vol. 143, p. 111617, Oct. 2019.

[191] Y. Zou, Y. Zhang, Y. Hu, and H. Gu, “Ultraviolet Detectors Based on Wide Bandgap Semiconductor Nanowire: A Review,” *Sensors*, vol. 18, no. 7, p. 2072, Jun. 2018.

[192] J. Zhou, L. Chen, Y. Wang, Y. He, X. Pan, and E. Xie, “An overview on emerging photoelectrochemical self-powered ultraviolet photodetectors,” *Nanoscale*, vol. 8, no. 1, pp. 50–73, 2016.

[193] W. Tian, Y. Wang, L. Chen, and L. Li, “Self-Powered Nanoscale Photodetectors,” *Small*, vol. 13, no. 45, p. 1701848, Dec. 2017.

[194] Z. Li *et al.*, “High-Performance Photo-Electrochemical Photodetector Based on Liquid-Exfoliated Few-Layered InSe Nanosheets with Enhanced Stability,” *Adv. Funct. Mater.*, vol. 28, no. 16, p. 1705237, Apr. 2018.

[195] K. A. Mauritz and R. B. Moore, “State of understanding of Nafion,” *Chem. Rev.*, vol. 104, no. 10, pp. 4535–4585, Oct. 2004.

[196] C. (John) Zhang *et al.*, “Extra lithium-ion storage capacity enabled by liquid-phase exfoliated indium selenide nanosheets conductive network,” *Energy Environ. Sci.*, vol. 13, no. 7, pp. 2124–2133, 2020.

[197] L. Najafi *et al.*, “Octapod-Shaped CdSe Nanocrystals Hosting Pt with High Mass Activity for the Hydrogen Evolution Reaction,” *Chem. Mater.*, vol. 32, no. 6, pp. 2420–2429, Mar. 2020.

[198] G. Anemone *et al.*, “Experimental determination of surface thermal expansion and electron–phonon coupling constant of 1T-PtTe 2,” *2D Mater.*, vol. 7, no. 2, p. 025007, Jan. 2020.

[199] B. Ghosh *et al.*, “Broadband excitation spectrum of bulk crystals and thin layers of PtTe2,” *Phys. Rev. B*, vol. 99, no. 4, p. 045414, Jan. 2019.

[200] F. Koppens, T. Mueller, P. Avouris, … A. F.-N., and undefined 2014, “Photodetectors based on graphene, other two-dimensional materials and hybrid systems,” *nature.com*.

[201] X. Yu *et al.*, “Atomically thin noble metal dichalcogenide: a broadband mid-infrared semiconductor,” *nature.com*.

[202] X. Zhang, K. Wang, J. Ma, … Q. Z.-I. P., and undefined 2015, “Ultraviolet Imaging Based on Surface Plasmon Resonance With Azo-Polymer Sensing Layer,” *ieeexplore.ieee.org*.

[203] J. Ou, J. So, G. Adamo, A. Sulaev, … L. W.-N., and undefined 2014, “Ultraviolet and visible range plasmonics in the topological insulator Bi1.5Sb0.5Te1.8Se1.2,” *nature.com*.

[204] F. Bisio *et al.*, “Pushing the High-Energy Limit of Plasmonics,” *ACS Nano*, vol. 8, no. 9, pp. 9239–9247, Sep. 2014.

[205] U. Garibaldi, A. C. Levi, R. Spadacini, and G. E. Tommei, “Quantum theory of atom-surface scattering: Diffraction and rainbow,” *Surf. Sci.*, vol. 48, no. 2, pp. 649–675, Mar. 1975.

[206] D. Farias and K.-H. Rieder, “Atomic beam diffraction from solid surfaces,” *Reports Prog. Phys.*, vol. 61, no. 12, pp. 1575–1664, Dec. 1998.

[207] A. Ruckhofer, A. Tamtögl, M. Pusterhofer, M. Bremholm, and W. E. Ernst, “Helium–Surface Interaction and Electronic Corrugation of Bi 2 Se 3 (111),” *J. Phys. Chem. C*, vol. 123, no. 29, pp. 17829–17841, Jul. 2019.

[208] A. Tamtögl *et al.*, “A Helium-Surface Interaction Potential of Bi2Te3(111) from Ultrahigh-Resolution Spin-Echo Measurements,” *Surf. Sci.*, vol. 678, pp. 25–31, Dec. 2018.

[209] A. Kjekshus, F. Grønvold, P. M. Jørgensen, and S. Refn, “High Temperature X-Ray Study of the Thermal Expansion of PtS2, PtSe2, PtTe2 and PdTe2.,” *Acta Chem. Scand.*, vol. 13, pp. 1767–1774, 1959.

[210] J. R. Manson, G. Benedek, and S. Miret-Artés, “Electron–Phonon Coupling Strength at Metal Surfaces Directly Determined from the Helium Atom Scattering Debye–Waller Factor,” *J. Phys. Chem. Lett.*, vol. 7, no. 6, pp. 1016–1021, Mar. 2016.

[211] A. Tamtögl *et al.*, “Electron-phonon coupling and surface Debye temperature of Bi 2 Te 3 (111) from helium atom scattering,” *Phys. Rev. B*, vol. 95, no. 19, p. 195401, May 2017.

[212] J. R. Manson, G. Benedek, and S. Miret-Artés, “Correction to ‘Electron–Phonon Coupling Strength at Metal Surfaces Directly Determined from the Helium Atom Scattering Debye–Waller Factor,’” *J. Phys. Chem.*

Lett., vol. 7, no. 9, pp. 1691–1691, May 2016.

[213] G. Benedek, S. Miret-Artés, J. P. Toennies, and J. R. Manson, "Electron–Phonon Coupling Constant of Metallic Overlayers from Specular He Atom Scattering," *J. Phys. Chem. Lett.*, vol. 9, no. 1, pp. 76–83, Jan. 2018.

[214] F. A. Rasmussen and K. S. Thygesen, "Computational 2D Materials Database: Electronic Structure of Transition-Metal Dichalcogenides and Oxides," *J. Phys. Chem. C*, vol. 119, no. 23, pp. 13169–13183, Jun. 2015.

[215] G. Anemone, A. Al Taleb, G. Benedek, A. Castellanos-Gomez, and D. Farías, "Electron–Phonon Coupling Constant of 2H-MoS 2 (0001) from Helium-Atom Scattering," *J. Phys. Chem. C*, vol. 123, no. 6, pp. 3682–3686, Feb. 2019.

[216] K. Kim, S. Kim, J. S. Kim, H. Kim, J.-H. Park, and B. I. Min, "Importance of the van Hove singularity in superconducting PdTe2," *Phys. Rev. B*, vol. 97, no. 16, p. 165102, Apr. 2018.

[217] A. Politano *et al.*, "3D Dirac Plasmons in the Type-II Dirac Semimetal PtTe 2," *Phys. Rev. Lett.*, vol. 121, no. 8, p. 086804, Aug. 2018.

[218] F. Hofer, F. P. Schmidt, W. Grogger, and G. Kothleitner, "Fundamentals of electron energy-loss spectroscopy," *IOP Conf. Ser. Mater. Sci. Eng.*, vol. 109, p. 012007, Feb. 2016.

[219] M. De Crescenzi and M. N. Piancastelli, *Electron scattering and related spectroscopies*. World Scientific, 1996.

[220] A. T. Young, "Rayleigh scattering," *Appl. Opt.*, vol. 20, no. 4, pp. 533–535, 1981.

[221] D. F. Swinehart, "The beer-lambert law," *J. Chem. Educ.*, vol. 39, no. 7, p. 333, 1962.

[222] C. Casiraghi, S. Pisana, K. S. Novoselov, A. K. Geim, and A. C. Ferrari, "Raman fingerprint of charged impurities in graphene," *Appl. Phys. Lett.*, vol. 91, no. 23, p. 233108, Dec. 2007.

[223] A. C. Ferrari, "Raman spectroscopy of graphene and graphite: Disorder, electron–phonon coupling, doping and nonadiabatic effects," *Solid State Commun.*, vol. 143, no. 1–2, pp. 47–57, Jul. 2007.

[224] F. Liang, H. Xu, X. Wu, C. Wang, C. Luo, and J. Zhang, "Raman spectroscopy characterization of two-dimensional materials," *Chinese Phys. B*, vol. 27, no. 3, p. 037802, Mar. 2018.

[225] W. R. Browne and J. J. McGarvey, "The Raman effect and its application to electronic spectroscopies in metal-centered species: Techniques and investigations in ground and excited states," *Coord. Chem. Rev.*, vol. 251, no. 3–4, pp. 454–473, Feb. 2007.

[226] G. Binnig, C. F. Quate, and C. Gerber, "Atomic Force Microscope," *Phys. Rev. Lett.*, vol. 56, no. 9, pp. 930–933, Mar. 1986.

[227] S. Bertolazzi *et al.*, "Exploring flatland: AFM of mechanical and electrical properties of graphene, MoS2 and other low-dimensional materials," *Microsc. Anal.*, vol. 27, no. 3, 2013.

[228] S. G. (Stephen G. . L. and H. (Henry)Lipson A. (Ariel) Lipson, "Optical physics," *Cambridge Univ. Press*, 2011.

[229] E. Ruska, "The early development of electron lenses and electron microscopy.," *Microsc. Acta. Suppl.*, no. Suppl 5, pp. 1–140, 1980.

[230] D. McMullan, "Scanning electron microscopy 1928-1965," *Scanning*, vol. 17, no. 3, pp. 175–185, Dec. 2006.

[231] L. V. P. R. de Broglie, "Recherches sur la théorie des quanta," *Ann. Phys.*, vol. 2, pp. 22–128, 1925.

[232] M. Nic, L. Hovorka, J. Jirat, B. Kosata, and J. Znamenacek, *IUPAC compendium of chemical terminology-the gold book*. International Union of Pure and Applied Chemistry, 2005.

[233] E. Pretorius, “Influence of acceleration voltage on scanning electron microscopy of human blood platelets,” *Microsc. Res. Tech.*, p. NA-NA, 2009.

[234] J. I. Goldstein, D. E. Newbury, J. R. Michael, N. W. M. Ritchie, J. H. J. Scott, and D. C. Joy, *Scanning Electron Microscopy and X-Ray Microanalysis*. New York, NY: Springer New York, 2018.

UNIONE EUROPEA
Fondo Sociale Europeo

Ministero dell'Istruzione, dell'Università e della Ricerca

PON RICERCA E INNOVAZIONE 2014 - 2020

UNIVERSITÀ DELLA CALABRIA

La borsa di dottorato è stata cofinanziata con risorse del Programma Operativo Nazionale Ricerca e Innovazione 2014-2020 (CCI 2014IT16M2OP005), Fondo Sociale Europeo, Azione I.1 "Dottorati Innovativi con caratterizzazione Industriale"